Quantitative 3D Micro X-ray fluorescence spectroscopy

vorgelegt von
Diplom-Physikerin
Ioanna Mantouvalou
Chios, Griechenland

Von der Fakultät II - Mathematik und Naturwissenschaften
der Technischen Universität Berlin
zur Erlangung des akademischen Grades
Doktor der Naturwissenschaften
Dr.rer.nat.

genehmigte Dissertation

Promotionsausschuss:

Vorsitzender: Prof. Dr. rer. nat. Brandes
Berichter/Gutachter: Prof. Dr. rer. nat. Kanngießer
Berichter/Gutachter: Prof. Dr. rer. nat. Eberhardt

Tag der wissenschaftlichen Aussprache: 20.07.2009

Berlin 2009

D 83

Kurzdarstellung

Röntgenfluoreszenzspektroskopie (RFA) ist eine etablierte Methode zur zerstörungsfreien Elementanalyse unbekannter Proben. Durch die Entwicklung von speziellen Röntgenoptiken wurden laterale Untersuchungen im Mikrometerbereich möglich. Die Benutzung zweier Optiken in einer konfokalen Anordnung führt dazu, dass zusätzlich Informationen aus dem Probeninneren erhalten werden können. Bei der 3D Mikro-Röntgenfluoreszenzspektroskopie (3D Mikro-RFA) wird eine Polykapillarlinse benutzt, um die Anregungsstrahlung zu fokussieren, und eine weitere Linse schränkt das Sichtfeld eines energiedispersiven Detektors ein. Informationen über die Probe werden in erster Näherung ausschließlich aus dem Untersuchungsvolumen erlangt, welches durch die Überlagerung der beiden Foki der Linsen entsteht. Im Rahmen der vorliegenden Dissertation wird 3D Mikro-RFA als neue experimentelle und analytische Methode vorgestellt. Der Schwerpunkt der Arbeit liegt dabei auf der Quantifizierung der gewonnenen Messdaten.

Die vollständige Quantifizierung von 3D Mikro-RFA Messungen an Schichtsystemen mit monochromatischer Anregung wurde entwickelt und mit Hilfe eigens hergestellter Referenzschichtprobensysteme validiert. Sowohl die Fluoreszenz der Probe als auch die gestreute Anregungsstrahlung gibt dabei Aufschluss über die Schichtzusammensetzung und -dicke. Eine Quantifizierungssoftware wurde erstellt, die flexibel auf verschiedene Probentypen angewandt werden kann.

Im Vergleich zu konventioneller Mikro-RFA ist die messbare Fluoreszenz- und Streuintensität geringer, da nur aus einem Mikrovolumen Informationen gewonnen werden. Die Auswertung der Messdaten ist aufwändiger und birgt größere Unsicherheiten in sich. Für jede Probe müssen spezielle Fitstrategien entwickelt werden, um die zu Verfügung stehenden Informationen optimal zu nutzen. Dennoch ist 3D Mikro-RFA eine der wenigen Methoden, wenn das Innere einer Probe von Interesse ist und Mikroprobenentnahme oder Querschnitte nicht zulässig sind. Durch die präsentierte Möglichkeit der Rekonstruktion von Schichtzusammensetzung und -dicke wird die zerstörungsfreie 3D Mikro-RFA in eine analytische Meßmethode überführt.

Die Quantifizierung von 3D Mikro-RFA mit Röntgenröhrenanregung ist vergleichsweise komplexer, da die erste Linse ein Anregungsspektrum transportiert anstelle einer monochromatischen Anregungslinie. Erste Modellierungsansätze zum Untersuchungsvolumen sowie Überlegungen zur Kalibrierung und Quantifizierung werden vorgestellt.

Als eines der ersten Anwendungsgebiete für 3D Mikro-RFA bietet sich die Archäometrie an, da wertvolle Kulturgüter zerstörungsfrei und ohne Präparation untersucht werden können. Möglichkeiten und Beschränkungen der Quantifizierung werden anhand von drei Beispielen aus diesem Forschungsbereich dargestellt. Kombinationsmöglichkeiten mit anderen Röntgenmethoden wie Mikro-RFA, sowie die Nutzung von rein qualitativen Messungen mit 3D Mikro-RFA Spektrometern mit Röhrenanregung werden diskutiert.

Abstract

X-ray fluorescence (XRF) spectroscopy as an experimental tool for destruction-free elemental analysis is widely used and well accepted. The advent of X-ray optics has rendered lateral micro-analysis feasible. Through the use of two X-ray optics in a confocal arrangement, the third dimension - the depth of a sample - has become accessible. 3D Micro-XRF uses two polycapillary optics - one for the focusing of the excitation radiation and a second lens in front of an energy-dispersive detector. The overlap of the foci of the two optics forms a probing volume from which information is exclusively derived. In this work, the method of 3D Micro-XRF is presented experimentally and introduced as a new analytical tool. The emphasis of this work is laid on new quantification procedures.

The full quantification of 3D Micro-XRF measurements of stratified samples with monochromatic excitation has been developed and is described in detail. The quantification relies on a convolution of the shape and sensitivity of the probing volume with the investigated sample. Fluorescence and scattered radiation is used for the reconstruction of thickness and composition of the layers of stratified samples. With the help of especially manufactured reference samples the validity of the quantification model is demonstrated and proved.

In general, the overall detected intensity of a confocal measurement is lower compared to Micro-XRF because of the restricted probing volume. The quantification is more laborious and yields higher uncertainties. For each sample new quantification strategies must be developed in oder to optimally use the measured data. Nevertheless, 3D Micro-XRF proves to be one of the only methods, when sectioning or sampling of an object is not an option. The presented possibility of reconstruction of thickness and composition of layers of stratified samples renders this method into a true analytical tool.

The quantification of 3D Micro-XRF with X-ray tube excitation is more complex due to the fact that the excitation spectrum is transported with the first capillary lens instead of a monochromatic excitation line. First ideas concerning calibration and quantification procedures are discussed in this work.

Due to its non-destructiveness and the fact, that sample preparation is not necessary, 3D Micro-XRF has high potential as an analytical technique in the field of archaeometry. Advantages and inherent limitations of this new technique are discussed with the help of three application examples from this field. The heterogeneity of the objects and the lack of adequate reference samples requires the development of new quantification strategies. The addition of other X-ray methods such as Micro-XRF proves to facilitate the quantification process. Last but not least it is shown, that the careful qualitative analysis of 3D Micro-XRF measurements with X-ray tube excitation can give valuable information without the need for a full quantification or synchrotron radiation.

Contents

1 Introduction **1**

2 X-rays fluorescence spectroscopy **4**
2.1 Interaction of X-rays with matter 4
2.1.1 Photoelectric absorption 5
2.1.2 Scattering 5
2.1.3 X-ray refraction and total reflection 9
2.2 Experimental components 10
2.2.1 Sources 10
2.2.2 Detectors 13
2.2.3 X-ray Optics 15
2.3 X-ray Fluorescence Spectroscopy 20
2.3.1 Fluorescence production 20
2.3.2 Fluorescence intensity 22
2.3.3 Spectral evaluation 22
2.4 Micro-XRF and 3D Micro-XRF 24
2.4.1 Micro-XRF 25
2.4.2 3D Micro-XRF 26

3 Theory of 3D Micro X-ray Fluorescence Analysis **32**
3.1 Sensitivity 32
3.1.1 Optimal case 33
3.1.2 Displacement 35
3.1.3 MySpot setup 38
3.2 Fluorescence equation for homogeneous samples 41
3.2.1 Simulation 42
3.2.2 Scattering 45
3.2.3 Calibration 46
3.3 Stratified Samples 47
3.4 Polychromatic excitation 48
3.4.1 Theory 48
3.4.2 Thin Foils 50
3.4.3 Calibration 52
3.4.4 Reconstruction 54

4 Reconstruction of thickness and composition **55**
4.1 Calibration 56

4.1.1 Calibration routine . . . 56
4.1.2 Calibration functions . . . 59
4.1.3 Thin and thick reference material . . . 59
4.1.4 Different excitation energies . . . 60
4.1.5 Different angles between excitation axis and sample normal . . . 61
4.2 Validation . . . 64
4.2.1 Glass reference material . . . 64
4.2.2 Polymer samples . . . 66
4.3 Discussion of the reconstruction procedure . . . 68

5 Application examples **77**
5.1 Reverse paintings on glass . . . 77
5.2 Dead Sea Scrolls . . . 84
5.2.1 Qualitative analysis . . . 84
5.2.2 Quantitative analysis . . . 90
5.3 Black enamel . . . 97
5.3.1 Reference measurements . . . 98
5.3.2 Measurements of the 'Lüneburger Meditationstafel' . . . 102

6 Discussion, conclusion and outlook **108**

7 Danksagung **111**

Bibliography **112**

symbol	name	unit	page number
w_i	weight percent of element i	1	25
$\rho_i = \rho w_i$	local density of element i	g/cm^3	41
μ	mass attenuation coefficient	cm^2/g	4
$\bar{\mu}_{lin} = \bar{\mu}_i \rho$	effective linear mass attenuation coefficient	1/cm	22
σ_A/σ_D	spot size of excitation/detection lens	cm	32
T_A/T_D	transmission of excitation/detection lens	1	32
σ_y	width of probing volume normal to the sample	cm	34
η	integral sensitivity	1/cm	34
$\hat{\eta}(x, y, z)$	3D sensitivity	1/cm^2	34
$\bar{\eta}(x)$	sensitivity function	1	34
$d\sigma_C/d\Omega$	differential polarized Compton cross section	cm^2	7
$d\sigma_R/d\Omega$	differential polarized Rayleigh cross section	cm^2	7
σ_{Sc}	scattering coefficient	cm^2/g	46
σ_F	fluorescence production cross section	cm^2/g	21
θ_c	critical angle of total reflection	$^\circ$	10

Table 0.1: Table of frequently used symbols

1 Introduction

'X-ray (radiation beam): electromagnetic radiation of extremely short wavelength and high frequency, with wavelengths ranging from about 10^{-8} *to* 10^{-12} *metres and corresponding frequencies from about* 10^{16} *to* 10^{20} *hertz (Hz).' from Encyclopedia Britannica.*

The use of X-radiation as a tool for elemental analysis originates from experiments conducted as early as 1920s, including work by Moseley, Barkla, Bragg and Siegbahn [BKL$^+$06]. X-ray fluorescence spectroscopy (XRF) relies on the principle of attributing fluorescence generated by the de-excitation of atoms to specific electronic transitions in the electronic structure of these atoms. As destruction-free method it has gained wide acceptance in various application fields, like f.e. biology, geology, material science and archaeometry.

Through the advent of X-ray optics in the last decades of the last century, micro-analysis was made feasible, allowing lateral micro-investigation leading to elemental distribution maps with resolutions in the sub-micrometer regime. The use of polycapillary lenses has triggered increased micro-analysis with X-ray tubes, because with large angles of acceptance relatively high transmission values are achieved.

In this context the new method of 3D micro X-ray fluorescence spectroscopy (3D Micro-XRF) was developed in our research group [KMR03]. This method allows three-dimensionally resolved analysis employing two polycapillary optics in a confocal arrangement. Within the project 'Quantitative 3D Mikro-Röntgenfluoreszenzspektroskopie' funded by the German research foundation (DFG KA 925/7-1) the work on my PhD was conducted.

3D Micro-XRF is performed by a number of research groups worldwide. 3D Micro-XRF experiments have been carried out at synchrotron radiation sources [JPF04, WLS$^+$08, WMB$^+$06] as well as with X-ray tubes [LWS$^+$08, PH06, SHHB06, TN07]. While the usefulness of this method has already been shown for a number of applications, reliable quantification procedures are still a topic for further development. Establishing a reliable quantification procedure is the precondition to render this spectroscopic method into a true analytical tool.

With respect to quantification of 3D Micro-XRF in general, three papers have been published. Šmit et al. [SJPL04] proposed a quantification approach for layered systems, which has not been validated up to now. Vekemans et al. [VVBA04] reported a treatment of three-dimensional data sets by K-means clustering. This group is currently working on quantification schemes for the investigation of interstellar grains and coma particles from Comet 81P/Wild2 captured by a NASA sample return mission, as presented at the EXRS 2008 by Tom Schoonjans. The quantification does not take into account the size of the probing volume and is based on the analysis of intensity ratios, using reference

samples to obtain weight percent values and Kα to Kβ ratios for depth estimation. The work has not been published yet. P$\grave{e}$rez at al. [PSPR09] have recently published first results using a quantification scheme for polychromatic excitation for thin intermediate layers using equations developed by our group.

In our group, during the course of the PhD of Wolfgang Malzer [Mal04] a quantification concept for 3D Micro-XRF with monochromatic excitation was developed. A calibration procedure based on an expression for the primary fluorescence intensity for bulk material was published in [MK05]. Based on the proposed model for the three-dimensional sensitivity, in this work a quantification procedure for stratified samples could be developed, tested and validated [MMS$^+$08].

In comparison to XRF or Micro-XRF two main differences arise when using two optics in a confocal arrangement. The local densities of the elements - as opposed to their concentrations - prove to be the parameters which determine the fluorescence intensity. Additionally, the calibration constant in XRF must be replaced by a position- and energy-dependent sensitivity function.

The overlap of the foci of the two polycapillary lenses used in the confocal geometry forms a micro-volume. This probing volume can be expressed by a rotation-symmetric ellipsoid, with its half axes dependent on the spot sizes of the two optics and the applied geometry. By substituting the calibration constant from conventional XRF with this sensitivity function, the fluorescence intensity becomes a function of position and 3D analysis is made feasible. For samples with homogeneous layers depth profiling, i.e. the scanning of the sample through the probing volume in the normal direction to the sample surface, provides information of thickness and elemental composition of the layers.

The quantification is a two-step process. Characterization measurements during the course of this work have shown, that illumination and divergence effects alter the transmission and spot size functions of polycapillary halflenses considerably [WMM$^+$09]. Thus, in order to characterize the setup a calibration procedure is mandatory, as the characteristics of polycapillary X-ray lenses are highly dependent on the nature, i.e. divergence, spot size etc, of the transported radiation. Two new parameters, the width of the probing volume σ_y and the integral sensitivity η, are used to describe the probing volume. The calibration parameters are obtained by the analysis of depth scan measurements of thick glass reference materials.

The reconstruction of samples relies on the deconvolution of the sensitivity function (obtained by the calibration) and the sample composition and geometry. Prerequisites are the density of the individual layers as well as the dark matrix, i.e. the concentrations of elements outside the detectable range of elements. The detectable range is mainly dependent on the transmission function of the detection optic. For the optics used in this work, fluorescence can be measured between 3 keV to 19 keV. Validation measurements show, that the precision of the method is highly dependent on the sample complexity and the knowledge of the prerequisites. For simple geometries and few fluorescence elements uncertainties for the concentrations lie in the range of 10 - 20 %, while they can reach an order of magnitude for trace elements or elements with fluorescence energies at the borders of the detectable range. Thickness values generally show uncertainties of < 10 %.

The quantification process for X-ray tube based 3D Micro-XRF is more complex because the characteristic parameters are functions of excitation and fluorescence energy. Due to time restrictions only first ideas for calibration and quantification have been developed up until now.

The already mentioned necessity of knowing the dark matrix and the density of the radiation triggered the use of the scattering radiation for analysis. Compton scattering is directly dependent on the density of the sample and Rayleigh scattering is a function of density and matrix composition. In this work scattering was successfully used for the determination of thicknesses of layers without fluorescence elements as well as for the determination of layer densities. The combination of Micro-XRF with 3D Micro-XRF as well as the use of a newly developed compact 3D Micro-XRF spectrometer proved to be valuable additions to the technique for the analysis of real samples.

The work is arranged in four main chapters. In the first chapter the important aspects of X-ray fluorescence are introduced. Special emphasis is laid in the first section on scattering of X-rays. The experimental components used in this work are presented in the second section. The third section deals with X-ray fluorescence spectroscopy (XRF), including the fluorescence equation and spectral evaluation. The chapter ends with the introduction of Micro-XRF and 3D Micro-XRF as experimental techniques with details on the used setups.

In the second chapter the theory of 3D Micro-XRF is presented, starting with a detailed study of the probing volume. In the second section the fluorescence equation for thick homogeneous samples is introduced and demonstrated with a simulation example. Stratified samples are discussed in the third section. The difficulties encountered when dealing with polychromatic excitation are explained in the last section and first ideas for a quantification are expressed.

The third chapter deals with calibration and validation measurements. Calibration phenomena are explained in the first section and the optimal procedures are discussed. In the second chapter validation measurements [MMS$^+$08] are presented. A thick glass reference sample as well as especially manufactured stratified polymer samples [SMM$^+$09] are investigated. The chapter ends with a detailed description of the quantification possibilities and problems, presenting as a first reconstructed example car paint samples.

In the fourth chapter archaeometric application examples are described. A study on reverse paintings on glass could confirm the assumption of corrosion processes initiated at the glass/paint interface [KMM$^+$08]. The second example shows the importance of the use of scattered radiation with the example of highly degraded parchment samples [HWK$^+$07]. In the third section measurements on another reverse painting on glass are presented. Qualitative 3D Micro-XRF measurements conducted with a compact spectrometer prove to be sufficient for specific art historic questions, while synchrotron 3D Micro-XRF can be used in this case as a proof for the validity of the results.

2 X-rays fluorescence spectroscopy

X-ray fluorescence (XRF) spectroscopy is an analytical method which relies on the principle of excitation of atoms with X-rays and successive de-excitation accompanied by the emission of characteristic radiation. In its simplest form radiation from an isotropic source excites atoms in a sample and an energy-dispersive detector collects the characteristic line spectra, thus making non-destructive elemental analysis possible.

The first section of this chapter deals with theoretical considerations on the interaction of X-rays with matter and the underlying physical mechanisms. The second section introduces the experimental components with a special emphasis on the devices used in this work. The third section describes the X-ray fluorescence spectroscopy as an analytical technique.

With the advent of new X-ray optics, especially polycapillary lenses, micro-analysis has become feasible. Used for focusing X-rays onto small spots as well as for reducing the field of view of a detector, X-ray lenses render lateral and in depth resolution possible. Hence, the last section of this chapter explains the methods of Micro- and 3D Micro-XRF.

2.1 Interaction of X-rays with matter

An X-ray beam is attenuated when passing through matter. An absorber with thickness x and density ρ reduces the incoming photon count N_0 to

$$N(x) = N_0 \exp(-\mu\rho x) = N_0 \exp(-\mu_{lin} x) \tag{2.1}$$

with $\mu[\mathrm{cm}^2/\mathrm{g}]$ the mass attenuation coefficient and $\mu_{lin}[1/\mathrm{cm}]=\mu\rho$ the linear mass attenuation coefficient. The mass attenuation coefficient can be derived from the atomic attenuation coefficient $\mu = (N_A/A)\mu_{Atom}$ with N_A the Avogadro constant and A the atomic mass, which can be calculated.

The mass attenuation coefficient μ describes the processes which occur during the interaction of a photon with matter in the X-ray regime. For the X-ray range used in this work it is the sum of the mass photoelectric absorption coefficient τ and the coherent and incoherent mass scattering coefficient σ

$$\mu = \tau + \sigma_{coh} + \sigma_{incoh} \tag{2.2}$$

These processes will be explained in detail in the following section.

2.1.1 Photoelectric absorption

The process of photoelectric absorption involves the transfer of the photon energy to one of the core electrons of an atom, resulting in its ejection from the atom. Electrons from outer shells of the atom fill the generated hole, returning the atom to its non exited state. The loss in potential energy is either emitted as a fluorescence photon or induces Auger or Coster-Kronig transitions. The energy of the emitted fluorescence photon corresponds to the energy difference of the involved shells of the atom. Fluorescence analysis relies on the principle of attributing fluorescence to specific atoms. The measured discrete fluorescence lines are broadened through natural line width and detector artifacts, see section 2.2.2.

	L1	L2	L3	M1	M2	M3	M4	M5	N1	N2	N3	N4	N5	O4/5
L3				Ll			Lα2	Lα1	Lβ6			Lβ2	Lβ2	Lβ5
L2				Lν			Lβ1					Lγ1		Lγ6
L1					Lβ4	Lβ3				Lγ2	Lγ3			
K		Kα2	Kα1		Kβ3	Kβ1	Kβ5	Kβ5		Kβ2	Kβ2	Kβ4	Kβ4	

Table 2.1: Nomenclature of X-ray lines. The Siegbahn notation (f.e. Kα1) was developed historically and according to intensity, while the IUPAC notation (f.e. K-L3) is based on the shells involved in the fluorescence emission process.

A nomenclature is necessary for the differentiation of the emitted fluorescence radiation. Table 2.1 shows the two most common notations - the IUPAC as well as the Siegbahn notation. If the relaxation process involves an electron falling from the M5 shell to the L3 shell, the transition is labeled M5-L3 (IUPAC) or Lα1 (Siegbahn). In this work both nomenclatures will be used.

2.1.2 Scattering

Two kinds of scattering may take place when a photon interacts with an atom:

- incoherent or inelastic or Compton scattering; the change of propagation direction is accompanied with an increasing of wavelength and change of phase
- coherent or elastic or Rayleigh scattering; phase and energy are not affected

In figure 2.1 the Compton and Rayleigh cross section are plotted as functions of atomic number and photon energy. The probability for Compton scattering increases with increasing photon energy and decreasing atomic number of the scattering atom. Rayleigh scattering increases with increasing energy and decreasing atomic number. The next two sections explain the mechanisms for these characteristics.

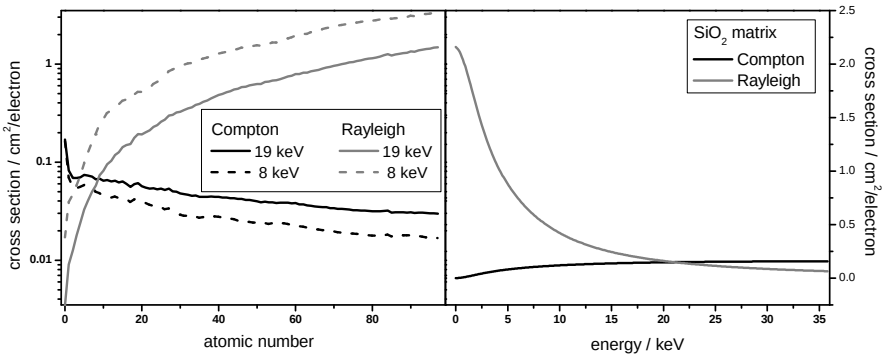

Figure 2.1: Compton and Rayleigh scattering cross sections as a function of energy of the incoming photon and atomic number of the scattering atom.

Inelastic scattering

Inelastic or Compton scattering occurs when a photon interacts with a free electron at rest changing its energy and/or phase. This scenario is as a first approximation given for electrons in the outer shells of atoms and for high energy photons. In such cases the weak binding of the electrons to the atom may be neglected, because the momentum transferred to the electron greatly exceeds the momentum of the electron in the bound state. Considering conservation of energy and momentum the wavelength change of the scattered photon is

$$\Delta\lambda = \frac{h}{m_e c}(1 - \cos(\theta)) \tag{2.3}$$

with θ the scattering angle, h the Planck constant, m_e the mass of the electron at rest and c the speed of light. The change of wavelength is a function of scattering angle and independent on the energy of the incoming photon as well as the scattering atom.

The shape of the Compton peak in an XRF spectrum has a broader shape than the fluorescence lines. Due to the relative motions of the electrons involved, a Doppler broadening can be observed. Additionally, in an XRF experiment the angle θ is not discrete, but a scattering over a small series of angles is measured. The broadening of the Compton peak can be expressed by [Dum33]

$$4\beta\lambda \sin(\frac{\theta}{2}) \tag{2.4}$$

with $\beta = v/c$ for electrons moving in random directions with the velocity v.

In case of polarized monochromatic radiation the probability for Compton scattering can be described by the differential cross section [VJA+95]:

$$\frac{d\sigma_C}{d\Omega} = \frac{d\sigma_{KN}}{d\Omega} S(q,Z) = \frac{r_e^2}{2}\left(\frac{K}{K_0}\right)^2 \left(\frac{K}{K_0} + \frac{K_0}{K} - 2\sin^2(\theta)\cos^2(\phi)\right) S(q,Z) \tag{2.5}$$

with $S(q,Z)$ the incoherent scattering function, q the momentum transfer, $d\sigma_{KN}/d\Omega$ the Klein-Nishina differential scattering cross section, r_e the classical electron radius and

$$\frac{K_0}{K} = 1 + \frac{E}{m_e c^2}(1 - \cos(\theta)) \tag{2.6}$$

θ is the scattering angle and ϕ the angle between the electric field vector of the incoming photon and the scattered photon, see figure 2.2.

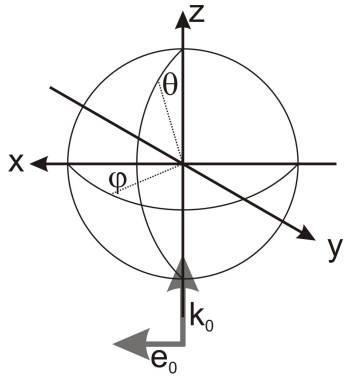

Figure 2.2: Coordinate system for scattering angles

The incoherent scattering function accounts for the phase differences between the waves scattered by the electrons in the atom and the fact, that not all electrons are loosely bound to the atom core. It can be calculated in terms of the atomic ground state wave function. Values lie between $S(0,Z) = 0$ to $S(\infty,Z) = Z$ and have been tabulated for $Z = 1$ to $Z = 100$ [HVB+75].

Elastic scattering

Elastic or Rayleigh scattering is a process in which a photon is scattered by a bound atomic electron changing its direction without energy loss and with a definite phase relation between the incoming and scattered waves. The electro-magnetic field of the incident photon accelerates the electrons in an atom which then emits dipole radiation. The intensity of the radiation is determined by summing the amplitudes of the radiation coherently scattered by each of the Z electrons [GM01].

Rayleigh scattering is the dominant process for low energy photons. The differential polarized Rayleigh cross section can be written as

$$\frac{d\sigma_R}{d\Omega} = \frac{d\sigma_T}{d\Omega} F^2(q,Z) = r_e^2\left(1 - \sin^2(\theta)\cos^2(\phi)\right) F^2(q,Z) \tag{2.7}$$

with $F(q, Z)$ the atomic form factor and $d\sigma_T/d\Omega$ the Thomson differential scattering cross section. The atomic form factor takes the phase differences between the waves scattered by the Z electrons in the atom into account. It is maximal for scattering in the forward direction (no phase change [TC82]) and proportional to Z^2. Values can be obtained by tabulated calculations [HO79].

Scattering of polarized radiation

In this work most theoretical considerations have been done for synchrotron radiation, which is linear polarized in the plane of the used storage ring. Therefore it is useful to take a closer look at equations 2.5 and 2.7. Figure 2.3 shows the differential polarized scattering cross sections for Compton as well as Rayleigh scattering for two energies (E = 19 keV and E = 8 keV) in a SiO_2 matrix.

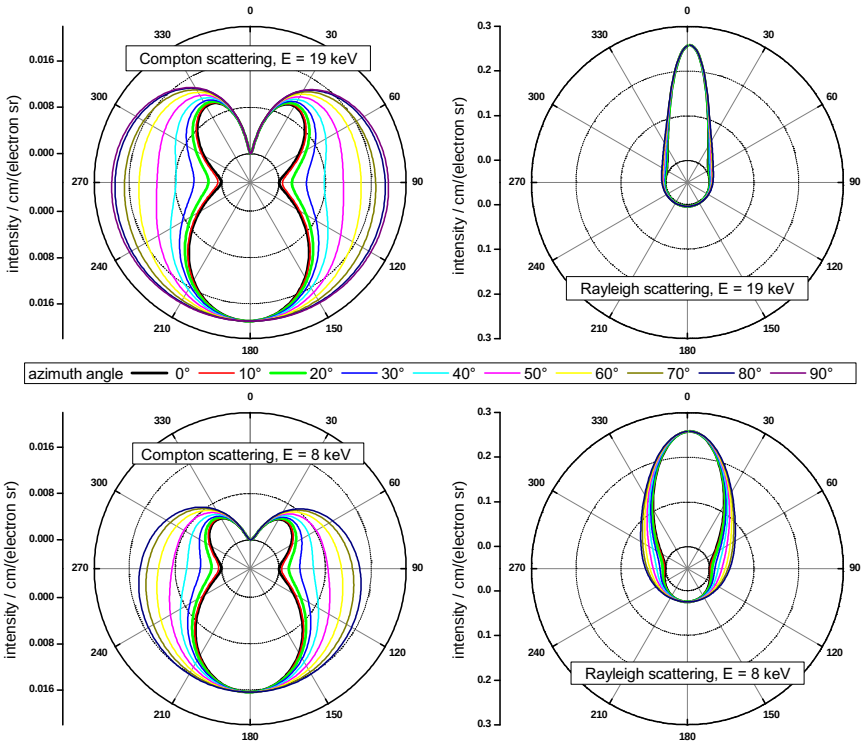

Figure 2.3: Angle dependency for the differential polarized Compton and Rayleigh cross sections at E = 8 keV and E = 19 keV.

For high photon energies Rayleigh scattering is mainly forward directed, confined to small angles. The lower the energy, the bigger the angular spread. Rayleigh scattering is as a first approximation independent on the azimuth angle.

Compton scattering in minimal for $\theta = 90°$ and $\theta = 270°$ as well as in the ring plane. Forward scattering is not allowed.

2.1.3 X-ray refraction and total reflection

The macroscopic interaction of X-rays with matter can be described with the complex refraction index:

$$\tilde{n} = 1 - \delta - i\beta = 1 - Kf_1 - iKf_2 \tag{2.8}$$

with $f_1 \approx Z$ and $f_2 \propto E\mu(E)$ the atomic scattering factors and

$$K = \frac{r_e}{2\pi}\frac{N}{Z}\lambda^2 \tag{2.9}$$

where N is the number of electrons per cubic meter, r_e the classical radius of the electron and λ the radiation wavelength. While β describes the absorption of radiation in a medium, the decrement δ determines the refractive properties.

X-rays have the special characteristic, that the real part of the complex refraction index, which is responsible for reflection, is slightly smaller than one, making vacuum the optically densest medium. It can be written as

$$n = 1 - \delta = 1 - \frac{r_e}{2\pi}N\lambda^2 \tag{2.10}$$

With $N = \frac{ZN_A}{A}\rho$ and λ given in Ångstrom a good approximation can be found

$$\begin{aligned} \delta &= 2.72 \cdot 10^{-6}\frac{Z}{A}\rho\lambda^2 \\ &\approx 1.3 \cdot 10^{-6}\rho\lambda^2 \end{aligned} \tag{2.11}$$

as Z/A is approximately 0.5 throughout the whole periodic table [Gui94]. Thus, with wavelengths between 0.005 Å and 124 Å (100 eV < E < 250 keV), the difference of refractive index to one is very small. This explains the low reflection and refraction capabilities of X-rays in any matter.

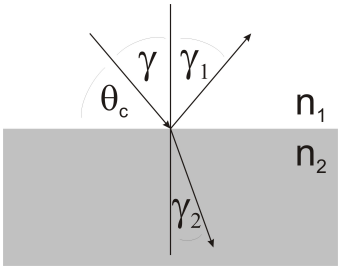

Figure 2.4: X-ray refraction scheme.

On the other hand, total reflexion phenomena are feasible for grazing incidence angles, because any solid state material is optically thinner than air. The Snellius equation for a system as shown in figure 2.4

$$\frac{\sin(\gamma_2)}{\sin(\gamma)} = \frac{n_1}{n_2} \tag{2.12}$$

leads for $\gamma_2 = 90°$ and $n_1 = 1$ to

$$\sin(\gamma) = \cos(\theta_c) \approx 1 - \frac{\theta_c^2}{2} = n_2 \tag{2.13}$$

with θ_c the critical angle for total reflection. By comparison with equation 2.11 and with $E = hc/\lambda$ we obtain

$$\begin{aligned} \theta_c &\approx (2\delta)^{1/2} \approx 1.6\sqrt{\rho}\lambda \\ &\approx 20\frac{\sqrt{\rho}}{E} \end{aligned} \tag{2.14}$$

with E in keV, ρ in g/cm^3 and θ_c in mrad. Typical values for a glass sample with ρ = 2.5 g/cm^3 are 1 - 20 mrad. For the Mo-Kα radiation at 17.4 keV the total reflection angle is 2 mrad, for Mo-L radiation at 2.3 keV it increases to 14 mrad.

2.2 Experimental components

As already mentioned, XRF is based on the excitation of atoms in a target and the collection of the characteristic fluorescence radiation. Numerous kinds of setups are imaginable with different sources and detectors. This section deals with these two aspects of XRF and additionally introduces polycapillary optics which may act as a means for optimizing setup geometries.

2.2.1 Sources

X-rays are produced mainly with the help of two processes, acceleration of charged particles (synchrotron and tube bremsstrahlung) and de-excitation of atoms (characteristic X-rays of tubes). In the following two sections the two X-ray sources used in this work are briefly described.

X-ray tubes

X-ray tubes rely on the principle of bombarding an anode with high energy electrons in a vacuum chamber. The electrons are scattered by the anode atoms. While elastic scattering is the dominant process, inelastic scattering can also occur. Inelastic scattering, i.e. the deceleration of the electrons, induces a continuous bremsstrahlung spectrum. Additionally the electrons can excite atoms from the anode which successively emit characteristic radiation.

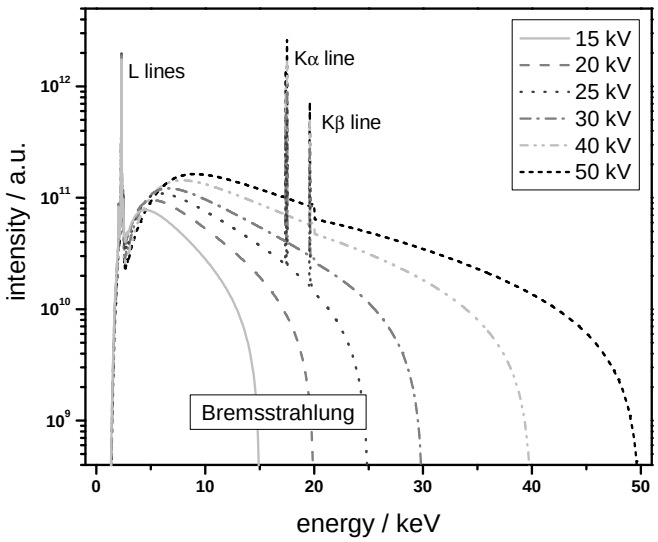

Figure 2.5: Calculated spectra of a Mo X-ray tube for different acceleration voltages. Characteristic K- and L-lines and the Bremsstrahlung spectrum can be distinguished.

In figure 2.5 simulated X-ray spectra are depicted for different acceleration voltages of an X-ray tube. The spectra are calculated with the Ebel equations [Ebe99] for a Mo-X-ray tube with a take off angle of 17°, a Be-window of 128 µm thickness and energy intervals of ΔE = 0.1 keV.

An accelerated electron emits a photon with an energy which is dependent on the scattering angle of the electron. Due to the undirected and random scattering the radiation has a broad bandwidth leading to a bremsstrahlung background. The background increases with increasing energy, reaches a maximum, decreases and has a cut-off energy depending on the acceleration voltage. The shape of the bremsstrahlung spectrum depends mainly on the acceleration voltage. The maximum of the spectrum shifts with increasing acceleration energy and the ratio of characteristic radiation to bremsstrahlung changes. The minimal emitted wavelength can be calculated with

$$\lambda_{min}[nm] = \frac{1.24}{E[keV]} \tag{2.15}$$

,while the wavelength of maximal intensity is roughly 1.5 λ_{min}.

When the impinging electrons have enough energy to produce a vacancy in the inner shells of an atom, it will successively be filled by an electron from a higher level. The loss in energy of the de-excitation process can be emitted through a characteristic X-ray. In figure 2.5 the spectra with an acceleration energy $\geq$25 keV show characteristic K- and

L-lines, because the K-edge of Mo is at 20.001 keV, while the other two spectra show only characteristic L-lines. The emission efficiency is a function of the overvoltage U_0 expressed by the ratio of the initial electron energy E_0 and the absorption edge energy E_{edge}, having a maximum at $U_0 \approx 3 - 4$ [GM01].

The total irradiated power P of a X-ray tube can be expressed for an anode material with the atomic number Z [BKL$^+$06]:

$$P[\text{kW}] = CZIU^2 \tag{2.16}$$

with I[A] the anode current, U[kV] the acceleration voltage and $C \approx 10^{-6}[\text{kV}^{-1}]$ a constant. The efficiency of an X-ray tube is of the order of 0.1 - 1 %, leading to a high thermal energy dissipation at the anode.

Synchrotron

The radiation emitted by electrons which are accelerated with a velocity $v \approx c$ in a circular path is called synchrotron radiation. Due to the relativistic properties of the electrons, this radiation has a few special characteristics.

1. The bandwidth of synchrotron radiation reaches from the infrared region to hard X-rays (eV to keV).

2. The irradiated power P of one electron can be expressed by

$$P = \frac{2e^2c}{3R^2}\gamma^4 \propto E^2B \tag{2.17}$$

   with $\gamma = E/m_ec^2$ and the orbit radius $R \propto E/B$ [Jac67]. The brilliance of the radiation, defined by the number of photons in an energy interval of 0.1% bandwidth emitted into angular intervals $d\theta$ and $d\psi$ at angles θ and ψ from an infinitesimal source area, can reach as high as 10^{18} photons / s / mm^2 / mrad^2 / 0.1 % BW (in comparison: X-ray tubes have a 10^{-10} times lower brilliance).

3. The characteristic wavelength λ_c, which is defined as the median wavelength of the synchrotron spectrum, is

$$\lambda_c = \frac{4\pi R}{3\gamma^3} \tag{2.18}$$

4. The radiation leaves the ring orbit in a narrow cone with a divergence of $\Psi \approx 2/\gamma$ [rad].

5. The polarization of the synchrotron beam is linear in the ring plane, with elliptical polarization components underneath and above the ring plane.

In a synchrotron facility electrons must be accelerated to very high (relativistic) energies, typically ranging from a few hundreds of MeV to several GeV. This is done with the help of different acceleration stages. In the following the synchrotron facility BESSY II will be described as an example.

At BESSY II electrons are produced in a high vacuum with a hot cathode and accelerated with an extraction energy of 100 keV. Then they are fed into a microtron with a rf-accelerator. The electrons are grouped into bunches with an energy of 50 MeV. These pulses are accelerated to 1.7 GeV in the synchrotron and then fed into the storage ring.

In the storage ring the electrons are forced onto a quasi-circular orbit with the help of dipole magnets, with quadrupoles the repulsion between the electrons is compensated and with sextupoles the ring orbit is corrected, so that a high life time is guaranteed.

In order to adjust radiation characteristics to experimental needs, magnetic insertion devices are used which introduce no overall deflection in the ring orbit. The critical photon energy from such devices is dependent on the magnetic field and the particle energy. Many different geometries and setups are possible. While wavelength shifters and wigglers are used to shift the characteristic wavelength to smaller values or enhance the radiation intensity, undulators may be used for optimizing the beam quality by maximizing its brightness or for providing specific characteristics like elliptical polarization [Wie02].

In this work, measurements were performed at two beamlines of BESSY II, which will be described in section 2.4.2. Both beamlines have the same superconducting 3-pole wavelength shifter [BDF+01] as source. Only the middle dipole with a maximum field of 7 T acts as the radiation source, while the other two normal conducting magnets with fields of 1.5 T compensate the beam deflection. The energy range is about 2 keV to 80 keV and the polarization is in the ring plane.

2.2.2 Detectors

The detection of X-rays relies on the interaction of the X-rays with matter. The most commonly used devices in energy-dispersive XRF are semiconductor detectors. An impinging X-ray produces a high energy electron, which creates a number of electron-hole pairs $n_{pair} = E_{ph}/\epsilon$, where ϵ is the average energy needed for the pair production. A charge cloud is generated. The electrons and holes are then extracted by a high voltage to an anode and a cathode, creating a charge signal. In the following detector electronics, this signal is shaped and amplified, resulting in a stable voltage pulse. The amplitude of this pulse is proportional to the energy of the impinging X-ray photon, thus making energy-dispersive detection feasible.

In its simplest form a semiconductor detector consists of a crystal with a pn-junction. When the diode is reverse biased, an intrinsic depletion zone is formed without free charge carriers. This depletion zone acts as the interaction zone of the detector. As the detected voltage is inversely proportional to the capacity of the junction, modern semiconductor devices aim at broad depletion zones and small contacts.

The detection efficiency η, defined as the ratio of incoming to detected photons, is the product of the geometric efficiency η_{geom}, the intrinsic efficiency η_i and the photo peak efficiency η_{photo}:

$$\eta = \eta_{geom} \cdot \eta_i \cdot \eta_{photo} \tag{2.19}$$

The geometric efficiency is a factor arising from the fact, that only photons, which are emitted into the detection angle can be captured. The intrinsic efficiency describes the

probability, that the photon interacts in the area of detection. The photo peak efficiency characterizes the fraction of the photons interacting in the detector, which deposit their full energy in the material.

A measured fluorescence line is broadened in a way, that it can be described by a Gaussian distribution

$$G(E) = \frac{N_0}{\sigma\sqrt{2\pi}} \exp\left(-\frac{(E-E_c)^2}{2\sigma^2}\right) \tag{2.20}$$

with $\sigma = FWHM/2.335$ the standard deviation, N_0 the net peak area and E_c the peak centroid. The standard deviation includes several broadening factors, like the electronic noise σ_{el} or the statistical noise $\sigma_{stat} = \sqrt{F(h\nu/\epsilon)}$, with F the Fano factor and $h\nu$ the energy of the fluorescence line.

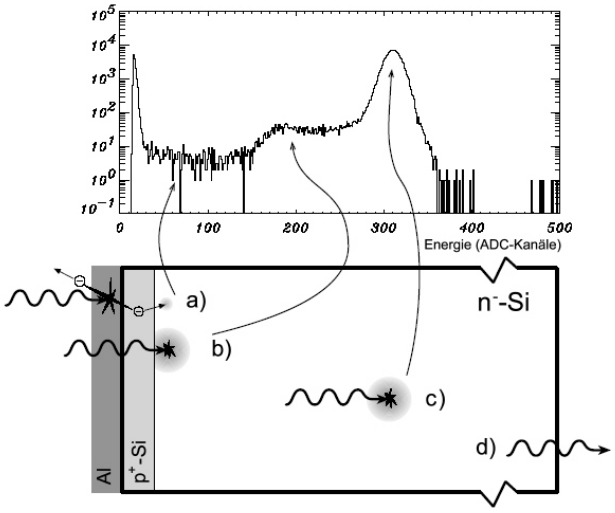

Figure 2.6: Response function of a semiconductor X-ray detector [Egg04]

Additional to this broadening detectors introduce artifacts into the spectrum, see figure 2.6 [Egg04]:

- **Escape peak:** When the impinging photon interacts with the crystal, a characteristic X-ray photon is produced. If this photon is not reabsorbed and leaves the detector, the voltage pulse is reduced, thus, leading to the detection of a fluorescence photon at $h\nu - E_{atom}$, with E_{atom} the fluorescence line energy of the detector crystal atoms. For silicon based detectors E_{atom} is equal to the Si Kα fluorescence at 1.74 keV.

- **Pile-up peak:** If two photons reach the detector in a time which is shorter than the pulse pair resolution, i.e. in a time in which the detector electronics cannot

discriminate between the two events, a peak at the sum of the two photon energies will be detected.

- **Tail:** A photon interacting in the detector close to the front contact or the side of the crystal creates a charge cloud, which may not lie completely inside the detector, see b) in figure 2.6. Charge carriers can recombine outside the active volume of the crystal. This incomplete charge collection changes the Gaussian shape of a fluorescence line to have an asymmetric tail to the low energy side. When considering a symmetric charge cloud around the first interaction the minimal energy of the tail-photon is half the energy of the fluorescence line.

- **Shelf:** The impinging photon can loose energy in two more situations. When the first interaction occurs in the front contact, high energy photo- or Auger-electrons can reach the detection zone, see a) in figure 2.6. On the other hand, when the first interaction is in the detection zone, high energy photo- or Auger-electrons can leave the detector, thus reducing the detected photon energy.

Two widespread silicon based devices are Li-drifted Si-detectors (Si(Li)) and silicon drift detectors (SDD).

Si(Li): In order to enhance the intrinsic detections zones, the weakly p-type silicon is doted with n-type lithium. Intrinsic zones of 10 mm can be achieved with this method, thus reducing the capacity considerably. A disadvantage is, that the lithium ions are very mobile, making it mandatory to cool the detector permanently with liquid nitrogen. Typical energy resolutions are 135 eV at 6 keV.

SDD: Silicon drift detectors have low electronic noise, short shaping times and low capacitance due to a new geometry, which integrates the pre-amplifying FET onto the detector chip. The energy-resolution is nowadays comparable to Si(Li) detectors and considerably high pulse throughput is achieved without detector cooling.

2.2.3 X-ray Optics

The fact that the refractive index for X-rays differs only slightly from one (10^{-5}), see section 2.1.3, makes X-ray focusing with refraction based optics difficult. The small refraction angle and the consequently high absorption of the radiation due to long paths in the medium have made such optics feasible only for synchrotron radiation. Optics based on diffraction are widely used in synchrotron source facilities.

The necessity for large deflection angles has triggered a new branch of X-ray optics based on the transport of radiation in hollow glass capillaries by total internal reflection. In this work solely polycapillary lenses have been used and will therefore be discussed in the following, only .

Polycapillary optics consists of thousands of bundles of hollow glass capillaries with different curvatures, to ensure a focusing or collecting characteristic. Figure 2.7 shows two types of polycapillary optics and their use. A full lens collects radiation from a spot source and focuses it. A halflens can be used for focusing parallel radiation as well as for collecting radiation from a spot source and parallelizing it.

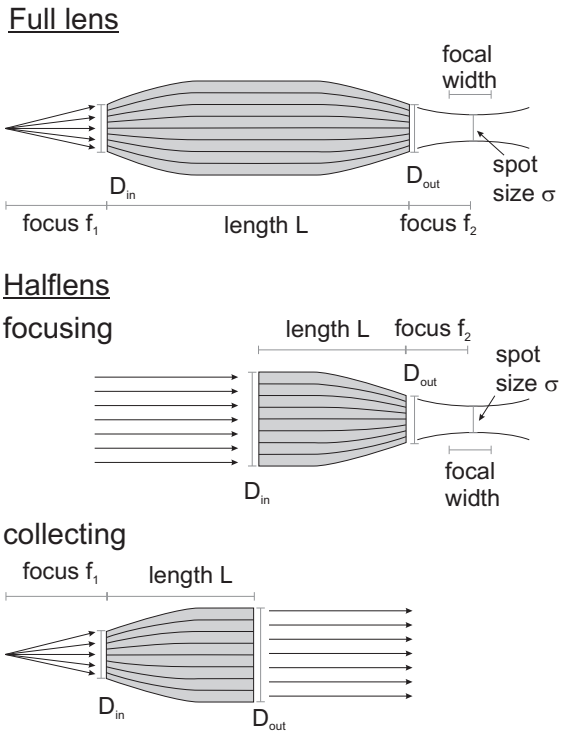

Figure 2.7: Polycapillary full and halflens: While full lenses focus radiation from a spot source onto a spot, halflenses can be used to focus parallel radiation (focusing mode) or collect radiation from a spot source (collecting mode).

The photon flux distribution of a polycapillary optic in the focal plane (halflens in focusing direction and full lens) as well as the acceptance area of a polycapillary full lens and a halflens used in collecting direction can be described by a Gaussian intensity distribution [WMM+09]. Polycapillary optics are characterized via two parameters, the spot size σ in the focal plane and the gain factor G.

The **gain factor** G is the measure for the enhancement of flux by a polycapillary compared to the use of a collimator. It is defined as the ratio of the photon flux in the middle of the focal spot with a polycapillary to the photon flux without polycapillary, the middle being defined by a pinhole. The gain is therefore dependent on the size of the used pinhole and the distance between lens and focus.

The **spot size** σ is the diameter of the focal or acceptance spot, where the Gaussian intensity distribution has reached the $1/e$-value of the maximal value. The spot size can be converted to the full width half maximum (FWHM) with the following relation

$$FWHM = 2\sqrt{2\ln(2)}\sigma \tag{2.21}$$

Depending on the geometry of the lens, the spot size does not change considerably in the region of focal width, see figure 2.7. For the used polycapillary lenses in this work the focal width is in the order of 200 µm.

The gain as well as the spot size of a polycapillary lens are energy-dependent values due to the energy-dependence of the angle of total reflection. The relation between spot size σ, gain factor G and transmission T can be described by

$$T \propto \sigma^2 G \tag{2.22}$$

The transmission is in this case defined as the fraction of the radiation which falls onto the entrance of the optic in respect to the radiation which is transported to the focus. The transmission comprises position-dependent information as it is proportional to the energy-dependent spot size.

Theoretical considerations

Polycapillary optics consist of thousands of bundles of hollow glass tubes with varying curvature. While the mechanisms of straight monocapillaries can be calculated, the simulation of polycapillary lenses is demanding due to energy- and position-dependent factors. Monte-Carlo methods have been successfully applied [HDCC07], but they can only be valid for ideal lenses and ideal setup alignments. In this section a few simple considerations will be discussed. For both the spot size as well as for the transmission of a polycapillary lens phenomenological fitting functions will be introduced.

Transmission

The transmission of a polycapillary lens has a maximum and decreases to both lower and higher energies. The decrease toward higher energies can be explained by the lower acceptance due to the decrease of the total reflection angle. Additionally, the different curvatures of the capillaries in the lens affect the transmission (shading effect). The reflectivity decreases to lower energies, which explains the decrease of the transmission to the low energy side.

Shading effect

The capillaries of polycapillary optics have position-dependent curvatures R. Outer capillaries are bent stronger than capillaries close to the middle of the lens. The radiation capture of a bent capillary is smaller than that of a straight capillary due to a shading effect, see figure 2.8.

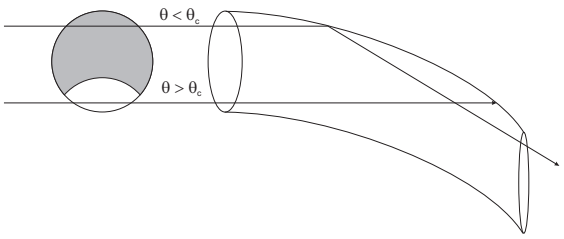

Figure 2.8: The radiation capture of a bent capillary than that of a straight capillary due to a shading effect.

The degree of capture can be expressed by

$$1 > \gamma_c = \frac{R\theta_c^2}{2d} \tag{2.23}$$

, with d the diameter of the capillary and θ_c the critical angle for total reflection. Thus, the maximal transmission is reduced, the bigger the curvature of the capillary.

Multiple reflections on a curved surface

When a photon falls upon a surface it can be reflected in an angle $\theta \leq \theta_c$, only. By means of multiple reflexions on curved surfaces bending angles $\Phi >> \theta_c$ can be achieved. The multiple reflection index is defined as

$$R_0 \approx \exp(-\Phi\beta\delta^{-3/2}) \tag{2.24}$$

With $\delta \propto E^{-2}$ (see equation 2.11) and $\beta \propto E^{-1}\mu(E)$, the reflectivity follows the rule

$$R_0 \propto \exp(-\Phi E^2\mu(E)) \tag{2.25}$$

In the energy range where the mass attenuation coefficient μ is dominated by the photoelectric absorption coefficient τ, that means especially between absorption edges, the reflectivity increases (due to the relation $\tau(E) \propto 1/E^3$, see equation 2.30). For higher energies, the E^2-term in relation 2.25 dominates and the reflectivity decreases.

Maximal spot size

The spot size for an ideal straight monocapillary lens with an diameter d and a focal distance f_2 can be expressed by [BKL+06]

$$\sigma \approx d + 2\theta_c f_2 \tag{2.26}$$

neglecting absorption, illumination and divergence effects. Although polycapillaries consist of thousands of bundles of monocapillaries, utilizing equation 2.26 for quick calculation yields spot sizes in the right order of magnitude.

In order to find a description of the spot size as a function of transported radiation energy, equations 2.26 and 2.14 can be used, leading to a function

$$\sigma(E) = \sigma_0 + \frac{\sigma_1}{E} \tag{2.27}$$

with σ_0 and σ_1 free parameters.

The enhanced absorption in the relatively longer photon paths in the outer capillaries in respect to the straight middle capillaries leads to a decrease of the spot size toward low energies. This effect is more pronounced for full lenses or half lenses with extremely bent outer capillaries. In this case equation 2.27 cannot be used, but a peak function must be found for the description.

Characterization

In 3D Micro-XRF a polycapillary halflens is placed in collection mode in front of a detector. The intensity distribution which is collected by this lens is an important factor for quantification. This so-called acceptance distribution describes the area from which the lens collects radiation. For quantification it is assumed that the acceptance distribution is a two-dimensional Gaussian function [MK05], see section 3.1.

While polycapillary lenses have been characterized in the focusing direction extensively [GP03, GJSX99, BEB$^+$08], only the divergence at the output of the optics has been characterized for the collecting direction. Ray-tracing simulations have been performed to understand radiation transport [HDCC07, CCV$^+$94], but not in order to characterize the acceptance area.

In the course of the work characterization measurements have been performed, which are described in detail in [Wol09]. The aim was to prove the assumption, that the acceptance area of a polycapillary halflens can be described by a Gaussian intensity distribution. A polycapillary halflens was investigated in focusing direction (knife-edge scans) and in collecting direction (electron and proton beam as point-like sources). Electron measurements were performed with a scanning electron microscope of the Zentraleinrichtung Elektronenmikroskopie der Technischen Universität Berlin (ZELMI) in Berlin, Germany. The lens was additionally characterized with a proton beam at the Jožef Stefan Institute in Ljubljana, Slovenia.

The investigation in the collecting direction proved for the first time, that the acceptance area of a polycapillary can be described by a Gaussian intensity distribution. Another important result of these measurements is, as described extensively in [WMM$^+$09], that the use of the optic alters spot size and transmission.

Figure 2.9 shows the results for spot size and transmission of the lens. The spot size of the investigated lens is a monotonically decreasing function of energy. In the left graph of figure 2.9 the certified values given by the manufacturer, the experimental results and a calculation using equation 2.26 are displayed. The divergence of the transported radiation in collecting mode is energy-dependent, while it is determined by the divergence of the synchrotron beam and, thus, constant for the focusing mode measurements. The result is, that the spot size of the investigated lens is smaller for the focusing direction because of the divergence difference (mySpot beamline < 1 mrad : total angle of reflection $\theta_c(20\text{ keV}) \approx 1.6$ mrad).

The transmission of the polycapillary halflens measured in collecting and focusing direction as well as the certified values are displayed in the right graph of figure 2.9. Due to the fact, that the lens was not fully illuminated during the synchrotron measurements (beam size 300 µm - $D_{in} = 2.1$ mm), the transmission function differs in the higher energy region.

As an additional result of these measurements a description for the transmission functions of polycapillary halflenses was found. The transmission can be described by a peak function of the form

$$T = T_0 + T_1 \exp(-\exp(-z(E)) - z(E) + 1) \tag{2.28}$$

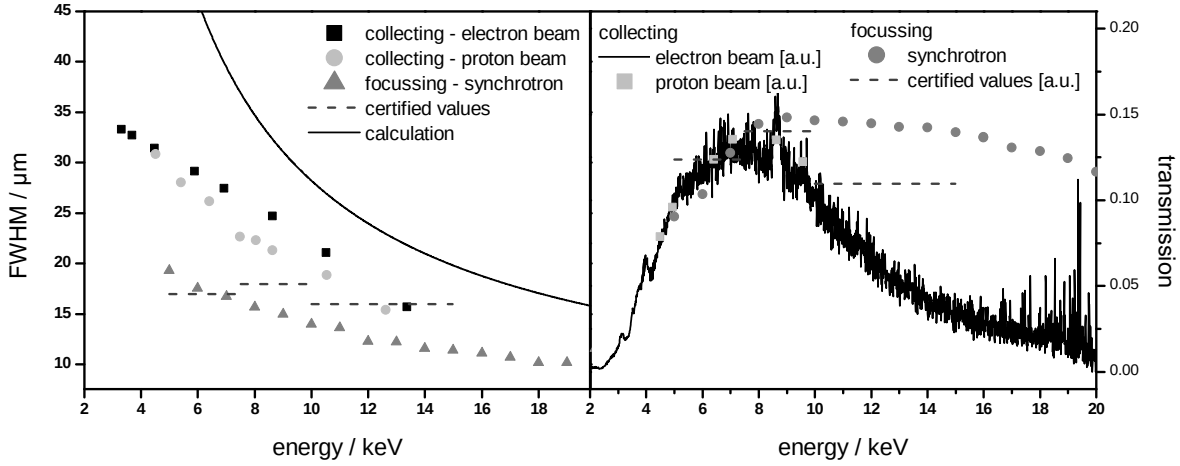

Figure 2.9: Characterization measurements of a polycapillary halflens in collecting direction (electron and proton beam) and focusing direction (synchrotron radiation).

with $z(E) = (E - E_c)/T_2$ and T_0, T_1, T_2 and E_c free parameters. The use of this so-called extreme function cannot be motivated in a physical context, but it has proved to be a function, which describes the experimental results very well.

The described characterization measurements show, that illumination and divergence effects may lead to extremely different characteristics of polycapillary X-ray optics. And this fact necessitates calibration procedures, as an absolute characterization of polycapillary lenses is not possible.

2.3 X-ray Fluorescence Spectroscopy

In the first section of this chapter the interactions of X-rays with matter have been described. Fluorescence can be induced in a target when bombarded with X-rays. The use of this characteristic fluorescence radiation for element specific analysis is called X-ray fluorescence spectroscopy (XRF).

2.3.1 Fluorescence production

The probability of the emission of a characteristic X-ray line can be described by the **fluorescence production cross section** σ_F. It is defined as the product of total photoelectric absorption cross section or mass photoelectric absorption coefficient τ,

jump factor j, fluorescence yield ω and the transition probability g:

$$\sigma_F = \tau j \omega g \tag{2.29}$$

The **mass photoelectric absorption coefficient** is composed of the absorption coefficients of all the shells of an atom $\tau = \tau_K + \tau_{L1} + \tau_{L2} + \tau_{L3} + \tau_{M1} + ...$ Derived from the Bragg-Pierce law [TC82] one finds the expression

$$\tau = C Z^\beta \lambda^\alpha \propto \frac{1}{E^\alpha} \tag{2.30}$$

where $2.2 < \alpha < 3.0$ and $2.5 < \beta < 3.5$ and C is a constant. Equation 2.30 is only valid in certain wavelength intervals, namely for wavelengths between absorption edges. In practice tabulated experimental values are used.

At the absorption edges τ has a discontinuity. This so-called jump is described by the jump ratio, the ratio of the mass attenuation coefficient at the higher and lower energy sides of the edge. For example the jump ratio S_K at the K edge is

$$S_K = \frac{\tau}{\tau - \tau_K} = \frac{\tau_K + \tau_{L1} + \tau_{L2} + \tau_{L3} + \tau_{M1} + ...}{\tau_{L1} + \tau_{L2} + \tau_{L3} + \tau_{M1} + ...} \tag{2.31}$$

The **jump factor** j is then defined as the fraction of the total absorption that is associated with a given level for a given interval of wavelengths, f.e. for the K edge:

$$\tau_K = \frac{S_K - 1}{S_K} \tau = j_K \tau \tag{2.32}$$

The **fluorescence yield** is the probability that a fluorescence photon will be emitted by the atom. The competing process is the Auger decay. The energy obtained by the de-excitation of the atom is transferred to an electron, with the help of an non-radiative transition, resulting in the ejection of this electron. In case of a transition to a K shell of the atom the definition of the fluorescence yield is

$$\omega_K = \frac{I_K}{n_K} \tag{2.33}$$

where I_K is the total number of X-rays emitted from the sample and n_K the number of primary K shell vacancies. Auger probability p_{Auger} and fluorescence yield must equal to one, $\omega + p_{Auger} = 1$. The fluorescence yield increases with the atomic number Z and is highest for the K shell.

The **transition probability** $g_{i,j}$ is the probability that a vacancy in the shell i is filled by a transition from a certain shell j, with $\sum_j g_{i,j} = 1$. It is ruled by quantum mechanics and is mainly responsible for the emission line intensities. For K lines it varies only slightly with atomic number.

For the further considerations in this work it is useful to introduce the **effective linear mass attenuation coefficient** $\bar{\mu}_{lin}[1/\text{cm}]$ as the product of the effective mass absorption coefficient $\bar{\mu}_i$ and the density ρ of a sample:

$$\bar{\mu}_{lin,i} = \bar{\mu}_i \cdot \rho = \left(\sum_{elements\, j} \left(\frac{\mu_{0,j}}{\cos(\theta_A)} + \frac{\mu_{i,j}}{\cos(\theta_D)} \right) w_j \right) \rho \quad (2.34)$$

$$= \sum_{elements\, j} \left(\frac{\mu_{0,j}}{\cos(\theta_A)} + \frac{\mu_{i,j}}{\cos(\theta_D)} \right) \rho_j \quad (2.35)$$

which takes the geometry of the experiment into account, with θ_A and θ_D the angle between sample normal and excitation or detection axis, respectively. Absorption of the excitation radiation Φ_0 by an element j is described by $\mu_{0,j}$ and absorption of the fluorescence radiation of the element i by the element j by $\mu_{i,j}$. The local density ρ_i of the element i in the sample is the product of its weight percent value w_i and the density ρ of the sample:

$$\rho_i = \rho w_i \quad (2.36)$$

2.3.2 Fluorescence intensity

The relationship between elemental concentration and fluorescence intensities can be calculated using the Sherman equations [She55]. With the assumption that the excitation radiation is monochromatic, parallel and the sample with the thickness D is flat and homogeneous we can describe the primary intensity of a fluorescence line of the element i as follows:

$$\Phi_i = \Phi_0 K \epsilon \sigma_{F,i} \rho_i \int_0^D exp(-\bar{\mu}_{lin,i} x) dx \quad (2.37)$$

with ϵ the detection efficiency of the detector, Φ_0 the excitation intensity, ρ_i the mass density of the element i and K a calibration constant. This constant describes the influence of the geometric parameters of the setup and is as a first approximation not a function of energy. The integral contains the self-absorption of radiation in the sample.

For every fluorescence line i one equation in the form of 2.37 is obtained, resulting in a system of equations, which are coupled through the linear effective mass attenuation coefficient. This system must be solved in respect to the local density of the contained elements.

An inherent limitation of XRF is the range of detectable elements. This range is dependent on the experimental setup (synchrotron radiation, vacuum chamber, X-ray optics aso.), especially complicating the measurement of light elements. The elements which cannot be measured constitute the 'dark matrix', which might in some cases be close to 100 % of the sample.

2.3.3 Spectral evaluation

Figure 2.10 shows a typical fluorescence spectrum. In this case a glass reference material (Breitländer D3) has been investigated. Peak overlapping and detector artifacts can be distinguished.

In order to be able to use equation 2.37 for the determination of elemental composition the fluorescence intensity must be extracted from the spectrum. In XRF it is common to use the net areas of peaks as a measure for the fluorescence intensity. The spectral evaluation which leads to the net peak areas will be shown in the following with the help of the example of the spectrum in figure 2.10.

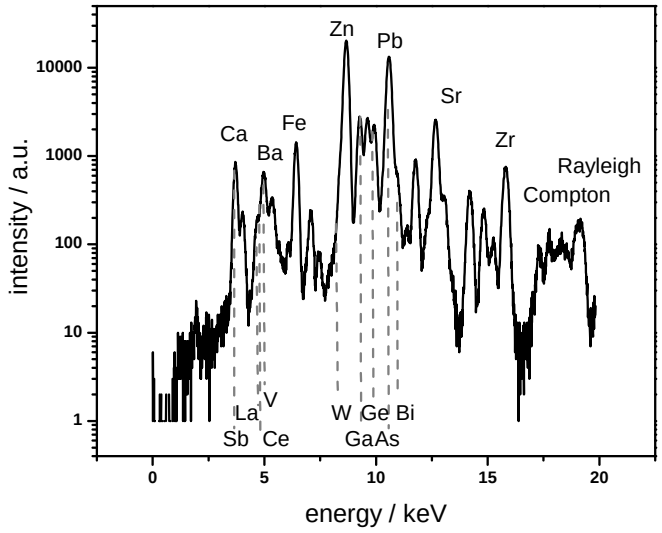

Figure 2.10: Fluorescence spectrum of the glass reference standard D3 (Breitländer)

In table 2.2 the visible elements of the sample are listed, with their certified weight percent values as well as their Kα and Lα fluorescence energies. A spectral deconvolution is mandatory for XRF spectra, especially when dealing with so many visible elements with evident peak-overlapping.

	K	Ca	V	Fe	Zn	Ga	Ge	As	Sr	Zr
$E_{K\alpha}$	3.313	3.69	4.95	6.4	8.64	9.25	9.89	10.54	14.16	15.77
$E_{L\alpha}$	-	-	-	0.85	1.01	1.10	1.19	1.28	1.81	2.04
weight-%	0.075	10.3	0.48	0.41	2.97	0.34	0.28	1.41	0.11	0.25
	Sb	La	Ce	W	Pb	Bi				
$E_{K\alpha}$	26.36	33.44	34.72	59.32	74.97	77.11				
$E_{L\alpha}$	3.6	4.65	4.84	8.40	10.55	10.84				
weight-%	1.54	0.75	0.72	0.25	1.58	0.16				

Table 2.2: Glass reference standard D3, weight percent values and fluorescence energies. The visible energies are marked in gray.

As a first step the measured spectra need to be calibrated according to the used detector. Two parameters are used for the conversion of detector channel to energy. Two more parameters, namely the electronic noise and the Fano factor, are used, in order to describe the energy-dependent width of the fluorescence peaks. A non-linear least square algorithm computes these values according to given fluorescence peaks. Two fluorescence lines at the far ends of the spectrum - f.e. Ca Kα and Zr Kα fluorescence peaks in figure 2.10 - are efficient for the calculation, decreasing the computation time considerably in comparison to a calibration with many elements.

As a next step the background is stripped, with an adjustable number of strip cycles and channels to use for the strip width w. Stripping is an iterative procedure. At each iteration, if the contents of channel i, $y(i)$, is above the average of the contents of the channels at w channels of distance, $y(i-w)$ and $y(i+w)$, $y(i)$ is replaced by the average. At the end of the process fast changing features in the spectrum, i.e. peaks, are 'stripped', while slowly changing features (background) have been approximated.

After defining a region of interest (ROI), all elements can then be fitted with the help of a linear least square algorithm. Line intensity rations derived from the Elam database are used in order to deconvolute overlapping peaks and pile-up and escape corrections are calculated for each element.

In this work a special emphasis is laid on the scattering of radiation. The fitting of the scattered peak net areas is not commonly discussed in literature. While the Rayleigh peak can be treated with a Gaussian function equal to those used for the fluorescence peaks, the Compton peak is broadened, see section 2.1.2. Additionally, peak overlapping is possible in the Compton peak energy range, which complicates the analysis further.

In [GLE03] the authors propose a model for the description of the Compton peak based on Monte Carlo simulations. Due to the complexity of the proposed model a different procedure was used in this work. Figure 2.11 shows as an example of the scattered radiation energy range of the spectrum in figure 2.10. Two peaks are overlapped with the Compton peak. The Rayleigh peak (green line) is subtracted from the measured data (black line). In the area of the line overlap, the strip background is used instead of the measured data. Then the sum of the intensity of the red line in figure 2.11 amounts to the Compton net peak area.

2.4 Micro-XRF and 3D Micro-XRF

Micro-analysis has been performed with X-ray optics at synchrotron since the 1960's. The advent of polycapillary optics, described in section 2.2.3, in recent years has made micro-analysis feasible for the use with X-ray tubes, also. Micro X-ray fluorescence spectroscopy (Micro-XRF) makes lateral micro imaging possible [KVJ00], [DJS$^+$08] due to lateral focusing of the excitation radiation to spot sizes of less than 100 μm. Depth resolution can additionally be achieved, when utilizing a second polycapillary lens in the detection channel.

The next two sections introduce these two techniques with a special emphasis on 3D Micro-XRF. In both sections the experimental setups used in this work and some

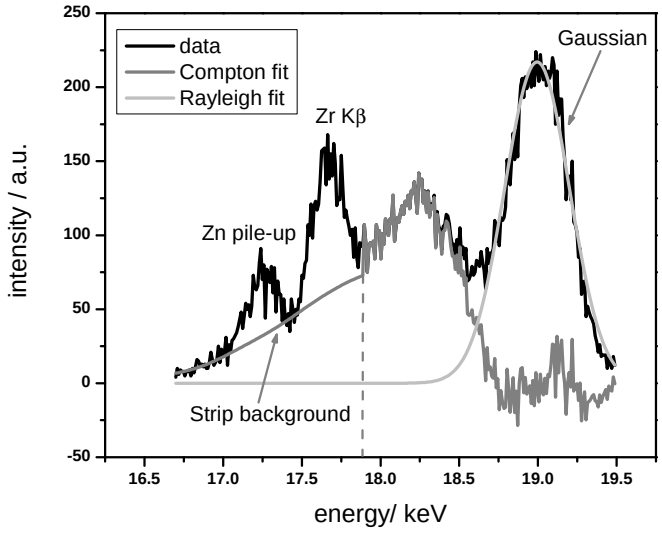

Figure 2.11: Fitting of the scatter peaks with line overlap.

theoretical considerations are presented.

2.4.1 Micro-XRF

The principle of Micro-XRF is the use of one X-ray optic for the formation of a micro-spot on the surface of a sample. The radiation from a tube is focused by a polycapillary full lens onto such a spot. The fluorescence from the sample is collected with an energy-dispersive detector. The small spot size ensures lateral resolution, thus making surface maps possible. Depth resolution however is not easily accomplished. Detected radiation originates as a general rule from different depths in the sample, thus complicating quantification for layered structures.

Similar to equation 2.37 a system of equations can be established for the evaluation of the relationship between fluorescence intensity and elemental concentration. The problem of non-parallel radiation can be neglected [MK03], but the polychromatic excitation $\Phi_0(E)$ and the energy-dependent transmission $T(E)$ of the polycapillary full lens complicate the analytical context:

$$\begin{aligned} \Phi_i &= K\rho_i \int_{E_{edge}}^{E_{max}} \Phi_0(E)T(E)\sigma_{F,i}(E) \int_0^D exp(-\bar{\mu}_{lin,i}(E)\, x)dxdE \qquad (2.38) \\ &= Kw_i \int_{E_{edge}}^{E_{max}} \Phi_0(E)T(E)\frac{\sigma_{F,i}(E)}{\bar{\mu}_i(E)} \left(1 - \exp(-\bar{\mu}_i(E)Q)\right) dE \end{aligned}$$

with Q[mass/area] and w_i the weight percent of the element i. The excitation spec-

trum must be multiplied with the transmission function of the used lens. While all the other components of equation 2.38 can be calculated or measured, the actual transmission function is difficult to determine absolutely, see section 2.2.3. In this work the quantification of the Micro-XRF data has been done with the help of a newly developed calibration procedure [Wol09].

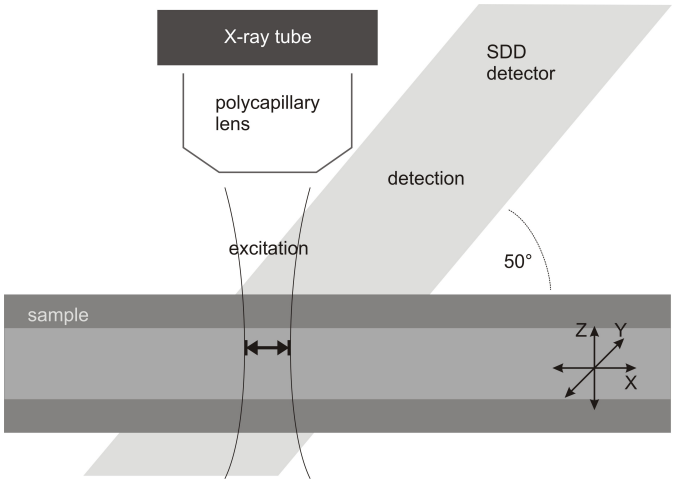

Figure 2.12: Micro-XRF sketch: the geometry refers to the used MicroTax spectrometer.

In this work X-ray tube Micro-XRF measurements have been used which were performed by Timo Wolff of the BAM for the validation and support of the 3D Micro-XRF analysis. For the measurements a commercially available spectrometer was utilized [BRB+01] with a 30 W Molybdenum tube, see figure 2.12. A polycapillary full lens in the excitation channel focuses the radiation onto a spot of about 70 µm on the sample. Fluorescence radiation is collected by a SDD with an energy resolution of 170 eV (Mn Kα) at 50 kcps. The head of the spectrometer can be flushed with Helium in order to enhance the sensitivity for lighter elements. The system has a camera for sample positioning and can be transported on site.

2.4.2 3D Micro-XRF

The use of two polycapillary lenses in a confocal geometry makes three-dimensional analysis possible. Figure 2.13 shows the schematic diagram of a 3D Micro-XRF setup.

Radiation from an X-ray tube or synchrotron radiation is focused by a polycapillary full or halflens onto a sample. The resulting characteristic fluorescence radiation is transported with a second polycapillary halflens to an energy-dispersive detector. The overlap of the foci of the two optics forms a probing volume from which information is derived. Due to the finite size of this probing volume information can be obtained three-dimensionally by moving the micro-volume through the sample. Absorption of exciting and fluorescence radiation limits the possible information depth and the extension of the probing volume affects the shape of the profiles.

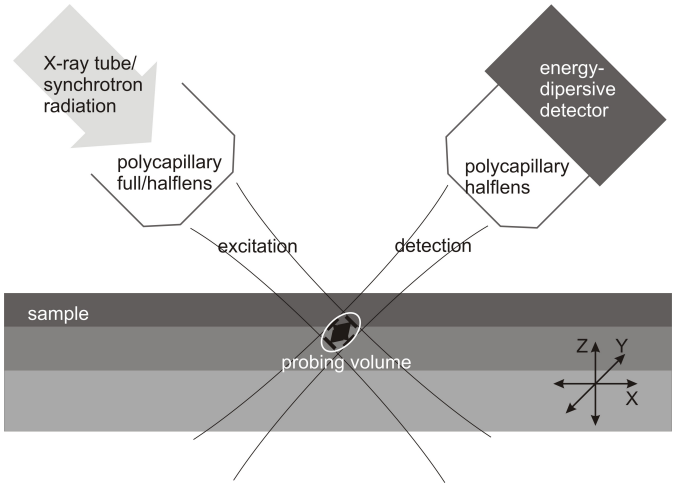

Figure 2.13: 3D Micro-XRF sketch; two polycapillary helflenses ensure three-dimensional resolution.

While 3D Micro-XRF can be used to obtain full 2D or 3D maps [KMP+07], the collection of depth profiles has proved to be a suitable measurement strategy for a number of analytical questions, see chapter 5. Depth profiles are the net peak intensities of fluorescence peaks as a function of depth. In practice that means, that a sample is moved through the probing volume in the z-direction of figure 2.13. After a movement of 5 to 10 µm a spectrum is collected. After a number n of steps, n spectra as a function of the position in relation to the sample surface are obtained. As an example of depth profiling the measurement of the glass reference standard of section 2.3.3 is shown in the left panel of figure 2.14. Each spectrum has to be analyzed individually in order to obtain the net peak intensities of the fluorescence and the scattered peaks. By plotting these net peak areas as a function of position, depth profiles for each fluorescence elements are produced. The right panel of figure 2.14 shows the depth profiles of a few pronounced peaks and the scatter peaks of the spectra. The goal of quantitative 3D Micro-XRF as presented in this work is the analysis of these depth profiles and the subsequent reconstruction of elemental composition of the investigated sample.

Sychrotron setup

In the course of this work 3D Micro-XRF with synchrotron radiation was performed at the Berlin synchrotron BESSY. In the beginning of this work a setup at the BAMline could be used. For later measurements the new mySpot beamline which was especially developed for micro-analysis measurements was available. Both beamlines have the same wavelength shifter as source, see section 2.2.1.

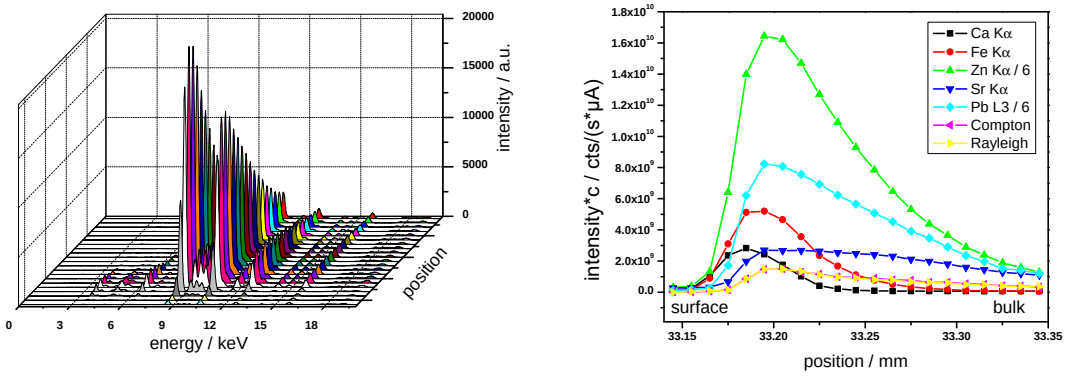

Figure 2.14: left: While moving the sample into the probing volume with step widths of 5 µm, at each position a spectrum is collected. right: Depth profiles of the main elements and the scattered peaks of reference sample D3.

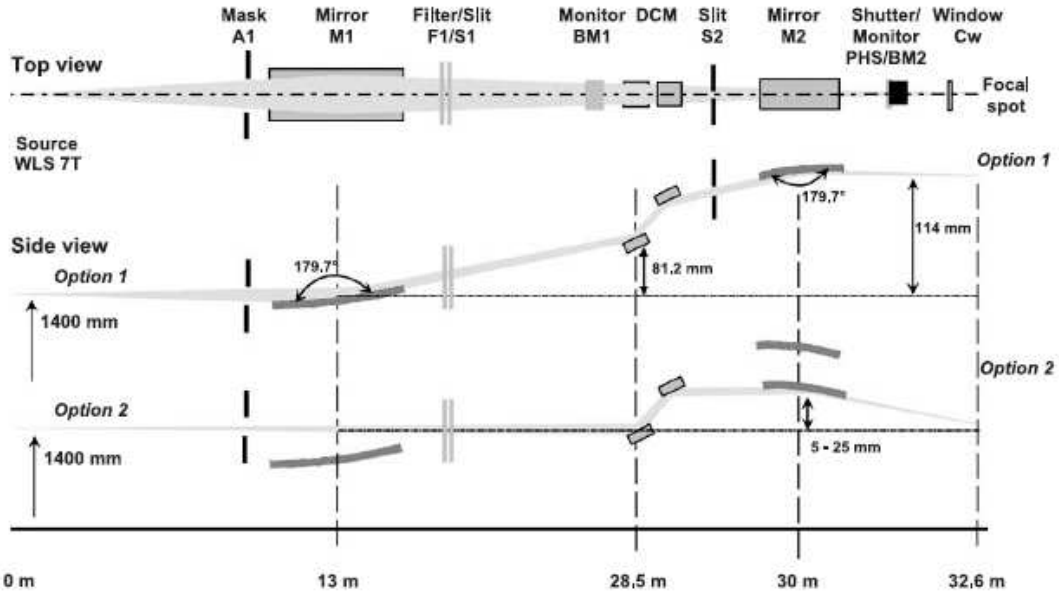

Figure 2.15: Optical layout of the mySpot beamline [ESF+04]

As an example for a beamline setup, the optical layout of the mySpot beamline is depicted in figure 2.15. The radiation from the wavelength shifter is collimated by the toroidal mirror, M1 (cylinder with bender) vertically. Either a double crystal (DCM) or a double multilayer (DMM) monochromator is located at a distance of 28.5 m from the source. The monochromatic beam is vertically focused by the bimorph mirror M2. At the focus of the beamline the beam has a spot size of 300 µm [ESF+04], exit flux on 10^{11} ph/s (DCM) to 10^{13} ph/s (DMM) with energy resolution of 1 - 3 eV (DCM).

At the **BAMline** the 3D Micro-XRF setup was realized with two polycapillary halflenses and a Si(Li) detector. The detector was positioned in a 90° angle to the excitation axis in the ring plane. The angle between sample normal and excitation axis was 45°. The first lens was aligned using a three translation axes and two rotation axes, while the second lens was mounted on the detector snout. The sample could be moved in three dimensions with step motors with a precision of $< 1\mu m$. The position of the probing volume on the sample was optically controlled along the focal distance by an optical long focal distance microscope with a resolution of about 3 µm. The flux of the monochromatic radiation falling onto the first X-ray optic was measured by an ionization chamber. The typical excitation energy was 19 keV and for depth profiling the sample was moved in the direction of the sample normal (z-axis in figure 2.13).

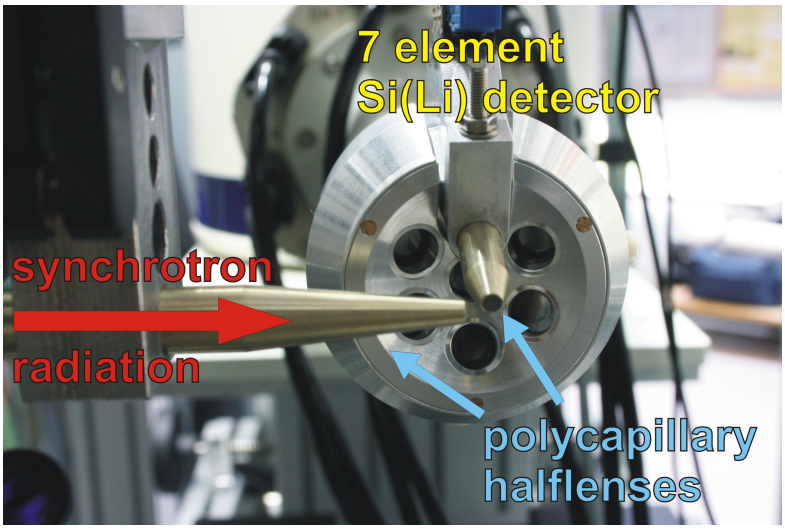

Figure 2.16: 3D Micro-XRF setup at the mySpot beamline: The detection lens is mounted in front of the north element of a 7 element Si(Li) detector.

The major improvement of the setup at the **mySpot beamline** is the presence of a 7 element Si(Li) detector, see figure 2.16, which makes simultaneous Micro-XRF and 3D Micro-XRF measurements possible. Only in front of one of the seven detection elements a polycapillary halflens is mounted, so that up to four other channels can be used for angle-dependent Micro-XRF. In order to be able to use scattered radiation for analysis the north element of the detector was chosen for the 3D setup.

Laboratory setup

In the course of this work two laboratory setups were used, a flexible configuration and a compact spectrometer. The main experimental difference to 3D Micro-XRF setups at a synchrotron is, that a polycapillary full lens must be used in the excitation channel due to the fact, that radiation from a spot source is focused onto a spot on the sample.

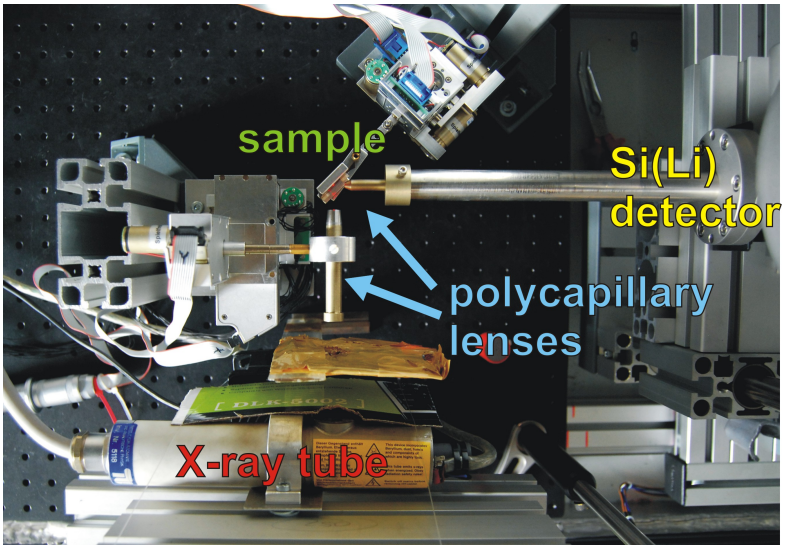

Figure 2.17: Top view of the flexible 3D Micro-XRF setup at the laboratory of the TU Berlin, a Mo X-ray tube, two polycapillary optics and a Si(Li) detector are used.

The **flexible setup** is realized with a 30 W Mo X-ray tube with an anode spot of about 100 µm, see figure 2.17. In the excitation channel a polycapillary minilens with a spot size of 65 µm at 16 - 19 keV is used. As detection optic different polycapillary halflenses can be used, with spot sizes of about 30 µm at 5 - 10 keV and different gain factors. While the first lens can be moved with a goniometer in three translation directions and two rotation axes, the second lens is directly mounted on the snout of a Si(Li) detector. The detector can be moved manually in three directions. A SDD or a pin diode are available for the monitoring of the alignment. Two lasers ensure a correct positioning of the sample, which can be moved in three directions with a motor precision of less than 0.5 µm. The setup is situated inside a 2140 mm x 740 mm x 1100 mm Pb-coated box with interlock doors in order to ensure flexibility and safety.

The specialty of the **compact spectrometer** is the measuring head, where both polycapillary lenses (spot sizes of about 20 µm at 20 keV) are firmly inserted to prevent misalignment, see figure 2.18. A 30 W Mo X-ray tube with an anode spot of about 50 µm and a SDD with a resolution of <145 eV at 150 kps at Mn Kα are also attached to the head. A microscope with camera allows the monitoring of the sample surface and position.

The compact spectrometer is more sensitive and has a better depth resolution. The

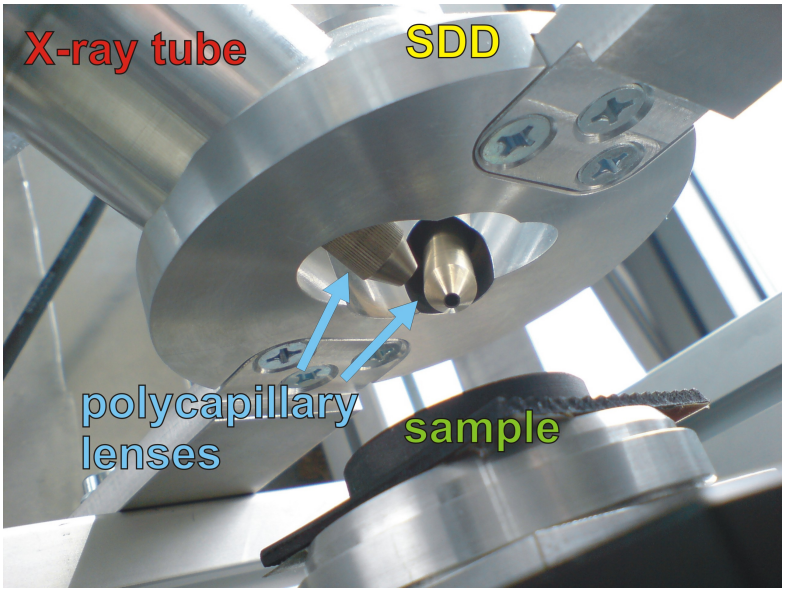

Figure 2.18: Compact 3D Micro-XRF spectrometer at the laboratory of the TU Berlin, a Mo X-ray tube, two polycapillary optics and a SDD are used.

flexible setup, though, can be used, when experimenting with different geometries, optics or X-ray tubes.

3 Theory of 3D Micro X-ray Fluorescence Analysis

In chapter 2.4.2 the principle of 3D Micro-XRF has been introduced. To understand the theory of this method a closer look must be taken at the X-ray optics and the overlap of their foci which forms the probing volume. The shape and sensitivity of this probing volume will be discussed in detail in the first section.

The second section deals with the quantification theory for homogeneous samples. Characteristic energy effects of 3D Micro-XRF are discussed with the help of a simulation example. A calibration procedure is introduced. The third section introduces the quantification scheme for stratified samples.

While the first three sections deal with monochromatic excitation, the fourth section gives insights into the difficulties of polychromatic excitation and explains first ideas for a quantification strategy.

3.1 Sensitivity

The intensity distribution of transported radiation in the focal plane of a polycapillary halflens can be described by a Gaussian distribution, see chapter 2.2.3. The width of the Gaussian distribution in the focal area does not change significantly within a length of about 200 µm. Therefore two-dimensional Gaussian functions can be used as a first approximation in the area of the overlap for the description in 3D Micro-XRF. Two such two-dimensional Gaussian distributions form the probing volume. The shape and sensitivity of this probing volume is determined by the properties of the two lenses - FWHM and transmission - as well as the geometry of the setup.

Let y_A be the excitation axis and y_D the detection axis. Then we can use following two expressions for the intensity distributions of excitation and detection lens:

$$\eta_A = \frac{T_A}{2\pi\sigma_A^2} \exp(-\frac{x_A^2 + z_A^2}{2\sigma_A^2}) \tag{3.1}$$

with z_A the vertical axis, T_A the global transmission and σ_A the spot size of the excitation lens and

$$\eta_D = \frac{\Omega T_D}{4\pi} \exp(-\frac{x_D^2 + z_D^2}{2\sigma_D^2}) \tag{3.2}$$

with z_D the vertical axis, Ω the solid angle of acceptance, T_D the transmission and σ_D the spot size of the detection lens.

The difference of the first factor in 3.1 and 3.2 can be explained by the different angle of acceptance. In case of the excitation lens parallel radiation is transported onto an energy-dependent focal spot. The detection lens on the other hand collects radiation from an isotropic radiation source, which is ideally a point source. This difference leads to the fact that the units of $\eta_A[1/\mathrm{cm}^2]$ and $\eta_D[1]$ are different, see [Mal04].

The overlap of the two foci is mathematically described by the product of η_A and η_D. Depending on the relation of the two coordinate systems (excitation and detection system) to each other, different cases can be distinguished, which will be discussed in the following sections.

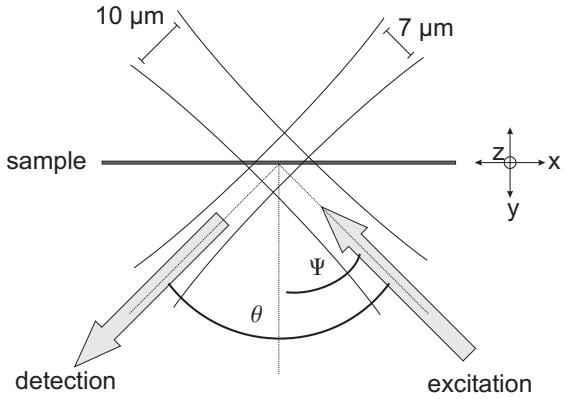

Figure 3.1: Optimal setup configuration with an angle of $\theta = 90°$ between excitation and detection axis and an angle $\Psi = 45°$ between excitation axis and sample surface.

3.1.1 Optimal case

The optimal case is, when excitation and detection axis are perpendicular toward each other, see figure 3.1, and there is no vertical displacement, i.e. $z_A = z_D = z$. Then the product of both intensity distributions can easily be calculated:

$$\begin{aligned} \hat{\eta}(x,y,z) &= \eta_A \eta_D \epsilon \\ &= \frac{\Omega T_A T_D \epsilon}{8\pi^2 \sigma_A^2} \exp\left(-\frac{\sigma_D^2 x_A^2 + \sigma_A^2 x_D^2 + (\sigma_D^2 + \sigma_A^2) z^2}{2\sigma_A^2 \sigma_D^2}\right) \end{aligned} \tag{3.3}$$

The 3D sensitivity $\hat{\eta}$ is the product of both intensity distributions multiplied with the detector efficiency ϵ. It determines the sensitivity of the setup for the detection of specific fluorescence lines. The shape of the 3D sensitivity is that of a three dimensional ellipsoid, where the FWHM in the different axes are determined by the FWHM of the optics.

In order to describe the interaction of this sensitivity with a sample as depicted in figure 3.1 a common coordinate system must be used. The coordinate system of the

sample is a reasonable choice when dealing with stratified samples, as the sample can then be moved along the axes of the system. The sample is positioned in the x-z-plane at $y = 0$, with Ψ the angle between excitation beam axis and sample normal. Following coordinate transformation can be used:

$$\begin{aligned} x_A &= x\sin(\Psi) + y\cos(\Psi) && (3.4)\\ x_D &= x\cos(\Psi) - y\sin\Psi && (3.5)\\ z_A &= z_D = z \end{aligned}$$

As it describes the rotation around the z-axis, the Jacobian is equal to one. This leads to:

$$\begin{aligned} \hat{\eta}(x,y,z) &= \frac{\Omega T_A T_D \epsilon}{8\pi^2\sigma_A^2} && (3.6)\\ &\exp\left(-\frac{(\sigma_A^2(x\cos(\Psi) - y\sin\Psi)^2 + \sigma_D^2(x\sin(\Psi) + y\cos(\Psi))^2 + (\sigma_D^2+\sigma_A^2)z^2)}{2\sigma_A^2\sigma_D^2}\right) \end{aligned}$$

The integration over the sample surface leads then to a new term, the **sensitivity function** $\tilde{\eta}$, which is only dependent on the position of the probing volume in respect to the sample surface:

$$\begin{aligned} \tilde{\eta}(y) &= \int_{-\infty}^{\infty}\int_{-\infty}^{\infty}\hat{\eta}(x,y,z)dxdz && (3.7)\\ &= \frac{\Omega T_A T_D \epsilon}{4\pi}\frac{\sigma_D^2}{\sqrt{(\sigma_D^2+\sigma_A^2)(\cos^2(\Psi)\sigma_A^2 + \sin^2(\Psi)\sigma_D^2)}}\exp\left(-\frac{1}{2}\frac{y^2}{(\sin^2(\Psi)\sigma_D^2 + \cos^2(\Psi)\sigma_A^2)}\right)\\ &= \frac{\eta}{\sqrt{2\pi}\sigma_y}\exp\left(-\frac{y^2}{2\sigma_y^2}\right) && (3.8) \end{aligned}$$

with the width of the probing volume σ_y

$$\sigma_y = \sqrt{\sigma_D^2\sin^2(\Psi) + \sigma_A^2\cos^2(\Psi)} \tag{3.9}$$

and the integral sensitivity η

$$\eta = \frac{\Omega T_A T_D \epsilon}{\sqrt{8\pi}}\frac{\sigma_D^2}{\sqrt{\sigma_A^2+\sigma_D^2}} \tag{3.10}$$

This sensitivity function substitutes the calibration constant in XRF analysis. It is a function of the place of measurement as with the overlap of the foci a volume is formed which can be moved three-dimensionally. The sensitivity function is a Gaussian distribution with two new parameters, the width of the probing volume σ_y and the integral sensitivity η. These two parameters characterize the probing volume and, thus,

with the knowledge of the excitation radiation (intensity I_0 and energy E_0) the setup completely.

The width σ_y describes the size of the probing volume in the direction normal to the sample. With

$$\frac{d\sigma_y}{d\sigma_A} = \frac{\sigma_A \cos 2(\Psi)}{\sqrt{\sigma_D^2 \sin^2(\Psi) + \sigma_A^2 \cos^2(\Psi)}} \geq 0 \tag{3.11}$$

$$\frac{d\sigma_y}{d\sigma_D} = \frac{\sigma_D \sin^2(\Psi)}{\sqrt{\sigma_D^2 \sin^2(\Psi) + \sigma_A^2 \cos^2(\Psi)}} \geq 0 \tag{3.12}$$

it is clear, that σ_y is a monotonically increasing function of both arguments. That means, that due to the decrease of spot size of a polycapillary lens with increasing transported energy, the width of the probing volume decreases for higher excitation energies as well as for higher fluorescence energies, also.

The integral sensitivity η is defined as

$$\eta = \int_{-\infty}^{\infty} \tilde{\eta}(x) dx \tag{3.13}$$

and determines the maximal sensitivity of the setup for a certain fluorescence energy. This parameter is not only affected by the energy-dependence of the spot sizes of the two optics, but also it is dependent on both transmission functions. Both parameters will be discussed in section 3.2.3.

For clarification purposes some calculations will be presented here and in the following sections. According to the optics used at the mySpot beamline following values were used: $\sigma_A = 10$ µm and $\sigma_D = 7$ µm; $\Omega\epsilon = 1$ and $T_A = T_D = 0.2$, with 20 % as a mean transmission. With these values we derive for the optimal alignment $\sigma_y = 8.63$ µm and $\eta = 3.2 \cdot 10^{-2}$µm.

3.1.2 Displacement

This section describes the problem of a non-optimal alignment. Especially of interest is the question whether the sensitivity function can always be described by a Gaussian distribution. As the excitation and detection tube are rotation-symmetric only a limited number of cases can occur which deviate from the optimal case.

With the assumption, that σ_A and σ_D do not change significantly in the focal width area, a small misalignment of the second lens up or down the excitation axis or up or down the detection axis will not affect the probing volume. A big misalignment in the case of our example must be a displacements of more than 200 µm. This is not likely for a fully automated setup with translation step widths of a few µm. A misplacement of the second lens in the z-direction, see figure 3.1, as well as a change in the 90°-geometry will be discussed in the following paragraphs.

Vertical displacement

If the foci of the two optics do not ideally overlap and there is a vertical displacement, equation 3.3 must be written as:

$$\begin{aligned}\hat{\eta}(x,y,z) &= \eta_A \eta_D \epsilon \\ &= \frac{\Omega T_A T_D \epsilon}{8\pi^2 \sigma_A^2} \exp(-\frac{\sigma_D^2 x_A^2 + \sigma_A^2 x_D^2 + \sigma_A^2 z^2 + \sigma_D^2 (z+k)^2}{2\sigma_A^2 \sigma_D^2}) \end{aligned} \tag{3.14}$$

with k the vertical displacement. The vertical displacement has been introduced into the formalisms describing the first lens, which is equivalent to the negative displacement of the second lens, thus, with no restriction for k, all possible cases of vertical misalignment are covered. Integration of equation 3.14 leads then to

$$\tilde{\eta}(y) = \frac{\eta_v}{\sqrt{2\pi}\sigma_y} \exp\left(-\frac{y^2}{2\sigma_y^2}\right) \tag{3.15}$$

with

$$\eta_v = \eta \cdot \exp\left(-\frac{1}{4}\frac{k^2(\sigma_A^2 + \sigma_D^2 + \cos(2\Psi)\cdot(\sigma_A^2 - \sigma_D^2))}{(\sin^2(\Psi)\sigma_D^2 + \cos^2(\Psi)\sigma_A^2)(\sigma_A^2 + \sigma_D^2)}\right) \tag{3.16}$$

Note, that the difference between 3.7 and 3.15 is the term for the integrated sensitivity, which must be modified depending on the misalignment, i.e. as a function of k. As will be discussed in section 3.2.3 the integrated sensitivity is a parameter which will be measured with the help of a calibration and therefore a vertical displacement changes only the measured intensity without introducing errors in our theoretical considerations.

The modification factor is a Gaussian function in k. Its values lie between 0 and 1. For small k the displacement is negligible. With the used values of the polycapillary lenses its sigma is 12.2 µm, which means, that if the displacement is in the order of magnitude of σ_A and σ_D, the absolute value for the sensitivity function decreases to $1/e$ of the value without displacement. In the calculation example, with a misalignment of $k = 10$ µm, the new values for the characteristic parameters are $\sigma_y = 8.63$ µm and $\eta = 2.3 \cdot 10^{-2}$µm.

Angular displacement

If the angle θ between excitation and detection axis is not equal to 90°, the shape of the probing volume changes. Equation 3.3 must be modified according to a rotation around the z-axis:

$$\begin{aligned}\hat{\eta}(x,y,z) &= \frac{\Omega T_A T_D \epsilon}{8\pi^2 \sigma_A^2} \\ &\quad \exp\left(-\frac{\sigma_D^2 x_A^2 + \sigma_A^2 (x_D \cos\theta - y_D \sin\theta)^2 + (\sigma_A^2 + \sigma_D^2) z^2}{2\sigma_A^2 \sigma_D^2}\right)\end{aligned} \tag{3.17}$$

In this case the excitation axis has been rotated in respect to the sample. Similar to the argumentation for the vertical displacement, without restriction for θ all possible cases

are covered with equation 3.17. Integration over the sample surface leads then to

$$\tilde{\eta}(y) \quad = \quad \frac{\eta_a}{\sqrt{2\pi}\sigma_{y,a}} \exp\left(-\frac{y^2}{2\sigma_{y,a}^2}\right) \tag{3.18}$$

were both characteristic parameters are modified compared to the optimal case. The integral sensitivity can be written as

$$\eta_a \quad = \quad \eta \sin\theta \tag{3.19}$$

and the width of the probing volume is

$$\sigma_{y,a} \quad = \quad \frac{1}{\sin(\theta)} \sqrt{\sin^2(\Psi+\theta)\sigma_A^2 + \sin^2(\Psi)\sigma_D^2}$$

The angle θ between excitation and detection axis changes the shape of the probing volume and the intensity of the sensitivity. Nevertheless, the shape of the sensitivity function remains a Gaussian function. Both modified parameters are equivalent to η and σ_y for $\theta = 90°$.

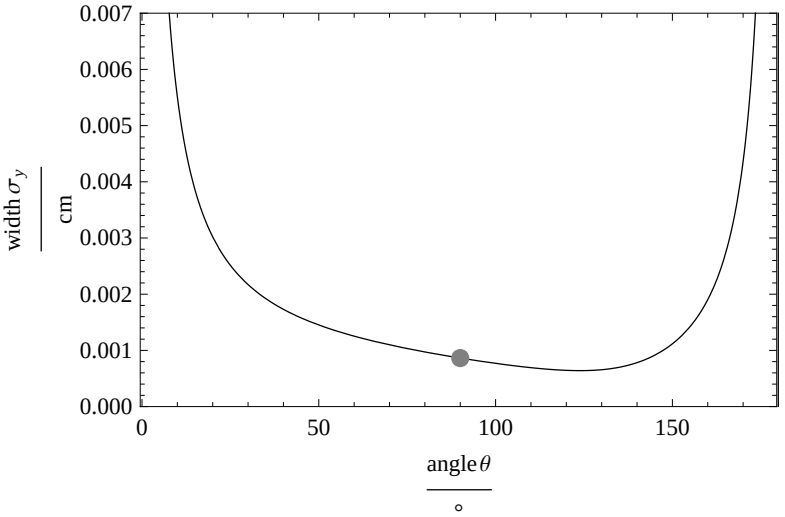

Figure 3.2: The width of the probing volume $\sigma_{y,a}$ as a function of the angle between excitation and detection axis.

In figure 3.2 the angle-dependency of the width of the probing volume for the values $\sigma_A = 10$ µm and $\sigma_D = 7$ µm is plotted. The function has singularities for $\theta = 0°$ and $\theta = 180°$, when excitation and detection axis are parallel. In the range between those two extremes, the function slowly decreases with increasing angle, due to the sigma values used for the calculation. The minimal width of the probing volume is for the plotted example at about $\theta = 130°$. The inherent decrease of integral sensitivity ($\eta_a(130°) = 2.45 \cdot 10^{-2}$µm) prevents the use of this geometry for optimal excitation.

Similar to equations 3.11 and 3.12 it can be shown that $d\sigma_{y,a}/d\sigma_{A/D} \geq 0$. The width of the probing volume decreases with increasing transported energy. For $\Delta\theta = 10°$ ($\theta = 80°$ and $\theta = 100°$) the characteristic parameters are $\Delta\sigma_y < 13\%$ ($\sigma_y = 9.72$ µm and $\sigma_y = 7.63$ µm) and $\eta_a = 3.15 \cdot 10^{-2}$µm.

3.1.3 MySpot setup

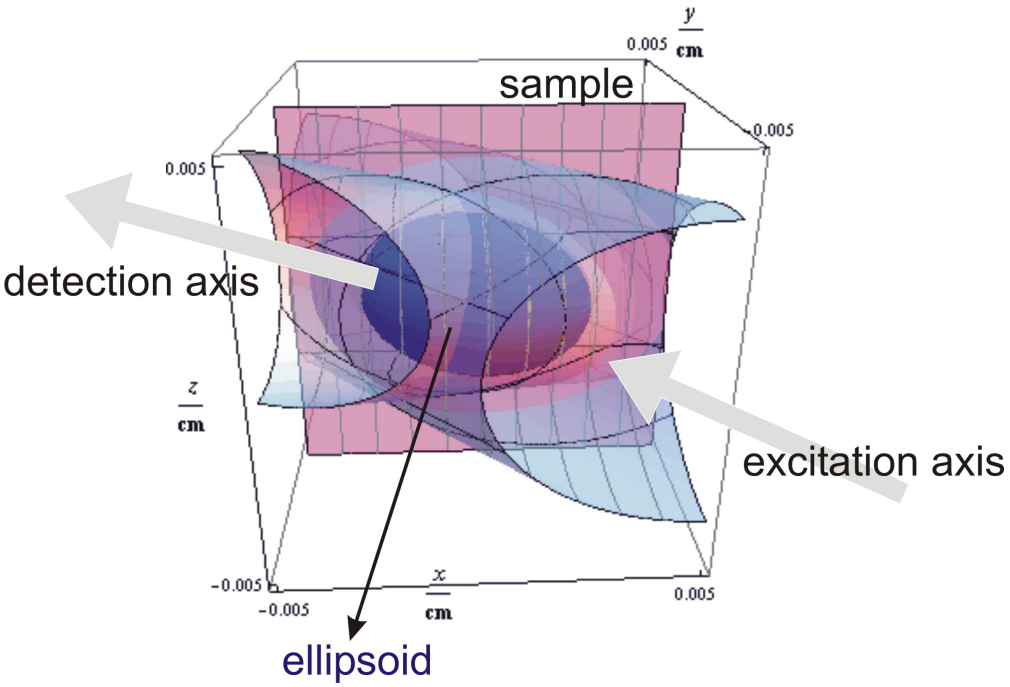

Figure 3.3: Configuration at the mySpot beamline at BESSY II. The angle between ring plane and detection axis is 20° due to the use of the north element of the 7-element Si(Li) detector, see section 2.4.2.

At the mySpot beamline a 7-element detector is used, see section 2.4.2. The detection lens is mounted in front of the north detector element, which means, that there is a 20° angle between ring plane and detection axis, see figure 3.3. This leads to the following changes:

$$z_D = z_A \cos(-20°) - x_A \sin(-20°) \tag{3.20}$$

$$\begin{aligned} \hat{\eta}(x,y,z) &= \frac{\Omega T_A T_D \epsilon}{8\pi^2 \sigma_A^2} \\ &\exp\left(-\frac{\sigma_D^2 x_A^2 + \sigma_A^2 x_D^2 + \sigma_A^2 (z\cos(-20°) - x_A \sin(-20°))^2 + \sigma_D^2 z^2}{2\sigma_A^2 \sigma_D^2}\right) \end{aligned} \tag{3.21}$$

The ellipsoid is rotated around the excitation axis, therefore we obtain a mixed $x_A \cdot z$-term. Integration leads to

$$\tilde{\eta}(y) = \frac{\eta}{\sqrt{2\pi}\sigma_{y,m}} \exp\left(-\frac{y^2}{2\sigma_{y,m}^2}\right) \tag{3.22}$$

with

$$\sigma_{y,m} = \sqrt{\frac{\sin^2(\Psi)\sigma_D^4 + \sigma_A^2\sigma_D^2 + \cos^2(20°)\cos^2(\Psi)\sigma_A^4}{(\sigma_A^2 + \sigma_D^2)}} \tag{3.23}$$

Again, the sensitivity function can be described by a Gaussian distribution. While the integral sensitivity is not affected by the 20° angle, the width of the probing volume is reduced to $\sigma_{y,m} = 8.4$ µm, see table 3.1. The difference to the optimal case can be seen in figure 3.4 for seven different values of σ_D. The difference is maximal for $\sigma_D = 7$ µm, but for all σ_D negligible as not significant.

The derivative of equation 3.23 in respect to $\sigma_{A/D}$ is always positive, thus, the width of the probing volume decreases with increasing fluorescence energy.

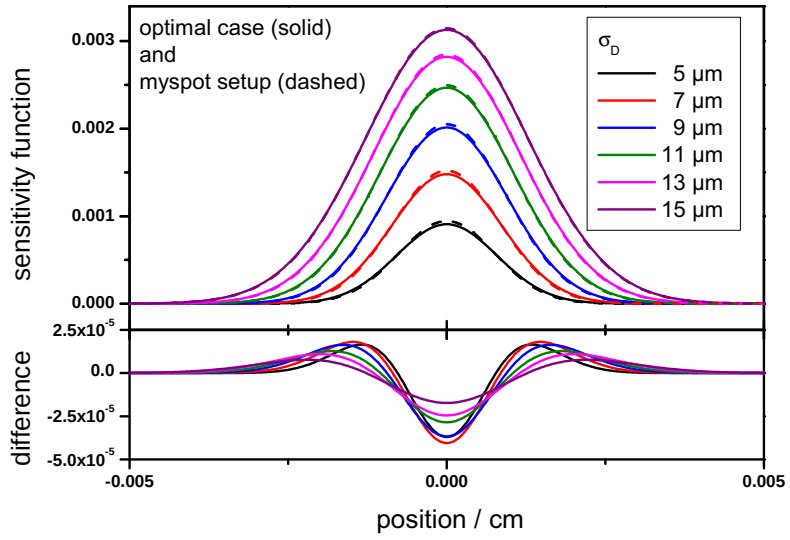

Figure 3.4: Difference of sensitivity function between the optimal case and the mySpot setup, where the angle between ring plane and detector axis is 20°, for seven different values of σ_D.

Because the ellipsoid is tilted inside the sample a misalignment may possibly change the shape of the depth profile. A vertical displacement $z_A \rightarrow z + k$ alters the sensitivity

function as follows:

$$\tilde{\eta}(y) = \frac{\eta}{\sqrt{2\pi}\sigma_{y,m}} \exp\left(-\frac{y^2}{2\sigma_{y,m}^2}\right) \exp(-gy) \exp(-h) \tag{3.24}$$

with

$$g = \left(\frac{k\,\sigma_A^2(\sin(40^\circ - \Psi) + \sin(40^\circ + \Psi))}{4(\sin^2(\Psi)\sigma_D^4 + \sigma_A^2\sigma_D^2 + \cos^2(20^\circ)\cos^2(\Psi)\sigma_A^4)}\right) \tag{3.25}$$

and

$$h = \left(\frac{k^2\cos^2(20^\circ)(\cos^2(\Psi)\sigma_A^2 + \sin^2(\Psi)\sigma_D^2)}{2(\sin^2(\Psi)\sigma_D^4 + \sigma_A^2\sigma_D^2 + \cos^2(20^\circ)\cos^2(\Psi)\sigma_A^4)}\right) \tag{3.26}$$

The Gaussian intensity distribution with $\sigma_{y,m} = 8.4$ µm and $\eta = 3.2 \cdot 10^{-4}$µm is distorted with a linear exponential term and a constant term. In figure 3.5 the undisturbed sensitivity function of equation 3.22 is displayed as well as the functions $\exp(-g * y) \cdot \exp(-h)$ for $k = 5$ µm, $k = 10$ µm, $k = 15$ µm and $k = 20$ µm. The precision and reproducibility of the step motors in the vertical direction is about ± 2 µm at the synchrotron setup. A misalignment of a few microns does not affect the shape of the Gaussian considerably. For bigger misalignments the intensity decreases significantly. A displacement of 15 µm yields a decrease to half of the expected intensity. In practice it is unlikely, that the loss in intensity will not be observed.

Thus, the change in shape due to the exponential term in y is negligible compared to the loss in intensity. The sensitivity function can be described for small k by a Gaussian distribution.

case	σ_y/µm	η/µm
optimal	8.63	$3.2 \cdot 10^{-2}$
vertical displacement $k = 10$ µm	8.63	$2.3 \cdot 10^{-2}$
angular displacement $\Delta\theta = 10^\circ$	7.63 – 9.72 µm	$3.15 \cdot 10^{-2}$
mySpot	8.40	$3.2 \cdot 10^{-2}$

Table 3.1: Width of probing volume and integral sensitivity in various cases

In consequence of the latter sections we can deduce that as a first approximation the sensitivity function can always be described by a Gaussian intensity distribution with two characteristic parameters η and σ_y. The calculated values for the width of the probing volume σ_y and the integral sensitivity η for the presented scenarios are listed for comparison in table 3.1. The two parameters are functions of the transmission properties of the used polycapillary lenses, namely their FWHM and transmission functions. Additionally they are highly sensitive to the geometry of the setup. Especially the integral sensitivity, which determines the intensity of the fluorescence information, is sensitive to misalignment. The width of the probing volume is a monotonically decreasing function in respect to the transported radiation energy.

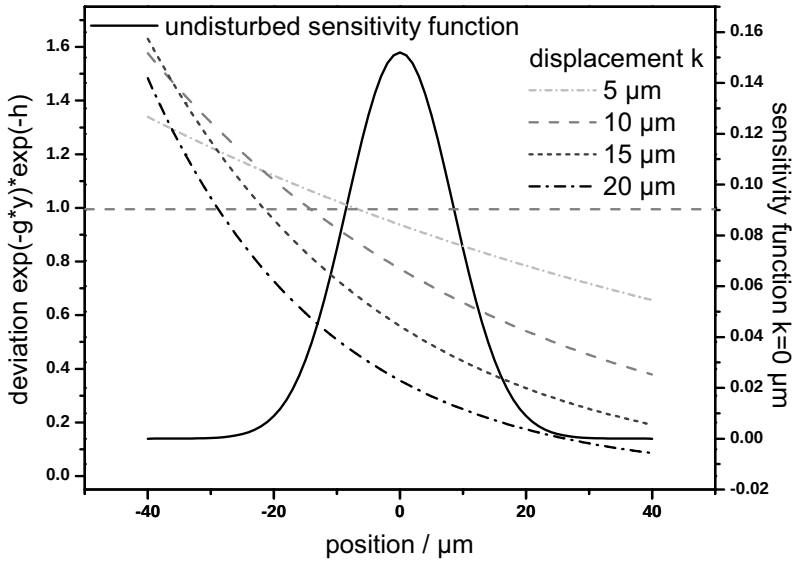

Figure 3.5: Difference of sensitivity function between the mySpot setup and a vertical displacement of 5 µm, 10 µm, 15 µm and 20 µm.

3.2 Fluorescence equation for homogeneous samples

In chapter 2.3.2 equation 2.37 on page 22 was introduced to describe the intensity of a fluorescence line of an element i of a thick, homogeneous sample with the thickness $D = d_2 - d_1$ in XRF analysis. This equation must now be modified according to the considerations of the last section. The calibration constant has to be replaced with the sensitivity function. As the integral sensitivity and the width of the probing volume are functions of transported energy they will in the following be denoted with the index i for the considered fluorescence energy of an element i.

By substituting the calibration constant K in equation 2.37 with following depth dependent function

$$\tilde{\eta}_i(y) = \frac{\eta_i}{\sqrt{2\pi}\sigma_{y,i}} e^{-\frac{y^2}{2\sigma_{y,i}^2}} \tag{3.27}$$

an expression for the characteristic fluorescence of an element can be derived:

$$\begin{aligned} \Phi_i(x) &= \Phi_0 \sigma_{F,i} \rho_i \int_{d_1}^{d_2} \tilde{\eta}_i(\zeta - x) \exp(-\tilde{\mu}_{lin,i}\zeta) d\zeta \\ &= \frac{\Phi_0 \eta_i \sigma_{F,i} \rho_i}{2} \times \exp\left(\frac{(\bar{\mu}_{lin,i}\sigma_{y,i})^2}{2}\right) \times \exp(-\bar{\mu}_{lin,i}x) \times \end{aligned} \tag{3.28}$$

$$\left[erf\left(\frac{d_2+\bar{\mu}_{lin,i}\sigma_{y,i}^2-x}{\sqrt{2}\sigma_{y,i}}\right)-erf\left(\frac{d_1+\bar{\mu}_{lin,i}\sigma_{y,i}^2-x}{\sqrt{2}\sigma_{y,i}}\right)\right]$$

The fluorescence equation is now dependent on the position x in relation to the sample surface, due to the fact that the probing volume probes just a small volume and not the integrated sample as in XRF spectroscopy. Expression 3.28 describes the net peak intensity of a fluorescence peak of an element i as a function of depth, a so-called depth profile, see chapter 2.4.2.

Most important to note is that it is an intrinsic property of 3D Micro-XRF, that the value which determines the intensity is the local density ρ_i of an element i. Equation 3.28 consists of four terms which are separated by the '×' sign. In the following an illustration these factors will be given.

The first factor is a constant term including the local density ρ_i which determines the absolute fluorescence intensity. It describes the intensity one would obtain with the probing volume completely inside the sample and with negligible absorption. The second term is an exponential function and corrects for the actual extension of the probing volume. Radiation originating from deeper parts of the probing volume is absorbed stronger than radiation from parts of the volume closer to the surface of the sample. The third term is a Lambert-Beer term, which stands for the decrease of the intensity at probing depth x due to absorption. Absorption of the impinging beam and absorption of the characteristic radiation are taken into account. Finally, the error functions are important if the probing volume intersects the layer boundaries.

3.2.1 Simulation

In order to clarify equation 3.28 an example of a 200 µm thick homogeneous SiO_2 sample with 50 ppm of CaO, Fe_2O_3, SrO and PbO was simulated. For the calibration parameters a typical calibration was used (April 2008, see chapter 4.1), which takes into account the energy-dependency of the spot sizes *and* the transmissions of the lenses.

Figure 3.6 illustrates the different factors in equation 3.28 once again. In the graphs the surface is on the left - in this case at the position 0.0 µm. The investigation of the Pb concentration profile of the SiO_2 sample would be a step function, see graph 1 in figure 3.6, without resolution or absorption effects. The error function term, factor four in equation 3.28, introduces smooth edges due to the convolution of probing volume and sample geometry, see graph 2. The third term is an absorption term which distorts the profile according to the fluorescence energy, see graph 3. This distortion enhances the intensity in front of the sample surface ($\exp(-\bar{\mu}_{lin,i}y) > 1$) and gradually decreases the intensity for positions inside the sample. The second term is a positive correction term. The first term scales this graph (graph 4) to the absolute value, see Pb-depth profile in the left graph of figure 3.8.

Figure 3.7 shows the three discussed factors for the other three elements, analog to the fourth graph in figure 3.6. Depending on the fluorescence energy and line, the resulting depth profile is extremely different. For Ca the width of the probing volume is biggest, which leads to a broader edge region as well as a bigger influence of the

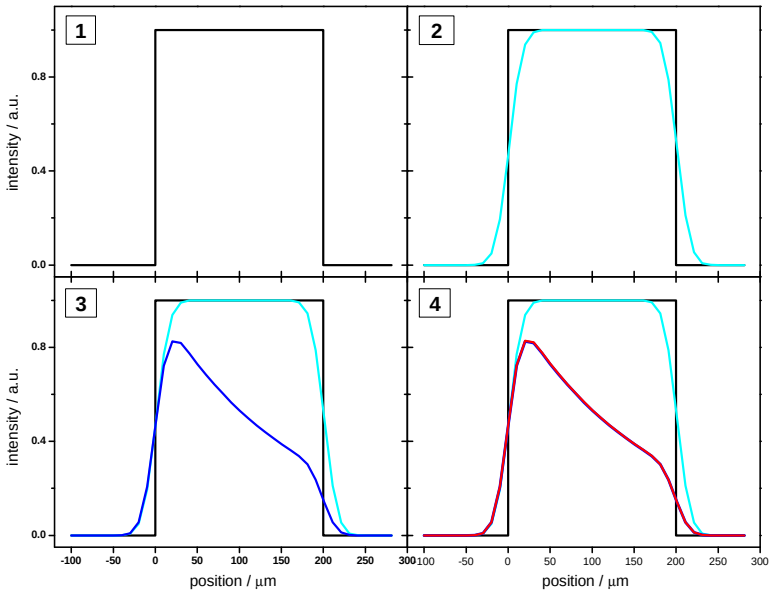

Figure 3.6: The four factors of equation 3.28 are illustrated with the help of the Pb-Lα depth profile of an SiO_2 sample with a thickness of 200 µm.

positive correction factor. The intensity does not reach the value 1 due to absorption, i.e. absorption effects start before the probing volume is completely inside the sample. The position of the sample surface is close to the maximum of the profile. As the other extreme, the position of the surface almost coincides with the half value of the Sr-Kα depth profile. In the case of Sr, fluorescence intensity can be detected throughout the whole sample. Interpretation of high energy profiles is clearly more straight forward than for elements with low fluorescence energies.

Figure 3.8 shows the depth profiles of all four traces in the SiO_2 matrix. The left graph shows the absolute values and the right graph is normalized to one in order to illustrate the shape of the profiles. When moving the sample through the probing volume the intensity rises due to the intersection of probing volume and sample surface. It then declines again due to absorption effects and falls to zero at the latest, when the probing volume has left the sample. These two graphs can clarify some characteristics of 3D Micro-XRF concerning energy dependency.

Energy effects

The difficulty when interpreting such depth profiles is, that the energy dependence of both the sensitivity as well as the width of the probing volume have to be taken into account.

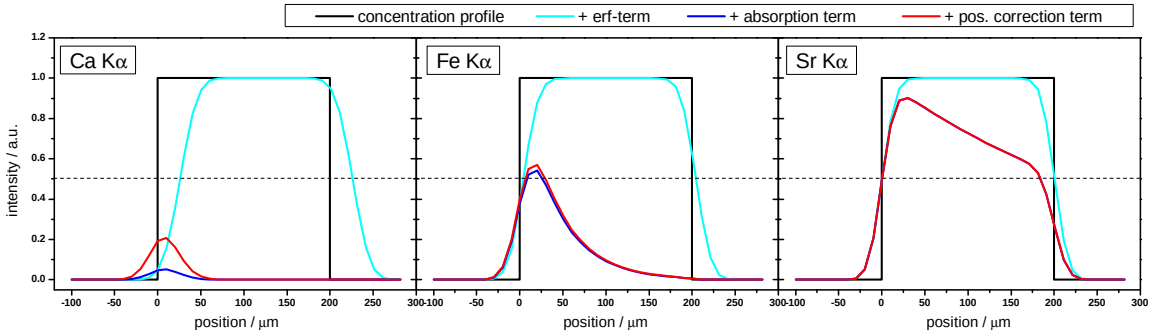

Figure 3.7: Factors, that distribute to the fluorescence intensity, are illustrated with the help of Ca-Kα, Fe-Kα and Sr-Kα depth profiles.

All trace elements in the simulated example are present in equal concentrations. The absolute fluorescence intensity value, though, shows extreme differences. This is because of the factor one of equation 3.28:

$$\frac{\Phi_0 \eta_i \sigma_{F,i} \rho_i}{2} \tag{3.29}$$

The excitation intensity Φ_0 is equal for all elements in the matrix. All other factors differ. A concentration of 50 ppm of the oxides and a typical density of 2.2 g/cm^3 leads to the local densities ρ_i listed in table 3.2. The fluorescence production cross section $\sigma_{F,i}$ increases with increasing fluorescence energy E_F. The integral sensitivity is maximal for Fe-Kα fluorescence due to the shape of the transmission function of the second polycapillary halflens. These different factors lead to the effect, that the Sr-Kα depth profile is the most intense followed by Pb, Fe and Ca.

The shape of the four depth profiles is mainly a function of energy, also, see right graph of figure 3.8. The lower the fluorescence energy, the earlier there is a rise in fluorescence intensity. The higher the fluorescence energy, the less absorption takes place. Note, that neither the maximum of the profiles nor the half value (dotted line) can be used as a measure for the position of the surface although the half value position for Sr is a good initial value for the sample surface. Nevertheless, the difference in σ_y ($\sigma_{y,Ca} - \sigma_{y,Fe} : \sigma_{y,Fe} - \sigma_{y,Pb} : \sigma_{y,Pb} - \sigma_{y,Sr} = 6.3 : 3.7 : 1$) is reflected in the position of the half value - $\approx 7 : 4 : 1$. For light elements the information depth is small, which in this example makes it impossible to reconstruct the local density of Ca after about 50 µm.

Qualitative analysis for the sake of identifying layers, their composition and succession must be performed very carefully. Sample boundaries must be interpreted on the basis

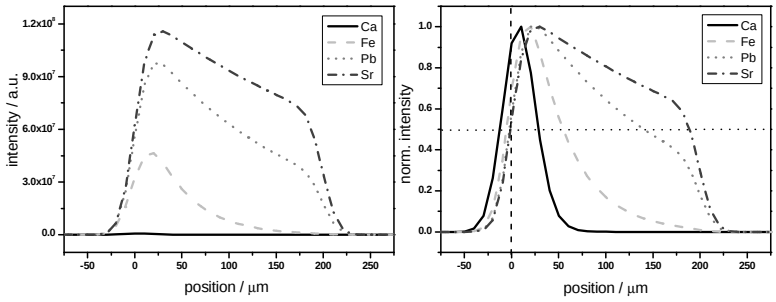

Figure 3.8: left: Depth profiles of traces in a SiO_2 matrix; right: Normalized depth profiles

	Ca-Kα	Fe-Kα	Sr-Kα	Pb-Lα
atomic number	20	26	38	82
E_F / keV	3.6	6.4	14.14	10.55
ρ_i / mg/cm^3	7.92	7.7	9.46	10.12
$\sigma_{F,i}$ / cm^2/g	1.9	8.9	40.8	12.8
η_i / cm	$2.5 \cdot 10^{10}$	$11.9 \cdot 10^{10}$	$3.4 \cdot 10^{10}$	$9.1 \cdot 10^{10}$
$\sigma_{y,i}$ / µm	15.5	13.6	12.2	12.5
$\bar{\mu}_{lin,i}$ / cm^{-1}	1085	238	32	63

Table 3.2: Energy-dependent parameter of a 200 µm thick SiO_2 sample with 50 ppm of CaO, Fe_2O_3, SrO and PbO.

of high energy depth profiles. Because the maximal intensity is almost reached for such profiles, the position of the half value is a good measure for the sample surface. A shift of more than 11 µm as in the presented example for the position at half value results from only 3.3 µm difference in the width of the probing volume (see $\sigma_{y,i}$ in table 3.2) in addition to matrix effects. For samples with obvious layer sequence and small absorption qualitative interpretation can nevertheless yield valuable information, as will be discussed in chapter 5.

3.2.2 Scattering

When X-rays interact with matter, two additional mechanisms occur - elastic and inelastic scattering, see section 2.1.2. Analog to the expression for the fluorescence intensity we can find equivalent equations for the two scattering types:

$$\Phi_{Sc}(x) = \frac{\Phi_0 \eta_{Sc} \sigma_{Sc} \rho}{2} \times \exp\left(\frac{(\bar{\mu}_{lin,Sc}\sigma_{y,Sc})^2}{2}\right) \times \exp(-\bar{\mu}_{lin,Sc} y) \times \left[erf\left(\frac{d_2 + \bar{\mu}_{lin,Sc}\sigma^2_{y,Sc} - y}{\sqrt{2}\sigma_{y,Sc}}\right) - erf\left(\frac{d_1 + \bar{\mu}_{lin,Sc}\sigma^2_{y,Sc} - y}{\sqrt{2}\sigma_{y,Sc}}\right)\right] \quad (3.30)$$

where the index Sc may be Compton or Rayleigh. As discussed in section 2.1.2 the scattering cross sections are functions of the scattering angle for polarized radiation. Thus, when describing experimental data obtained at the synchrotron, where the radiation is linear polarized in the ring plane, see section 2.2.1, the differential polarized cross sections must be used.

The difference between equation 3.28 and 3.30, besides the obvious change in cross sections, is, that the density ρ of the sample determines the absolute scattered intensity. Up until now, analog to the fluorescence equation, only first order effects are taken into account. This as a first approximation can be justified by ...

Thus, when using the scattering depth profiles together with the fluorescence depth profiles additional information can be derived. The Compton profile gives insights into the density variations of the sample into the depth as the Compton cross section is fairly independent on the atomic number of the scattering atom. Rayleigh scattering on the other hand is a function of density and matrix composition. And exactly these two parameters - density and matrix compositions are important prerequisites for the quantification of the fluorescence depth profiles.

3.2.3 Calibration

As mentioned before the two new parameters σ_y and η substitute the calibration constant in XRF. They are functions of the FWHM and the transmissions of the used lenses as well as dependent on the geometry and detection efficiency. In the simplest case they can be described by

$$\sigma_y = \sqrt{\sigma_A(E_0)^2 \sin^2(\Psi) + \sigma_D(E_i)^2 \cos^2(\Psi)} \quad (3.31)$$

and

$$\eta = \frac{\Omega T_A(E_0) T_D(E_i) \epsilon}{\sqrt{8\pi}} \frac{\sigma_D(E_i)^2}{\sqrt{\sigma_A(E_0)^2 + \sigma_D(E_i)^2}} \quad (3.32)$$

The exact shape and value of FWHM and transmission of a polycapillary halflens is extremely dependent on the use of the optic [WMM+09]. A slight misalignment also alters the sensitivity function as discussed in section 3.1. These aspects and the fact, that the solid angle of detection is difficult to measure absolutely makes a calibration mandatory.

When using thin one-element foils self-absorption of radiation can in some cases be negligible, so that equation 3.28 can be written as [Mal04]

$$\Phi_i(x) = \Phi_0 \, \tilde{\eta}_i(x) \, \sigma_{F,i} \, m_i \quad (3.33)$$

with m_i the area density of the element. This equation immediately yields both characteristic parameters for the fluorescence line energy of the investigated element. The disadvantage of a calibration routine with thin foils is the handling of the foils and the necessity of numerous measurements.

The calibration time can be significantly reduced, when using thick multi-element samples. Measurement of such multi-element standards leads to a system of equation for all measurable elements of the sample, which are coupled through the effective linear mass absorption coefficient. If we consider a reference sample with infinite thickness, equation 3.28 simplifies as follows:

$$\begin{aligned} \Phi_i(x) &= \frac{\Phi_0 \eta_i \sigma_{F,i} \rho_i}{2} \exp\left(\frac{(\bar{\mu}_{lin,i}\sigma_{y,i})^2}{2}\right) \exp(-\bar{\mu}_{lin,i} y) \times \\ &\quad \left[1 - erf\left(\frac{d_1 + \bar{\mu}_{lin,i}\sigma_{y,i}^2 - x}{\sqrt{2}\sigma_{y,i}}\right)\right] \end{aligned} \tag{3.34}$$

With full knowledge of the composition and density of the sample as well as the incoming radiation, the system is decoupled and the only two unknown parameters in equation 3.34 are σ_y and η. Thus, a calibration procedure is made feasible.

Scattering

As discussed before, not only fluorescence information can be used for the analysis of a sample, but the scattered information is valuable, also. Analog to equation 3.34 an equation for the scattered radiation can be found, when substituting $\sigma_{F,i}$ with σ_{Sc}, ρ_i with ρ and $\bar{\mu}_{lin,i}$ with $\bar{\mu}_{lin,Sc}$, see equation 3.30. The calibration parameters are then η_{Sc} and $\sigma_{y,Sc}$, where the subscript Sc may mean Compton or Rayleigh.

Details on the calibration procedure will be discussed in section 4.1. Important to note is, that both characteristic parameters are functions of energy due to the energy dependence of σ_A, σ_D, T_A and T_D.

3.3 Stratified Samples

In practice most samples are not homogeneous. A quantification for stacks of homogeneous layers was developed. The difference to a homogeneous sample is the absorption of exciting and fluorescence radiation by layers which are situated on top of the measuring position. Equation 3.28 must therefore be modified as follows:

$$\begin{aligned} \Phi(y) &= \frac{\Phi_0 \eta \sigma_F}{2} \sum_k \rho_{i,k} \left[\prod_{j=1}^{k-1} e^{-\bar{\mu}_{lin,j}(d_j - d_{j-1})}\right] e^{-\bar{\mu}_{lin,k}(y - d_{k-1})} e^{\frac{(\bar{\mu}_{lin,k}\sigma_y)^2}{2}} \times \\ &\times \left[erf\left(\frac{d_k + \bar{\mu}_{lin,k}\sigma_y^2 - y}{\sqrt{2}\sigma_y}\right) - erf\left(\frac{d_{k-1} + \bar{\mu}_{lin,k}\sigma_y^2 - y}{\sqrt{2}\sigma_y}\right)\right] \end{aligned} \tag{3.35}$$

with k the number of layers of the sample. The analog scattering equation can be written as

$$\begin{aligned}\Phi(y) &= \frac{\Phi_0 \eta_{Sc} \sigma_{Sc}}{2} \sum_k \rho_k \left[\prod_{j=1}^{k-1} e^{-\bar{\mu}_{lin,j}(d_j - d_{j-1})} \right] e^{-\bar{\mu}_{lin,k}(y-d_{k-1})} e^{\frac{(\bar{\mu}_{lin,k}\sigma_{y,Sc})^2}{2}} \times \\ &\times \left[erf\left(\frac{d_k + \bar{\mu}_{lin,k}\sigma^2_{y,Sc} - y}{\sqrt{2}\sigma_{y,Sc}} \right) - erf\left(\frac{d_{k-1} + \bar{\mu}_{lin,k}\sigma^2_{y,Sc} - y}{\sqrt{2}\sigma_{y,Sc}} \right) \right] \end{aligned} \quad (3.36)$$

With these expressions it is possible to reconstruct thickness and elemental composition of stratified samples. After a successful calibration only the density ρ, the local densities ρ_i and the layer boundaries d_k are unknown. By first fitting the scattered profiles and then analyzing the fluorescence profiles an unknown sample can be fully described, thus rendering 3D Micro-XRF into a true analytical tool for layered samples.

3.4 Polychromatic excitation

In the above sections the quantification of 3D Micro-XRF with monochromatic excitation was discussed. Monochromatic 3D Micro-XRF is up until now limited to the use at a synchrotron facility. As synchrotron experiments involve high cost and little time, a quantification for measurements of X-ray tube 3D Micro-XRF spectrometers is desirable.

Monochromatizing the X-ray tube beam in order to avoid the more complex task of polychromatic quantification is not yet feasible with existing optics. Experiments in our group were performed with a multilayer monochromator (Astix-Modified Montel Optic of AXO Dresden) coupled to a molybdenum X-ray tube [Sei08]. Although the experiment can be performed, the resulting fluorescence is not intense enough for practicable analysis. To our knowledge, monochromatic 3D Micro-XRF spectrometers do not exist in other groups, either.

Polychromatic 3D Micro-XRF, though, is employed by different groups throughout the world [KMR03, LWC$^+$07, PH06, TND07]. Adequate quantification schemes have not been published, yet. This section will introduce the difficulties of polychromatic excitation as well as present first theoretical considerations.

3.4.1 Theory

The difficulty with polychromatic excitation is, that the spot size σ_A and the transmission T_A of the first lens are not constant compared to experiments with monochromatic excitation. The excitation spectrum of the tube is transported through the first X-ray lens, resulting in a mixture of spot sizes and transmission values weighed by the intensity distribution of the spectrum.

Figure 2.5 on page 11 shows simulated spectra for six different acceleration voltages of a Molybdenum X-ray tube. X-ray tube spectra can be divided into the Bremsstrahlung and the characteristic fluorescence lines of the anode material.

The probability for the emission of a characteristic line is maximal for excitation energies close to the absorption edge of the line and decreases with increasing energy. Thus, for the production of f.e. a Ca-Kα fluorescence photon only the portion of the transmitted spectrum above the K-absorption edge can be responsible.

For 3D measurements that means, that the excitation spectrum is first modified by the transmission of the first lens. Then, according to the elements in the sample different portion of this spectrum can excite the different atoms. The fluorescence is then again modified through the transmission of the second lens. The fluorescence equation must be written as:

$$\Phi_i(x, E_{max}) = \int_{E_{edge}}^{E_{max}} \sigma_{F,i}(E)\Phi_0(E) \int_{d_1}^{d_2} \tilde{\eta}_i(\zeta - x, E)\rho(\zeta)e^{-\bar{\mu}_i(E)\rho(\zeta)\zeta} d\zeta dE \tag{3.37}$$

with

$$\tilde{\eta}_i(y, E) = \frac{\eta_i(E)}{\sqrt{2\pi}\sigma_{y,i}(E)} e^{-\frac{y^2}{2\sigma^2_{y,i}(E)}} \tag{3.38}$$

The two characteristic parameters integral sensitivity η and width of the probing volume σ_y are not only dependent on the fluorescence element i, but also functions of the energy which is transported by the first lens:

$$\sigma_{y,i}(E) = \sqrt{\sigma_D^2(E_i)\sin^2(\Psi) + \sigma_A^2(E)\cos^2(\Psi)} \tag{3.39}$$

and

$$\eta_i(E) = \frac{\Omega T_A(E) T_D(E_i)\epsilon}{\sqrt{8\pi}} \frac{\sigma_D^2(E_i)}{\sqrt{\sigma_A^2(E) + \sigma_D^2(E_i)}} \tag{3.40}$$

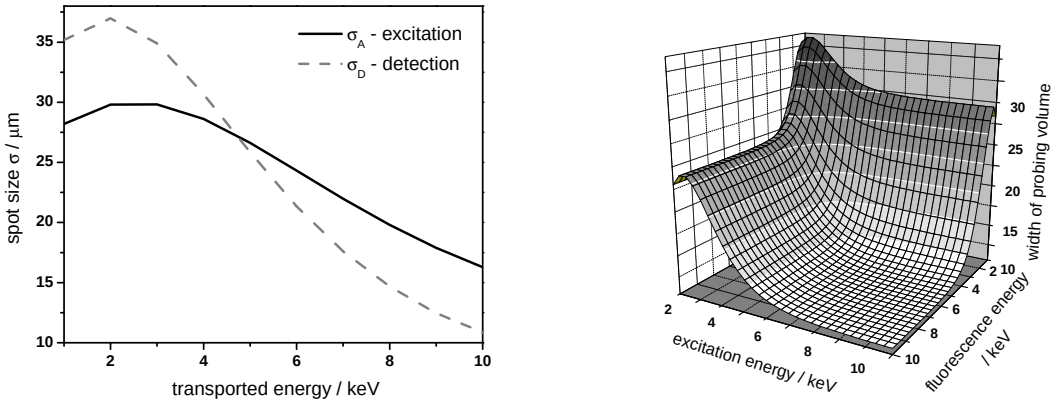

Figure 3.9: Left: Two random spot size functions. Right: Calculation of the width of the probing volume according to equation 3.39 for the two spot size functions and $\Psi = 45°$.

In figure 3.9 (left graph) two random spot size functions were chosen to illustrate the differences for the quantification for polychromatic excitation. With these two functions the width of the probing volume can be calculated according to equation 3.39 as shown in the right graph. The width of the probing volume is a function of excitation and detection energy.

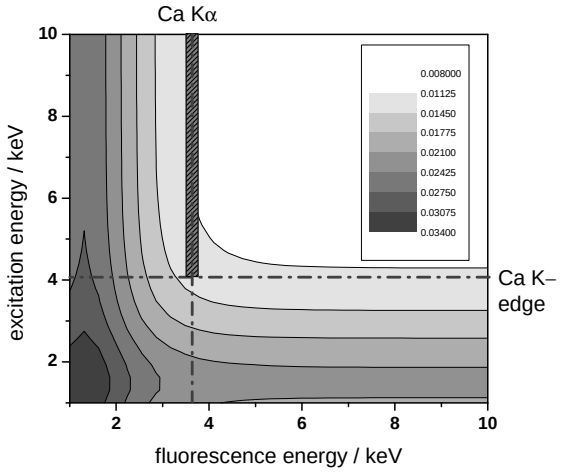

Figure 3.10: For the Ca-Kα fluorescence line the width of the probing volume is a mix of all widths at this fluorescence energy above the Ca-K edge excitation energy, here marked with a hatched rectangle.

If a specific fluorescence line, like Ca-Kα, is analyzed, different values for σ_y according to the excitation spectrum must be taken into account. A mix of all widths at the fluorescence energy of the Ca-Kα line with excitation energies between the Ca-K edge and the maximal energy of the spectrum are present. In figure 3.10 these values are marked with a hatched rectangle. For the integral sensitivity the analogous picture using equation 3.40 can be employed to get an idea of the complexity of the radiation transport.

3.4.2 Thin Foils

In the case of thin homogeneous foils the absorption is negligible and equation 3.37 can be simplified to

$$\Phi_i(x, E_{max}) \quad = \quad \rho D \int_{E_{edge}}^{E_{max}} \sigma_{F,i}(E)\Phi_0(E)\eta_i(x, E)dE \tag{3.41}$$

The integrand is the product of the excitation spectrum $\Phi_0(E)$, the fluorescence production cross section $\sigma_F(E)$ and the sensitivity function $\eta_i(E)$. The excitation spectrum

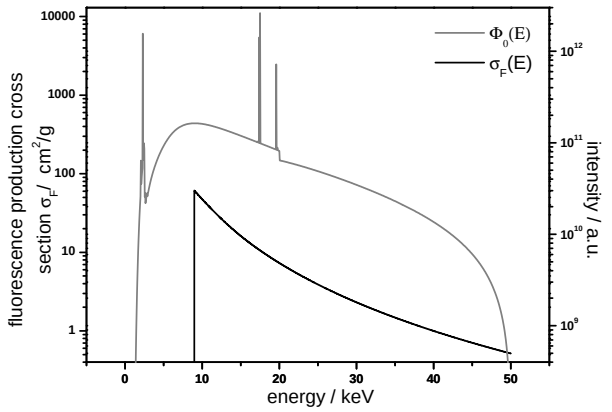

Figure 3.11: The excitation spectrum $\Phi_0(E)$ with E_{max}= 50 keV of section 2.2.1 and the fluorescence production cross section $\sigma_F(E)$ for the Cu-Kα fluorescence line are functions of energy.

consists of the Bremsstahlung background and the characteristic lines, see figure 2.5. The energy dependency of the fluorescence production cross section is due to the mass photoelectric absorption coefficient and thus monotonically decreasing between absorption edges. The product of $\sigma_F(E)$ and $\Phi_0(E)$ can be understood as a weighing factor for the sensitivity function. Figure 3.11 shows the excitation spectrum $\Phi_0(E)$ with E_{max} = 50 keV of section 2.2.1 and the fluorescence production cross section $\sigma_F(E)$ for Cu-Kα fluorescence line. The product of these two functions determines the mixing of sensitivity function values. In figure 3.12 this product is calculated for five selected fluorescence lines.

For elements with low absorption edge energy the integral will be dominated by energy values close to the absorption edge, while for elements with higher absorption energy the integral is dominated by the characteristic line energies. In section 2.2.1 the calculation of X-ray tube spectra showed, that the changing of the maximum voltage changes the shape of the background significantly concerning the median energy. The characteristic lines, though, are always at the same energy. Thus, the changing of the maximum voltage changes of the X-ray tube will significantly change f.e. the width of the probing volume for Cr-Kα fluorescence, while it will be negligible for Pb-Lα fluorescence.

Figure 3.13 shows measurements performed with the compact 3D Micro-XRF spectrometer described in section 2.4.2. Nine elemental foils with thicknesses of 1 to 2 µm were scanned with 5 µm step widths and live times of 50 to 200 s. The effective FWHMs were obtained with a Gaussian fit function as a measure for the overall width of the probing volume. The FWHMs decrease with increasing fluorescence energy as expected. Also the higher the maximum voltage the smaller the width of the probing volume. The differences of FWHM decrease with increasing energy.

For a higher maximum excitation energy more smaller spot sizes are used, thus, the

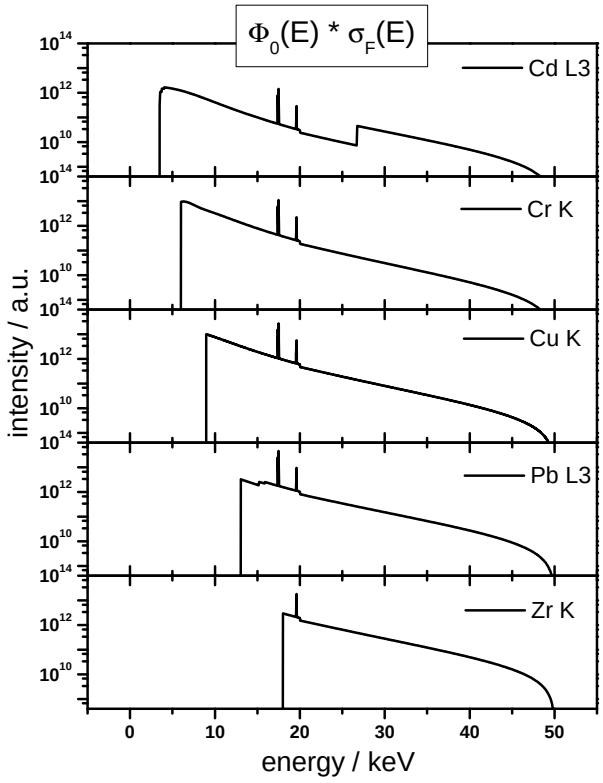

Figure 3.12: The product of the excitation spectrum $\Phi_0(E)$ with E_{max}= 50 keV and the fluorescence production cross section $\sigma_F(E)$ for a selection of fluorescence lines.

overall spot size is smaller. As expected the spot size is not influenced significantly by the different maximal voltage values for higher fluorescence line energies, while the differences are enhanced for lower fluorescence energies.

The same considerations concerning the weighed mixing of values can be applied to the integral sensitivity. As a consequence of these aspects, it is mandatory for a quantification to investigate the full 2D maps of the width of the probing volume as well as the integral sensitivity. The possibility to know the absolute values for the spot sizes and transmissions of the used lenses was proved to be non practicable, see section 2.2.3. Therefore a calibration procedure similar to the one used for monochromatic excitation measurements must be developed.

3.4.3 Calibration

In the case of monochromatic excitation the excitation energy is constant, only the fluorescence energy must be varied in order to calibrate the setup. Thus, only a horizontal

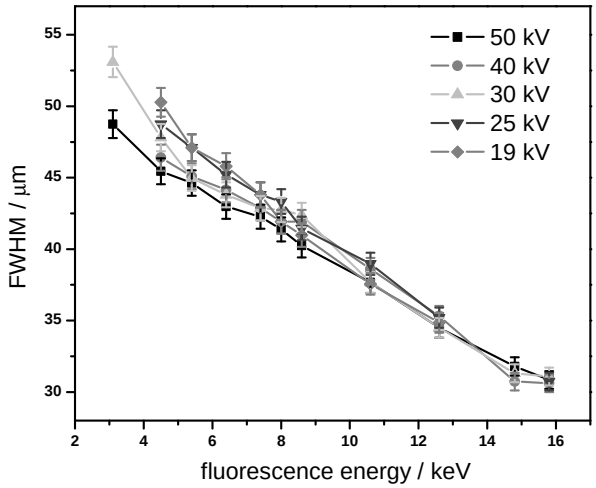

Figure 3.13: FWHM obtained by the scanning of thin foils at different maximal voltages of the excitation spectrum. Experiments were performed with the compact spectrometer described in section 2.4.2.

cross section of the two-dimensional map in figure 3.10 must be characterized. That is the reason, why the measurement of thick glass reference samples is an adequate tool for the determination of the characteristic parameters. In case of polychromatic excitation, though, the full map must be known in order fully calibrate the system. The idea for a calibration is to use thin elemental foils and vary the maximum excitation energy of the X-ray spectrum.

The fluorescence intensity equation for thin foils with thickness D and density ρ is a function of the spot sizes σ_A, σ_D and the transmissions T_A,T_D of the used optics:

$$\begin{aligned}\Phi_i(x, E_{max}) &= \rho D \int_{E_{edge}}^{E_{max}} \sigma_{F,i}(E)\Phi_0(E)\frac{\eta_i(E)}{\sqrt{2\pi}\sigma_{y,i}(E)} e^{-\frac{x^2}{2\sigma^2_{y,i}(E)}} dE \\ &= \rho D \frac{\Omega\epsilon}{4\pi} \int_{E_{edge}}^{E_{max}} \sigma_{F,i}(E) * \Phi_0(E) * F(x, T_A, T_D, \sigma_A, \sigma_D) dE\end{aligned} \tag{3.42}$$

with

$$\begin{aligned}F(x, T_A, T_D, \sigma_A, \sigma_D) &= \frac{T_A(E)T_D(E_i)}{\sqrt{\sigma_A^2(E) + \sigma_D^2(E_i)}} \frac{\sigma_D^2(E_i)}{\sqrt{\sigma_A^2(E)\sin^2(\Psi) + \sigma_D^2(E_i)\cos^2(\Psi)}} \\ &\quad \exp(-\frac{x^2}{2(\sigma_A^2(E)\cos^2(\Psi) + \sigma_D^2(E_i)\sin^2(\Psi))})\end{aligned} \tag{3.43}$$

These are all functions of the transported energy and can be described by extreme functions or linear exponential functions, as explained in 2.2.3. This means, that using

two extreme functions for the transmission and two exponential functions for the spot sizes, fourteen unknown parameters must be obtained through a calibration.

Measurements of different foils of elements i with different maximal X-ray tube energies E_{max} yield this possibility. The full depth profiles $\Phi_i(x, E_{max})$ must be fitted with equation 3.42 simultaneously. In order to obtain the transmission and spot size functions unambiguously numerous measurements are necessary as the full 2D maps must be reconstructed.

The calibration with this proposed model is time consuming as a big number of scans on thin foils must be employed. Additionally, the results of the calibration algorithm must be judged carefully as it will not be unique. On the other hand the use of new compact 3D Micro-XRF spectrometers requires only one calibration after the first alignment and after that only if changes in the performance can be observed.

The fitting of fourteen parameters demands a more complex fitting routine than simple least square fitting. As a tool for the fitting of many parameters a genetic algorithm has proved to be an adequate tool [Man05]. The fitting algorithm was implemented and tested on simulated data, yielding no stable results yet. Due to time limits further work on this subject will be done in future projects.

3.4.4 Reconstruction

If the 2D maps of the width of the probing volume and the integral sensitivity are known, a reconstruction of unknown samples is the next step. For thick homogeneous samples following equation system must be solved.

$$\begin{aligned}\Phi_i(x) &= \int_{E_{edge}}^{E_{max}} \frac{\Phi_0(E)\eta_i(E)\sigma_{F,i}(E)\rho_i}{2} \times \exp\left(\frac{(\bar{\mu}_{lin,i}(E)\sigma_{y,i}(E))^2}{2}\right) \times \exp(-\bar{\mu}_{lin,i}(E)x) \times \\ &\quad \left[erf\left(\frac{d_2 + \bar{\mu}_{lin,i}(E)\sigma^2_{y,i}(E) - x}{\sqrt{2}\sigma_{y,i}(E)}\right) - erf\left(\frac{d_1 + \bar{\mu}_{lin,i}(E)\sigma^2_{y,i}(E) - x}{\sqrt{2}\sigma_{y,i}(E)}\right)\right] dE\end{aligned}$$

In principal, all parameters except the local densities of the elements and the layer thicknesses are known and, thus, a reconstruction is possible. The computational complexity, though, is by far greater than for monochromatic excitation due to the additional energy dimension. Further work should be invested as to find a simplification for the expression.

In XRF analysis the concept of the effective wavelength was introduced in the 1960s [SF66, TC82]. On account of the difficulties encountered through polychromatic excitation, a monochromatic wavelength is defined that is representative of the whole spectrum. This concept might be the solution for the quantification for polychromatic quantification, also. This effective energy would be influenced by the sample, the excitation spectrum and the sensitivity function. The sensitivity function derived through the calibration described in the last section is therefore the most important prerequisite for this kind of evaluation.

4 Reconstruction of thickness and composition

This chapter deals with the quantification of SR 3D Micro-XRF measurements, more precisely the possibility to reconstruct the composition and thickness of layers of stratified samples. The quantification is a two-phase process. As a first step a calibration is mandatory in order to obtain the width of the probing volume σ_y and the integral sensitivity η, the two characteristic parameters, which determine the experimental setup. A calibration procedure was implemented in a python based least square algorithm. The self-developed algorithm works stable and unambiguous and the procedure will be discussed in detail in the first section of this chapter.

The quantification of unknown layered samples is numerically a more challenging task involving the solution of a coupled system of fluorescence and scattering intensity equation, see section 3.3. A second python-based least square algorithm based on equation 3.35 was developed. Prerequisites for the algorithm are the density of the layers and their dark matrix. As this information is in most cases difficult to obtain, the quantification of the scattered radiation based on equation 3.36 was included in the quantification process.

When investigating an unknown sample, an initial value for the matrix composition must be given in order to start the fitting routine. This first guess is in most cases easily obtained through the nature of the sample, i.e. if it is a glass sample, a parchment sample aso.. Then, through the fitting of the scattered radiation, the densities of the layers of the sample are derived. Successively the local densities are obtained through the fitting of the fluorescence intensities. Thus, with a good guess of the matrix of a sample, layer thicknesses and compositions can be reconstructed without the need for sampling or sectioning of an object.

The quantification software has been developed to be flexible according to the analytical problem at hand. It allows the fitting of concentrations and local densities, of elements and oxides. If the density of a sample is known it can be included as a fixed value. The fit of the fluorescence depth profiles can be performed with or without weighing according to the intensity. For known chemical stoichiometries non-visible elements like N or O can be calculated in each fit iteration a.s.o. The validation of the quantification procedure is presented in the second part of this chapter. The third section gives an overview of the reconstruction possibilities and a first application example.

4.1 Calibration

In section 3.2.3 the principle of calibrating a 3D Micro-XRF setup with monochromatic excitation was introduced. In principle a calibration is valid for one excitation energy, one geometry and one set of used lenses. Changing any of these factors makes a new calibration mandatory.

A different excitation energy implies a different FWHM and transmission of the first lens, thus altering the values of the width of the probing volume σ_y and the integral sensitivity η. As discussed in section 3.1 the sensitivity of a setup is also highly dependent on the alignment of the foci of the used optics.

In the course of this work eight beamtimes consisting of one to two weeks of measuring time were evaluated. A calibration is necessary for each beamtime because the alignment cannot be assumed exactly equal even if excitation energy and hardware are the same as in a previous beamtime. Additionally, whenever the excitation energy is changed or the setup is modified according to specific experimental needs, a new calibration is required. In this section a few more important notes on practical issues of the calibration are stated and in the following different kinds of calibration aspects are shown and discussed.

4.1.1 Calibration routine

The system of equations for the measurement of a thick multi-element standard was introduced in section 3.2.3. For each fluorescence peak in the measured spectra (compare figure 2.10) a depth profile is obtained, which can be treated separately because of the full knowledge of sample composition and density.

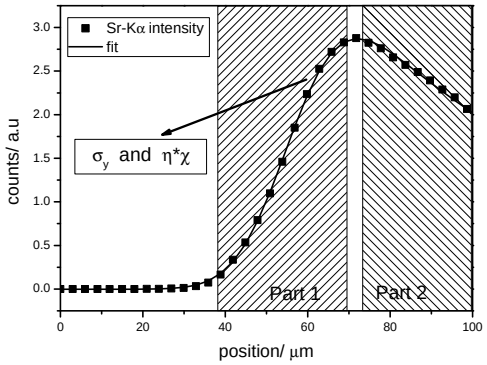

Figure 4.1: Sr-Kα depth profile of a thick glass reference sample (Breitländer D3)

Figure 4.1 shows as an example the depth profile of the Sr Kα-fluorescence of a thick glass reference standard (Breitländer D3). In part one of the depth profile the curvature introduced by the error-function term is visible and the decrease in part 2 is mainly dependent on the absorption of the radiation. By fitting this curve with a python-based least square algorithm the width of the probing volume σ_y and the integral sensitivity

η multiplied with a factor χ are immediately obtained. These two values correspond to the energy of the Sr Kα-fluorescence energy of 14.014 keV for this specific beamtime setup (used lenses, excitation energy and geometry). The factor χ has been introduced in this work, because the excitation intensity Φ_0 is not known in absolute value, but a proportional value obtained with an ionization chamber is available. By successively fitting all depth profiles of the standard, calibration values throughout the measurable range of fluorescence lines can be derived.

Throughout this work a set of six thick glass reference samples of the company Breitländer were used. The manufacturer describes them as 'silica glasses of special composition for XRF-spectrometer recalibration and control'. They are not certified to be homogeneous in the micrometer regime. Other glass reference samples, f.e. the NIST standard reference material 1412, were tested throughout this work. By comparison the Breitländer series proved to be the most reliable concerning homogeneity and certified concentration values. Nevertheless deviations from the certified values have been observed especially for elements with concentrations beneath 0.05 %, which makes the calibration parameters for these fluorescence energies not reliable.

Another aspect for excluding certain depth profiles from the calibration procedure is the overlapping of fluorescence peaks with each other or with the scattered peaks. If a fluorescence peak lies energetically close to another peak a deconvolution procedure must be applied. Especially if the intensity difference of these peaks is considerable, i.e. a small peak is situated on the shoulder of the other intensive peak, the deconvolution will yield values for the small peak with big uncertainties. Thus, for calibration, the small peak would be omitted.

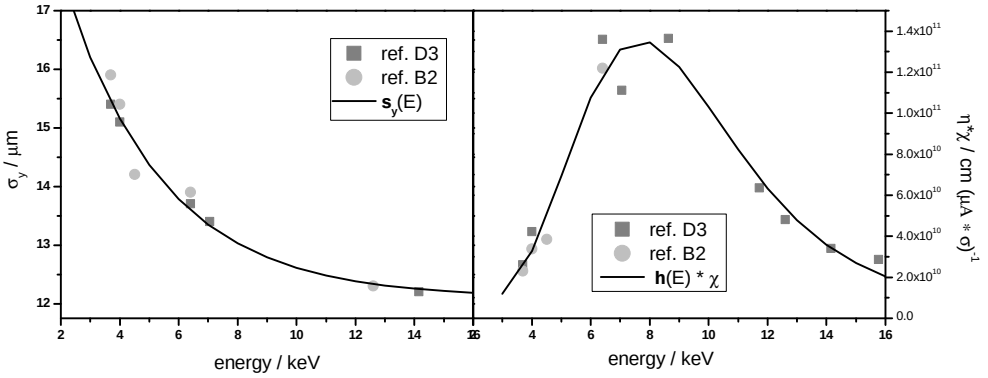

Figure 4.2: Example of typical calibration curves for the width of the probing volume σ_y (left) and the integral sensitivity η multiplied with χ (right) (April 2008, mySpot beamline)

Figure 4.2 shows a typical calibration. The left panel shows the energy-dependency

of the width of the probing volume σ_y and the right panel the shape of the integral sensitivity profile η. In this example of the beamtime in April 2008, only two thick glass reference standards were used.

The values of the integral sensitivity multiplied with χ of different standards show a statistical spread of up to 15 %. The maximum lies between fluorescence energies of 5 - 10 keV. It decreases to lower and to higher energies following roughly a transmission curve of polycapillary halflenses. According to equation 3.10 the integral sensitivity is a function of the transmissions and spot sizes of the used lenses:

$$\eta \propto T_A(E_0)T_D(E_i)\frac{\sigma_D^2(E_i)}{\sqrt{\sigma_A^2(E_0)+\sigma_D^2(E_i)}} \tag{4.1}$$

The excitation energy is a constant, so the integral sensitivity is in first approximation proportional the product of the transmission of the detection lens T_A and its spot size σ_D. Thus, the decrease to higher and lower energies is explained by the shape of the transmission function of the used lens, modified by the monotonically decreasing spot size.

The full width of half-maximum of the focal spot size drops with rising energy due to the decreasing critical angle. The minimal FWHM of 29 µm ($2.355 \cdot \sigma_y$) is obtained for energies above the Kα fluorescence energy of strontium. The values for σ_y of different standards show a statistical spread of ~ 5 %.

As seen in the graph only a limited number of calibration values of each sample were used, as explained before. For not measured fluorescence energies an interpolation with adequate calibration functions is possible, which will be introduced in the next section. The calibration curves hold for K and L-lines with all the associated subshell lines. In the example of figure 4.2 f.e. the Pb Lβ-line at 12.611 keV was used.

The least square algorithm was tested thoroughly in respect to the best fitting strategy. The two calibration parameters are always used as fitting values. The overall density of the sample may be included in the fit parameter space, if it is not known. Separate measurement of the density (f.e. weighing experiment) is nevertheless preferable. The obtained values for σ_y and η are weighed according to the quality of the fit of the depth profile. The smaller the χ^2-value, the more weight the data point has in the determination of the calibration function.

Measurement of two to three standards is sufficient for a satisfactory calibration. If there is prior knowledge of the important elements for a specific analytical question it is desirable to choose reference samples with a considerable content of these elements.

Scattering

The measurement of a thick glass reference sample additionally yields the depth profiles for Compton and Rayleigh scattered radiation. These two additional depth profiles are also fitted with the appropriate analytical function, yielding two pairs of values for $\sigma_{Compton}$, $\eta_{Compton}$, $\sigma_{Rayleigh}$ and $\eta_{Rayleigh}$. For one excitation energy they should be equal for all measured samples. For a more precise measurement of these four values, a highly pure NaCl sample was used in the course of this work.

4.1.2 Calibration functions

The interpolation between measured calibration data must be carried out with adequate calibration functions, both for the width of the probing volume σ_y and the integral sensitivity η. The agreement of these function to the experimental data was tested with different equations.

The width of the probing volume can be written in the simplest case with equation 3.9 and equation 2.27 as

$$\sigma_y(E) = \sqrt{a_0 + \left(a_1 + \frac{a_2}{E}\right)^2} \tag{4.2}$$

with a_i constants. Equation 2.27 was introduced as the shape of the FWHM of a polycapillary without absorption, divergence or illumination effects. In reality the shape of the FWHM function differs significantly [Wol09]. Different monotonically decreasing functions were tested in order to find an equation which shows good agreement with the experimental data and has at the same time minimal free parameters. The analysis of the experimental data showed, that the width of the probing volume can best be described by a linear exponential function with three free parameters:

$$\sigma_y(E) = a_0 + a_1 * \exp(-\frac{E}{a_2}) \tag{4.3}$$

As discussed in section 2.2.3 the transmission of a polycapillary halflens can be described by an extreme function, which has four free parameters. As the integral sensitivity is a function of the transmissions and spot sizes of the lenses the combination of the extreme function with the linear exponential function results in a fitting expression with 9 free parameters. Due to the large uncertainties of the calibration data it is preferable to use a more simple function. The experimental data shows that the integral sensitivity can be described by an extreme function with four free parameters, which means, that the integral sensitivity is dominated by the shape of the transmission function of the second lens:

$$T = T_0 + T_1 \exp(-\exp(-z(E)) - z(E) + 1) \tag{4.4}$$

with $z(E) = (E - E_c)/T_2$ and T_0, T_1, T_2 and E_c the four free parameters.

4.1.3 Thin and thick reference material

According to equation 3.33, thin foils can be used for calibration, as well. In one of the first beamtimes a 3 µm thick Wolfram foil was scanned through the probing volume. The calibration results agree within the spread of experimental data with the values obtained with the Breitländer series, see figure 4.3.

In this example one reference sample A3 was measured twice during the course of the beamtime. Differences for the calibration values for the same elements can be distinguished in figure 4.3. The reason might be a slight misalignment or drift of the excitation beam or micro-inhomogeneities in the reference sample. Typical uncertainties for the measured data lie in the range of up to $10 - 15$ %, even for selected peaks with high

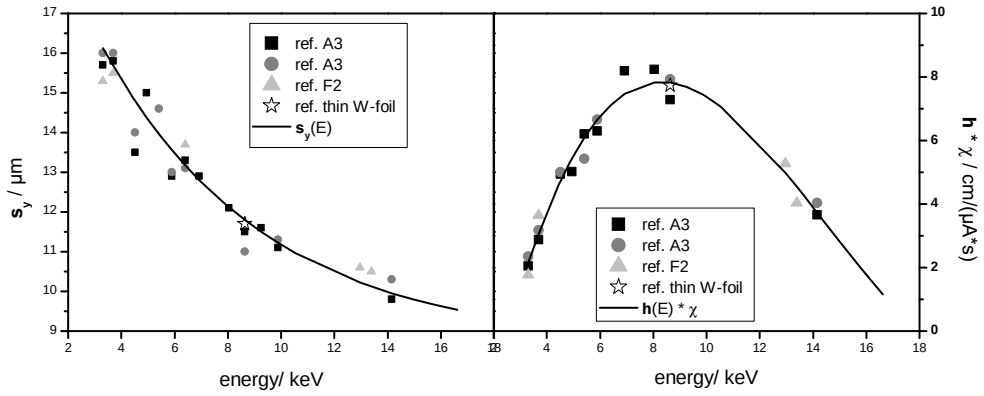

Figure 4.3: Example of one calibration (Aug. 2006, BAMline) with a thin W-foil and three thick glass reference samples.

concentration and without peak-overlapping. These uncertainties influence the quantification of unknown concentrations directly, which will be discussed in section 4.2.

The difference in magnitude for $\eta \cdot \chi$ of the two calibrations of figure 4.2 and 4.3 has its origin in the fact, that the 3D Micro-XRF setups were realized at two different beamlines. In the beginning of this work the BAMline of BESSY II was utilized, while later experiments were carried out at the mySpot beamline with its dedicated endstation for micro analysis, see section 2.4.2. Different lenses were used making a comparison of the calibration impossible.

4.1.4 Different excitation energies

The dependency of the width of the probing volume and the integral sensitivity on the excitation intensity was tested by changing the energy of the beamline.

Figure 4.4 shows the obtained results for E = 16 keV and E = 19 keV. The width of the probing volume σ_y is smaller for 19 keV excitation energy, while the integral sensitivity η is increased compared to the experiment with 16 keV excitation energy.

In order to understand these results, the characteristics of the lens in the excitation channel must be taken into account. This polycapillary halflens was especially developed for the use in the excitation channel of 3D Micro-XRF measurements. The gain factor is optimized for energies between 15 and 20 keV, see table 4.1, which are typical excitation energies for SR XRF. The spot size decreases with increasing energy.

That implies that the spot size of the excitation lens is smaller for a higher excitation energy ($\sigma_A(19\text{ keV}) < \sigma_A(16\text{ keV})$) and that the transmission is higher for a higher excitation energy ($T_A(19\text{ keV}) > T_A(16\text{ keV})$). The width of the probing volume increases with increasing spot size of the first lens, thus explaining the smaller spot size in the

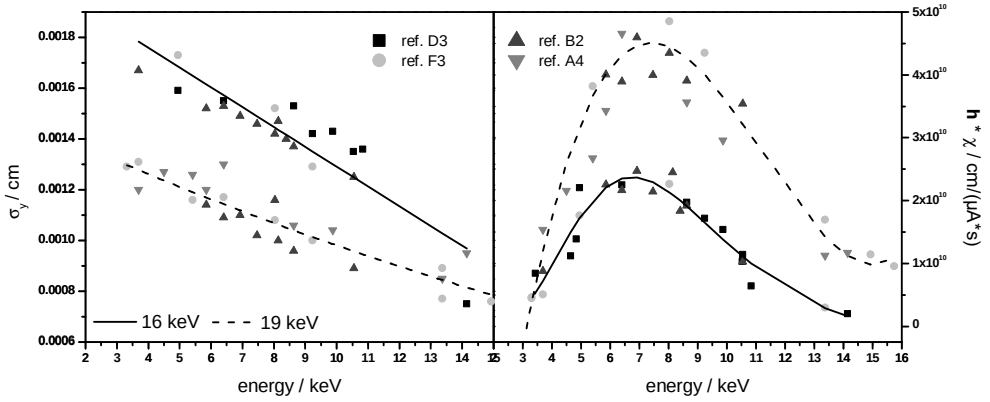

Figure 4.4: Example of two calibrations (Jan. 2007, mySpot beamline) with excitation energy of 16 keV (straight line) and of 19 keV (dashed line).

E / keV	3-5	5-7.5	7.5-10	10-15	15-20	20-25	25-30
spot size / µm	36	35	30	25	24	27	20
gain	1367	3290	3842	4290	4924	2803	758

Table 4.1: Characteristic parameters of 51mls03

case of 19 keV excitation energy. The integral sensitivity decreases with increasing spot size (in the simplest case $\eta \propto 1/\sqrt{\sigma_A^2 + \sigma_D^2}$), but the linear increase with increasing transmission of the first lens $\eta \propto T_A$ dominates the expression. The setup is more sensitive for 19 keV excitation because there is more flux on the sample.

Figure 4.5 shows the product of fluorescence production cross section σ_F and the integral sensitivity η of Ca-, Mn-, Zn-, Rb- and Sr-Kα fluorescence for the two excitation energies. These factors determine the absolute intensity of a fluorescence line. The fluorescence intensity is only slightly increased for the Ca-Kα line, while for higher fluorescence energies 19 keV excitation is by far preferable. In this example there is no advantage neither in resolution nor in intensity when reducing the excitation energy. Other scenarios are possible, when a specific light element is of interest. For a considerable change, the excitation energy must be reduced to lower energies, though, see section 5.2.

4.1.5 Different angles between excitation axis and sample normal

In section 3.1 the angle Ψ between excitation angle and sample normal was not discussed, because it does not change the shape of the ellipsoid. If the spot sizes of both lenses are

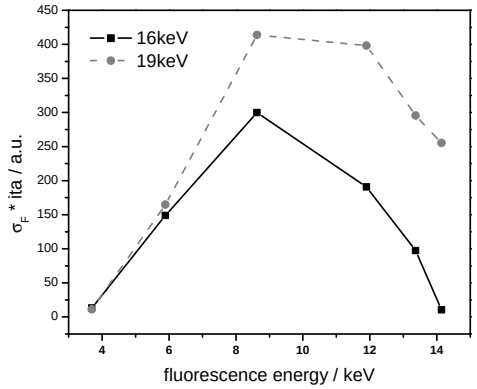

Figure 4.5: The product of fluorescence production cross section σ_F and the integral sensitivity η for excitation energies of 16 keV and 19 keV and six elements were calculated. The solid lines are just a means for guiding the eye. There is no advantage in reducing the excitation energy in this example.

equal, Ψ is irrelevant for the determination of the sensitivity function. This holds at the most only for one fluorescence energy, as the spot size of the second lens is a function of energy. Measurements were performed at the BAMline for $\Psi = 30°$, $\Psi = 45°$ and $\Psi = 60°$, see figure 4.6.

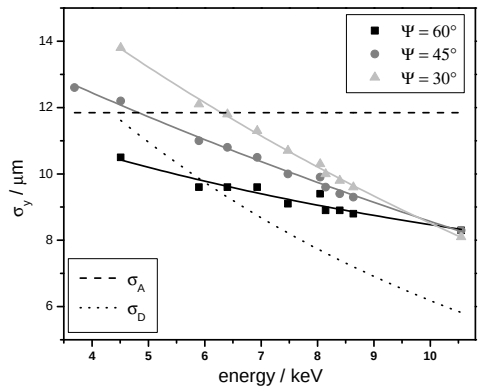

Figure 4.6: Angle-dependency of the width of the probing volume for three different angles Ψ between beam axis and sample normal.

In contrast to the setup at the mySpot beamline there is no angle between detection axis and ring plane, allowing for the use of equation 3.9

$$\sigma_y = \sqrt{\sigma_D^2 \sin^2(\Psi) + \sigma_A^2 \cos^2(\Psi)} \tag{4.5}$$

Using the data with the different angle Ψ, a set of linear equations for σ_y^2 is obtained, resulting in values for σ_A and σ_D as shown in the graph. In this example a spot size of the first lens of $\sigma_A = 11.84$ µm and values for σ_D, which are smaller for the whole energy range, could be calculated. The nominal values for the used lenses are $\sigma_A = 10$ µm and $\sigma_D \approx 7$ µm. While the excitation lens spot size was calculated to be slightly too big, the detection lens spot size is in good agreement with the manufacturers values for energies above 8 keV. For smaller energies, the calculated spot size σ_D shows a trend to bigger values as expected due to the use of the lens in collecting mode, see section 2.2.3. The values cannot be taken as an absolute result, as the error of σ_y is not negligible and a non-optimal alignment hinders the use of equation 4.5. Nevertheless, by way of three simple confocal measurements a measure for the spot sizes of the used lenses is derived.

In figure 4.7 the ellipsoid formed by the overlap of the two optics is depicted. It is clear, that depending on Ψ, the integration over the sample surface changes the width of the probing volume.

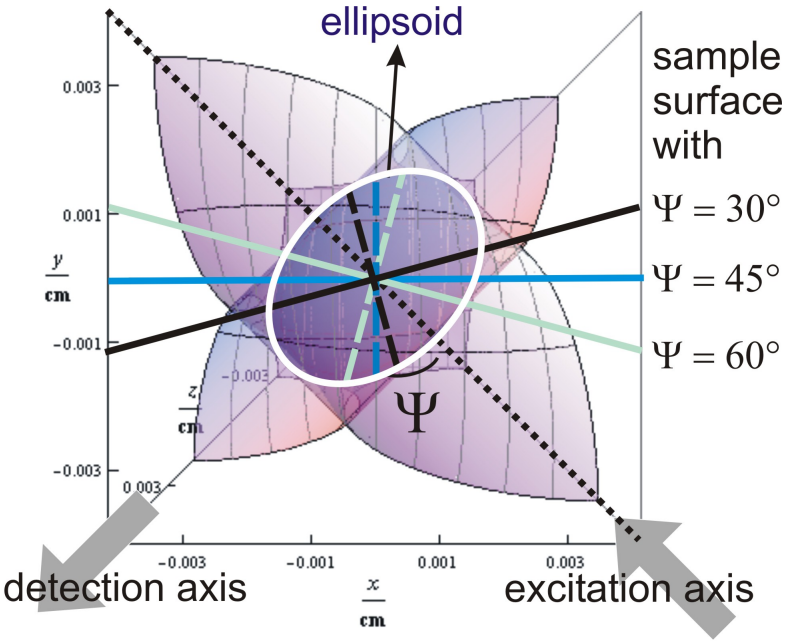

Figure 4.7: Angle-dependency of the width of the probing volume. Depending on the angle Ψ between excitation axis and sample normal, the width of the probing volume changes. For $\Psi = 60°$ depicted in black the width of the probing volume is minimal, it increases for $\Psi = 45°$ (dark grey) and is maximal for $\Psi = 30°$ (light gray). For the lateral resolution the correlation is inverse.

In the case of the values already used in section 3.1 the width of the probing volume is minimal for $\Psi = 60°$ (black lines in figure 4.7), while the lateral spot size on the measurement spot is maximal. The increase in depth resolution for specific angles coincides always with the decrease in lateral resolution. The commonly used value of $\Psi = 45°$ (dark gray lines) is a compromise between lateral spot size and width. For

specific purposes, f.e. if only the depth resolution is of interest, other geometries may yield an advantage. According to equation 3.10 the integral sensitivity is independent on Ψ, see figure 4.8.

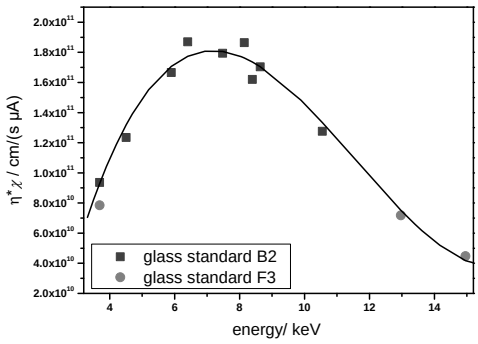

Figure 4.8: The integral sensitivity η is not dependent on the angle Ψ between sample normal and excitation axis.

4.2 Validation

The validation of the analytical model for the reconstruction of the composition and layer thicknesses of stratified samples is a prerequisite for the use of the model for quantification. In the next two sections results are presented for the quantification of thick glass reference samples as well as for stratified polymer samples, as published in [MMS$^+$08].

4.2.1 Glass reference material

As a first test one standard of the Breitländer series was excluded from the calibration procedure and used as validation sample. This standard was quantified according to equation 3.28 with local densities as free parameters in a least square fitting algorithm. For non-detectable elements, the manufacturers' values were implemented as fixed parameters. The integral sensitivity η times χ and the width of the probing volume σ_y were previously obtained by a calibration.

Extensive evaluations were carried out regarding the optimal fitting strategy and program options. Errors due to the fitting routine were tested by varying the initial values of the concentrations. As fitting parameters the local densities were replaced by the concentrations including the overall density of the sample or with a fixed density. Fitting of elemental concentrations of local densities was done directly or in form of oxides.

All depth profiles were fitted equally or the fitting was weighed according to the maximal intensities. As an example, if one major element is present in two successive layers and a trace element is only present in one layer, it is advisable to fit both elements

equally in order to obtain the layer thicknesses. In cases with simple stratified geometry of a sample, weighing might give better results.

For this simple case the fitting of local densities compared to concentrations showed equal results compared to the manufacturers' values. The weighing or the fitting of oxides did not improve the outcome. Deviations proved to be less than 3 % and, thus, negligible compared to the uncertainties caused by the spectral processing mechanism and the inhomogeneity of the reference material.

element	weight percent / %		rel. deviation / %
	reference	quantification	
K	1.8	0.87	52
Ca	0.59	0.30	49
Ti	2.3	2.5	8.7
Cr	0.1	0.023	77
Mn	16	13.6	15
Fe	0.8	0.86	7
Zn	6	5.8	3.3
Ge	0.055	0.058	5.4
Rb	0.037	0.031	16
Sr	0.6	0.79	32
Zr	0.1	0.073	27
Ba	1.8	1.5	15
Th	0.035	0.03	13

Table 4.2: The weight fractions for selected elements as given by the manufacturer, as fitted with the analytical model and their deviations in percent.

Table 4.2 compares the fitted weight fractions for a representative selection of elements as given by the manufacturer and as obtained by the quantification.

All elements are fitted simultaneously. Therefore, errors in the calculation of one element affect all the others. In general, the deviation from the reference values is $\sim$ 20-30%. Due to better statistics, higher concentrations of elements yield smaller errors. The deviations may increase for minor and trace elements as well as for low Z elements.

In the case of the low-Z elements calcium or potassium, the absorption influences the ratio of Kα to Kβ fluorescence with depth. This induces distortions in the intensity profiles. These problems are of particular importance if regions deep inside the specimen are probed.

The considerable deviation of the Chromium values can be explained by the presence of 16 % of manganese. Mn is the following element in the periodic table, i.e. the fluorescence peaks of the two elements are very close. The difference in concentration amounts to two orders of magnitude. The deconvolution of the peaks is therefore difficult, resulting in high uncertainties in the net peak intensity values.

Considering a probing volume of (20 µm)^3 only 30 pg of glass is probed. Thus, inhomogeneities may contribute to the overall error, as well.

4.2.2 Polymer samples

For the validation of the reconstruction algorithm for layered systems, the availability of stratified reference material is essential. Such model systems are required to have layer thicknesses in the region of some 10 µm to meet the spatial resolution of the confocal setup.

Such stratified materials were manufactured and characterized by the analytical chemistry research group at the Leibniz University of Hanover [SMM+09]. As an amorphous organic material, commercially available Keltan-512 was chosen. It consists of EPDM (ethylene propylene diene M-class rubber) with ethylidennorbornen as the diene. One percent of dicumyl peroxide was added as vulcanizing agent. Eleven different matrices were fabricated; five with ZnO, five with SiO_2 as additive and one pure matrix. As nominal concentrations of the additives 2, 4, 6, 8, 10 phr and 6, 12, 18, 24 and 30 phr $SiO_2 \cdot H_2O$ were chosen. The unit phr means parts per hundred of rubber and is used by rubber chemists to depict what amount of certain ingredients are needed.

The matrices were then vulcanized and pressed into thin films with varying thicknesses. Five of these thin films were stacked together to attain 16 stratified samples. Each polymer as well as the layer systems have been characterized by scanning Micro-XRF to analyze the homogeneity of the filler dispersion and by light microscopy to determine the layer thicknesses. The layer thickness of one layer in a stack of five shows deviations of 3 - 10 %, while the Micro-XRF intensity of Zn shows a stability of 3 - 8 % averaging $\sim$ 5000 single measurements in the latter case. Both relative standard deviation values are within the typical range of the applied method. For Micro-XRF, variations of layer thicknesses are the main source for increased deviations of the intensities measured while the highest standard deviation for the thickness measurements by light microscopy was induced by layers with comparable composition, i.e. adjacent layers with additives in different concentrations. In this case, the identification of the boundary between two adjacent layers, which was used to measure the thickness in the stratified samples, was complicated. This led to higher errors ($\sim$ 10 %) in the determination of layer thicknesses of those materials in comparison to the materials with alternating layers with and without additives.

The filler mass share was determined by inductively coupled plasma-optical emission spectroscopy (ICP-OES). A microwave extraction of each rubber mixture was performed in a solution of concentrated nitric acid for ZnO as filler and a solution of concentrated nitric acid and hydrofluoric acid in the case of $SiO_2 \cdot H_2O$ as filler. The analysis was done with the aqueous solutions by ICP-OES using the emission spectral lines with the highest sensitivity at 334.502 nm for zinc and 288.158 nm for silicon.

Fifty-five scans on seven different systems with alternating ZnO concentrations and layer thicknesses between 30 and 130 µm have been performed by 3D Micro-XRF at the mySpot beamline. Weight percent and layer boundaries were the free parameters for the fit algorithm. Density and dark matrix could be calculated from the nominal values. The fit was not sensitive to the initial values of the Zn concentration. The layer boundaries have to be a good guess for a successful reconstruction, otherwise visibly incorrect profiles may be calculated.

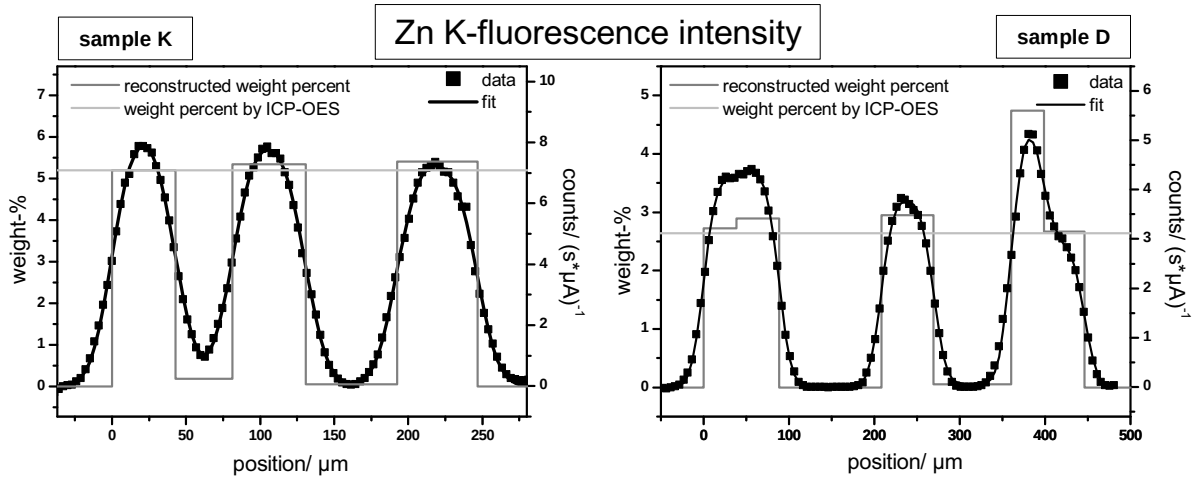

Figure 4.9: Left: Example for reconstruction of composition and layer thickness of sample A: The measured Zn-Kα data in counts/(s µA) (dots) and the fit in counts/(s µA) (black line) with equation 3.35 are depicted as well as the reconstructed weight percent profile in weight percent and the values obtained by ICP-OES measurements for the Zn concentration in layers one, three, and five. Right: Example for Zn concentration variation. In this sample (sample B), a lump of Zn could be detected in the fifth layer.

Two examples of scans on samples K and D, see table 4.4, will be discussed in the following. In figure 4.9 the measured Zn-Kα count rate profiles and the reconstructed weight percent values as a function of thickness for the two polymer systems are shown. Sample K consists of three layers with a nominal ZnO concentration of 8 phr and two layers without any additive in between. In sample D, layers of nominal 4 phr ZnO alternate with 12 phr $SiO_2 \cdot H_2O$.

The scan of sample K (left graph of figure 4.9) is a typical depth profile of the measured series. The weight percent distribution is rectangular shaped, while the experimental data show mainly two distortion effects: absorption of the X-rays inside the sample and the limited spatial resolution of the instrument. The peak intensities representing the high Zn concentration decrease with depth, whereas the respective Zn concentration is constant. The boundaries of the different layers are smoothed by the resolution of the setup, i.e. the convolution of the sharp layer boundaries and the probing volume. The reconstruction shows good agreement for the scan of sample K. The deviation of the fitted values is below 2 % compared to the values obtained by ICP-OES. The precision of the zinc concentrations is excellent; the relative standard deviation derived from all measurements is smaller than 5 %.

In one of the scans of sample D (right graph of figure 4.9) significant variations of the concentration of Zn were observed. As stated previously, $\sim$ 5000 individual intensity values have been used to obtain the average zinc intensities for each polymer system by scanning Micro-XRF. If small lumps of ZnO produce significantly higher intensities at only few measuring points, the total number of averaged data will smooth this effect with respect to the resulting average value. Thus, an inhomogeneous distribution of the filler material will eventually only result in a higher standard deviation of the average intensity. Hence, the result for sample D in figure 4.9 is an example that 3D Micro-XRF is capable of determining changes in the concentration of elements into the depth in the micrometer regime.

The depth profiles at different points among the seven samples investigated in this work were measured with step widths of 3 - 5 µm with live times of 5 s. In table 4.3 the results of the thickness determination of all scans are displayed. As a reference method, thicknesses were determined with a light microscope after the 3D measurements at BESSY. A cross section was prepared in the vicinity of the spots of the 3D scans by slicing the samples with a razor blade. In order to test the homogeneity of the samples, measurements were carried out in an area of $\sim$ 1 mm^2 around the 3D scan spots. The values for the layer thicknesses obtained by light microscopy and by 3D Micro-XRF agree within their standard deviation for all samples. The thicknesses obtained by repeated scans on the same sample scatter with 10 - 15 % for both techniques. As a result, the variation of thicknesses is sufficiently small for this validation. Improvements for the thickness determination should be expected if both measurements were performed at exactly the same position, and a scatter of the values of both methods below 10 % is likely for this case.

The weight percent of Zn obtained by the reconstruction algorithm are displayed in table 4.4. The relative mean standard deviation in all samples is smaller than 5 %. The comparison with the reference value obtained with ICP-OES exhibits a deviation of less than 6 %. The values agree within two times the standard deviation of the measured data. Taking the uncertainties of the calibration into account these results are excellent.

The Zn weight fractions computed for the layers made of pure EPDM vary around zero. However, they can reach values of almost 0.1%. This can be explained by the very nature of a deconvolution procedure with limited resolution. A layer of pure EPDM surrounded by two layers with additives represents a difficulty for a fit procedure, especially when the layer thicknesses are in the scale of the resolution of the setup: the thinner the layer, the higher the uncertainties of the computed weight fractions. The dynamic range of weight fractions, which can be accommodated by this method and this setup, is $\sim$60 (6% Zn for layers one and three, 0.1% Zn for layer 2) for layer thicknesses of 40 µm.

4.3 Discussion of the reconstruction procedure

In this chapter the reconstruction of bulk and stratified material by 3D Micro-XRF has been shown and proved to be a precise quantitative analytical technique. The precision of the composition values was shown to be satisfactory in the case of the glass reference

sample	layer thickness / µm				deviation	
	light microscopy		3D Micro-XRF		/ µm	rel. / %
	98.8	± 4.3	93.0	±10.0	5.8	6.0
A	105.3	±3.2	111.5	±8.0	-6.2	-5.9
6scans	91.3	±8.0	84.2	±7.0	7.1	7.8
2 spots	84.8	±6.8	88.5	±6.0	-3.7	-4.3
	71.8	± 7.7	74.9	±10.7	-3.1	-4.3
	111.5	±5.3	124.6	±5.0	-13.1	-11.7
B	93.2	±7.3	100.4	±4.3	-7.2	-7.7
10 scans	100.0	±3.6	96.7	±3.7	3.3	3.3
2 spots	79.5	±2.3	88.5	±7.6	-9	-11.3
	105.0	±6.2	99.9	±4.5	5.1	4.8
	71.0	±6.0	68.5	±6.1	2.5	3.5
C	50.5	±6.0	55.9	±7.9	-5.4	-10.6
8 scans	70.7	±7.6	69.2	±10.6	1.5	2.2
1 spot	119.3	±8.5	119.5	±8.6	-0.2	-0.1
	73.5	±8.4	70.3	±5.7	3.2	4.3
	90.0	±8.0	86.4	±5.4	3.6	4.0
D	109.5	±6.1	117.8	±4.6	-8.3	-7.5
8 scans	65.8	±5.4	63.2	±2.7	2.6	3.9
1 spot	84.0	±6.2	90.2	±7.1	-6.2	-7.3
	85.2	±2.8	77.4	±10.2	7.8	9.1
	64.8	±3.7	59.3	±4.0	5.5	8.6
E	38.7	±2.8	43.8	±5.0	-5.1	-13.1
9 scans	38.3	±5.9	38.8	±2.5	-0.5	-1.23
2 spots	67.5	±3.6	70.9	±2.9	-3.4	-5.1
	59.5	±4.6	58.6	±1.6	0.9	1.4
	44	±	43.8	±2.4	0.2	0.46
J	46	±	40.2	±2.9	5.8	12.7
6 scans	53	±	53.9	±2.3	-0.9	-1.6
2 spots	39	±	36.4	±4.9	2.6	6.7
	53	±	49.1	±2.7	3.9	7.4
	51.3	±2.3	45.6	±3.4	5.7	11.1
K	36.0	±3.8	38.7	±3.0	-2.7	-7.6
8 scans	47.1	±1.9	48.6	±2.8	-1.5	-3.2
1 spot	57.4	±3.7	63.3	±4.4	-5.9	-10.4
	54.1	±2.2	54.5	±3.2	-0.4	-0.7

Table 4.3: Layer thicknesses of seven samples consisting of 5 layers obtained by light microscopy and 3D Micro-XRF with relative and absolute deviations. As uncertainties the standard deviations of all measurements are listed.

sample	ZnO / phr	Zn concentration / %				deviation / %	
		ICP-OES		3D Micro-XRF		abs.	rel.
	10	6.6	± 0.05	6.87	±0.18	-0.27	-4.01
A	2	1.15	±0.02	1.10	±0.03	0.05	4.10
6scans	10	6.6	±0.05	6.85	±0.18	-0.25	-3.74
2 spots	2	1.15	±0.02	1.11	±0.05	0.04	3.56
	10	6.6	± 0.05	6.57	±0.21	0.03	0.46
	6	4.07	±0.05	4.15	±0.09	-0.08	-1.82
B	4	2.64	±0.04	2.68	±0.09	-0.04	-1.57
10 scans	6	4.07	±0.05	4.23	±0.18	-0.16	-3.77
2 spots	4	2.64	±0.04	2.72	±0.07	-0.08	-2.93
	6	4.07	±0.05	4.12	±0.12	-0.05	-1.26
	8	5.24	±0.04	5.34	±0.11	-0.1	-2.00
C	0	0.02	±0.03	0.07	±0.10	0.05	(244.18)
8 scans	8	5.24	±0.04	5.34	±0.11	-0.10	-1.98
1 spot	0	0.02	±0.03	0.00003	±0.09	0.02	(98.77)
	8	5.24	±0.04	5.23	±0.14	0.01	0.25
	4	2.64	±0.04	2.72	±0.03	-0.08	-3.01
D	(12)	0.02	±0.03	0.004	±0.009	0.02	(76.40)
8 scans	4	2.64	±0.04	2.72	±0.08	-0.08	-3.00
1 spot	(12)	0.02	±0.03	0.007	±0.01	0.01	(65.68)
	4	2.64	±0.04	2.81	±0.12	-0.16	-6.22
	10	6.6	±0.05	6.82	±0.11	-0.22	-3.3
E	2	1.15	±0.02	1.19	±0.06	-0.05	-4.22
9 scans	10	6.6	±0.05	6.81	±0.10	-0.21	-3.11
2 spots	2	1.15	±0.02	1.1	±0.05	0.05	4.18
	10	6.6	±0.05	6.72	±0.19	-0.12	-1.82
	6	4.07	±0.05	4.22	±0.20	-0.14	-3.50
J	4	2.64	±0.04	2.76	±0.10	-0.12	-4.56
6 scans	6	4.07	±0.05	4.27	±0.13	-0.20	-4.92
2 spots	4	2.64	±0.04	2.82	±0.11	-0.18	-6.70
	6	4.07	±0.05	4.09	±0.06	-0.01	-0.33
	8	5.24	±0.04	5.16	±0.12	0.08	1.51
K	0	0.02	±0.03	0.12	±0.07	0.10	(479.47)
8 scans	8	5.24	±0.04	5.29	±0.19	-0.05	-0.88
1 spot	0	0.02	±0.03	0.03	±0.01	-0.01	(-29.85)
	8	5.24	±0.04	5.17	±0.19	0.07	1.34

Table 4.4: Zn concentration of seven samples consisting of 5 layers. ICP-OES values, 3D Micro-XRF values and relative and absolute deviations. Values in brackets denote the deviations of layers with nominal 0 % ZnO.

material (in general $20 - 30$ %) and excellent in the case of stratified polymer samples (Zn concentration ≈ 5 %, layer thickness < 15 %). In the following some characteristics of the method and the reconstruction procedure will be discussed.

The overall detected intensity of a confocal measurement is lower than when using Micro-XRF. Due to the restricted probing volume, the investigated mass is small. One may consider this as a measurement of a layer with a thickness of $\sim$ 20 µm. In addition, the solid angle of detection is limited by the acceptance of the capillary lens in front of the detector. Finally, the transmission of these lenses usually is below 20 %.

A quantitative reconstruction algorithm is used for the determination of the weight fractions. Mathematically, the main procedure for the reconstruction is a deconvolution. The depth profiles of all visible elements are fitted simultaneously. Errors in the determination of one fit parameter will affect all others. When taking another look at the analytical model (equation 3.35) we find numerous sources for errors:

$$\begin{aligned}\Phi(y) &= \frac{\Phi_0 \eta \sigma_F}{2} \sum_k \rho_{i,k} \left[\prod_{j=1}^{k-1} e^{-\bar{\mu}_{lin,j}(d_j - d_{j-1})} \right] e^{-\bar{\mu}_{lin,k}(y - d_{k-1})} e^{\frac{(\bar{\mu}_{lin,k}\sigma_y)^2}{2}} \times \\ &\times \left[erf\left(\frac{d_k + \bar{\mu}_{lin,k}\sigma_y^2 - x}{\sqrt{2}\sigma_y} \right) - erf\left(\frac{d_{k-1} + \bar{\mu}_{lin,k}\sigma_y^2 - x}{\sqrt{2}\sigma_y} \right) \right] \end{aligned} \quad (4.6)$$

1. Φ_0: The knowledge of the excitation intensity relies in the measurements on the use of a calibrated ionization chamber, which can be considered precise.

2. σ_F: The fluorescence production cross section is as precise as the used fundamental parameter data base. A compilation based on data collected by Elam et al.[ERS02] is used throughout this work.

3. η and σ_y: The calibration parameters show uncertainties in the range of 10 - 15 % mainly due to inhomogeneities of the used reference standards.

4. $\bar{\mu}_{lin}$: The error of the effective linear mass absorption coefficient, see equation 2.34, is composed of the error of the determination of the excitation and detection angles, the error of the mass attenuation coefficients, the error of the density of the sample and the error in the weight percent of the elements.

5. d_k and ρ_i: The two fit parameters are dependent on the initial values supplied for the fit. The complexity of the analyzed sample and its density complicate the reconstruction. Errors in the layer thickness directly influence the validity of the computed local densities of following layers.

The two presented examples in this chapter already illustrate the last statement. The reconstruction is excellent in the case of the polymer samples. The samples have a low density and therefore small absorption effects. The Zn Kα radiation can be collected throughout the whole samples. Only one element is fitted, which simplifies the deconvolution considerably. In case of the glass reference samples fluorescence could be obtained

only as far as penetration and information depth reached for the different fluorescence energies. The simultaneous fitting of thirteen elements made the fitting more time-consuming. More complex systems introduce higher uncertainties in the reconstruction process.

Real experimental samples are far more complicated than these two reference samples. They may not exhibit a layered structure with sharp boundaries, many elements might be present, the density of the sample may lead to total absorption of one element, thus making a reconstruction in deeper parts impossible.

Initial values for the local densities do not influence the reconstruction considerably. Only for trace elements in complex systems uncertainties of up to 50 % may be encountered. The number of layers and the initial values for the layer boundaries on the other hand are parameters, which must be chosen carefully, especially as errors in layer thickness directly influence the calculated transmission of the considered layer. As a control for these parameters the fit can be judged visibly. The computed data must fit to the measured data, but additional plausibility criteria can be taken into account. For example, negative values must be excluded or thicknesses must not be considerably smaller than the resolution of the setup. Each sample must be treated individually regarding fitting procedure and evaluation of results. Just computing the χ^2-value of the least square algorithm is therefore not sufficient, but monitoring the fitting procedure is mandatory. This renders the quantification of 3D Micro-XRF depth scans into a labor-intensive task, which needs human supervision.

In order to meet the needs of a variety of samples, following fitting routine options could be used:

- Local densities or concentrations can be fitted.
- Layer boundaries may be fixed or fitted.
- The overall density may be fixed or an additional fitting parameter (fluorescence or scattering).
- The dark matrix composition derived through additional measurements can be implemented as fixed values or it can be calculated after each iteration, if the exact stoichiometry of the layer is known (f.e. Oxides).
- The depth profiles can be weighed according to their intensity, or all elements can be fitted with equal weight.
- The fitting of minor and major elements can be done as a sequence in order to derive layer boundaries which are not so obvious through visual examination.

Best results are obtained when a flexible fitting strategy is applied adjusted to the object at hand. The algorithm works the more stable the fewer fitting parameters are used. Thus, successively fitting different parameters has proved to be useful. Following fitting options are implemented with ρ_k the total density of layer k, d_k its layer boundaries and $w_{i,k}$, $\rho_{i,k}$ the weight percent and local density of element i in layer k, respectively:

	fitted parameters	fitted profiles	layer boundaries	fixed matrix	density
0	d_k	fluorescence or scatter	fitted	dark or total	fixed or fitted
1	ρ_k	scatter	fixed	total	-
2	$\rho_k + d_k$	scatter	fitted	total	-
3	$w_{i,k}$	fluorescence	fixed	dark	fixed
4	$w_{i,k} + d_k$	fluorescence	fitted	dark	fixed
5	$w_{i,k} + d_k + \rho_k$	fluorescence	fitted	dark	fitted
6	$w_{i,k} + d_k + \rho_k$	fluorescence + scatter	fitted	dark	fitted
7	$\rho_{i,k}$	fluorescence	fixed	dark	fixed
8	$\rho_{i,k} + d_k$	fluorescence	fitted	dark	fixed
9	$\rho_{i,k} + d_k + \rho_k$	fluorescence	fitted	dark	fitted
10	$\rho_{i,k} + d_k + \rho_k$	fluorescence + scatter	fitted	dark	fitted

Table 4.5: Fitting option implemented in the computation program.

Table 4.5 must be read as follows. Fitting option 2 means, that the Compton and Rayleigh depth profiles of a scan are fitted with layer densities and boundaries as fitting parameters. Concentrations of all elements must be given in advance as fixed values. Fluorescence and scatter profiles are fitted in option 10 with local densities, layer densities and boundaries as fitting parameters. Only the local densities of the dark matrix elements must be known. Fitting options can be interactively employed by the user, and thus, optimally adapted to the investigated sample. If for example only trace elements of a sample can be measured by 3D Micro-XRF and the dark matrix is well characterized as for parchment samples, a fitting strategy can be the fitting of density and layer boundaries (option no. 2) with the known dark matrix composition and then fitting the elements as local densities (option no. 7). This strategy is not feasible for samples with less dark matrix, where a combination of fitting option 4, 5 and 6 may be practicable.

In comparison to Micro-XRF, the quantification is more laborious and the results are less accurate. Nevertheless, 3D Micro-XRF as a tool for the investigation of stratified materials is an alternative, if sectioning of the sample has serious disadvantages or nondestructive characterization is the only option. For many scientific issues from art and archeology, geology, biology, or materials science, relative concentration profiles or quantitative analysis with lower precision provides valuable and important information.

Application example: car paint

The investigation of car paint is a good example for the possibilities as well as limitations provided by the quantification program as the layered structure is well characterized and the layers have sharp boundaries. Figure 4.10 shows a light microscope picture of a cross section of a red paint, embedded in an epoxy resin. The different paint layers are clearly distinguishable.

The first layer **(1.)** is a clearcoat which is composed mainly of acrylates, i.e. no fluorescence can be detected with 3D Micro-XRF. The second layer **(2.)** is the basecoat

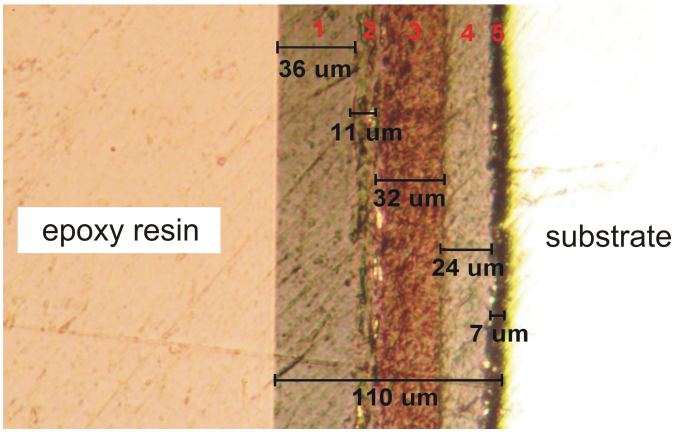

Figure 4.10: Light microscope picture of a cross section of a red paint with 200 times magnification. The different paint layers are clearly distinguishable.

layer with the color-giving constituents. A primer layer **(3.)** made of a polyester matrix with additives like $BaSO_4$ and TiO_2 follows. Next is a epoxy resin coat **(4.)** followed by a zinc coating **(5.)**. The substrate is steel mainly made of Fe.

This layered structure can be seen in the depth profile of this sample, also, see figure 4.11. The scattering profiles are very important in this example, as the first layer cannot be discerned by fluorescence measurements. Without the knowledge of the thickness and density of this layer, the reconstruction of all following layers can only be incorrect due to incorrect absorption correction. In this case, the fitting strategy employed was first the fitting of the scattering profiles in order to obtain the layer boundaries (option 0) and the subsequent fitting of the fluorescence profiles with option 7 in order to obtain the local densities of the elements. The fitting of local densities was feasible because the dark matrix and density of the layers is well characterized.

Figure 4.12 shows the reconstructed weight percent values of two different car paints, the red paint in the left graph and a blue paint for comparison in the right graph. In case of the quantification of the car paint samples it is only meaningful to reconstruct the composition of layers 1 through 4. The zinc coating with a density of 7.14 g/cm^3 does not allow reliable quantification because of the high absorption of radiation. Layers 5 and 6 are only displayed for the sake of completeness. In section 4.2.2 the dynamic range proved to be 60 in case of 40 µm thick layers. Here, the dynamic range is smaller due to the smaller thicknesses. This is the reason for the big uncertainties of f.e. Zn in layer 4 and Ba in layer 2. Values must be understood as semiquantitative. The comparison of the two paints shows that the layered structure is very similar in both cases, with the main difference being the presence of Ti in the blue paint. The coloring elements are Cu and Fe for the blue and the red paint, respectively.

Table 4.6 shows the reconstructed layer thicknesses obtained by 3D Micro-XRF as well as the values obtained by light microscopy, see figure 4.10. The first layers show deviations as expected. The deviations increase with increasing depth. In this case this has two different reasons. Errors in the dark matrix which was provided by the

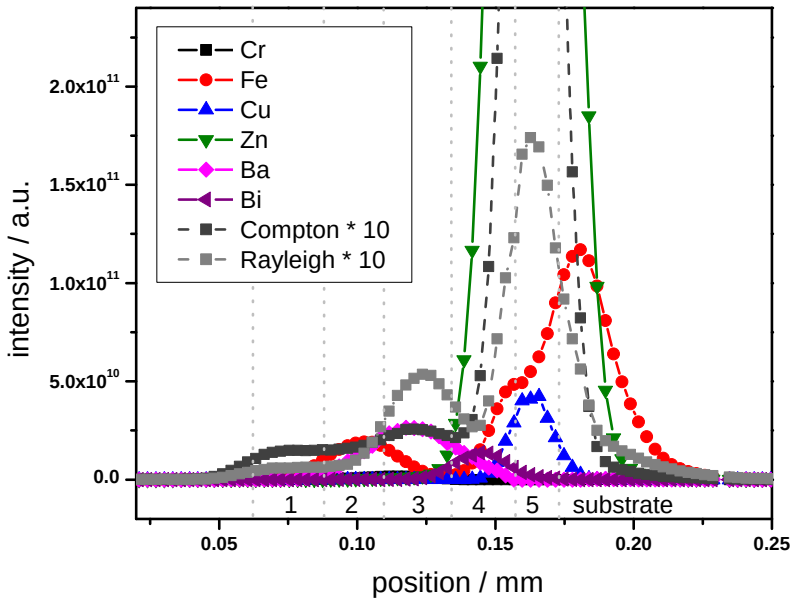

Figure 4.11: 3D Micro-XRF scan of the red paint sample of figure 4.10. The dotted gray lines symbolize the layer boundaries qualitatively.

manufacturer add up when reconstructing deeper layers. Additionally the difference in detected overall fluorescence intensity between layers 3 and 4 is more than 1 order of magnitude, which limits the dynamic range.

This example proves the possibility to reconstruct the composition and thickness of layered structures with as many as 5 layers without sectioning. The results are semi-quantitative due to the presence of an elemental Zn-layer which complicates reconstruction due to high absorption and dynamic range problems. The additional analysis of scattered radiation should in any case be included in the fitting routine, especially when dealing with samples with possible layers without fluorescence elements as the clearcoat layer (layer 1) in this example.

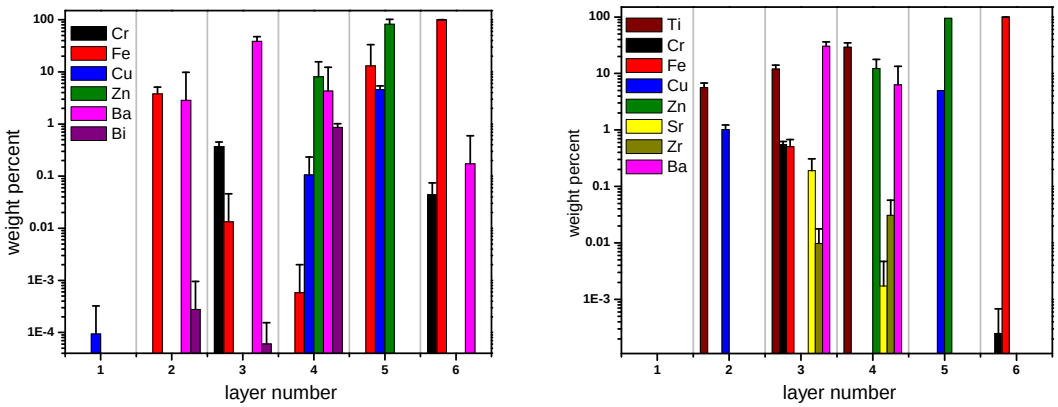

Figure 4.12: Left: Reconstruction of the weight percent values of the scan of figure 4.11. Right: For comparison a reconstruction of a blue car paint is shown.

no of layer	thickness / µm		deviation / %
	light microscopy	3D Micro-XRF	
1	36	36	0
2	11	13	16
3	32	22	32
4	24	31	28
5	7	5	26

Table 4.6: Layer thickness values obtained by light microscopy and 3D Micro-XRF.

5 Application examples

This chapter deals with the use of quantitative 3D Micro-XRF for archaeometric applications. Archaeometry is the application of scientific techniques and methodologies to archaeological objects. Due to their value, many cultural heritage samples have to be analyzed non-destructively. Thus, X-ray techniques have proved to be useful tools for the elemental analysis and characterization of many different kinds of samples, like paintings[CCB+04, FRJ+02, DJS+08, KvBM00], metals [GC98] or manuscripts [HMKB04], even leading to specialized spectrometers [BRB+01]. The possibility of depth resolved measurements by 3D Micro-XRF is in this context especially interesting because sampling, sectioning or preparation of the object is not necessary.

3D Micro-XRF as any analytical technique has its advantages and limitations. In the following three sections it becomes apparent, that a combination of methods is always the best way to deal with a real analytical question. In the first presented example, it was possible through additional Micro-XRF measurements to make corrosion phenomena in a historical art object visible. Micro-XRF was in this case used in order to extend the range of detectable elements. In the second application example, 3D Micro-XRF measurements on parchment proved to give essential insights into the variations of composition and density inside the samples. With this gained knowledge, measurement strategies involving Micro-XRF were developed. The last investigation concerning a glass object from the 14th century highlights the capabilities of 3D Micro-XRF with X-ray tube excitation. A specific art historical question could be answered without the need for a full quantification.

5.1 Reverse paintings on glass

The objective of the first presented study was to gain insight into aging and corrosion processes in historical glass artifacts. Within a collaboration with the group of Dr. Oliver Hahn of the Federal Institute for Materials Research and Testing (BAM) we had the opportunity to investigate a reverse-glass painting of the virgin Mary from the 19th century. Results of this work have been published in [KMM+08].

In contrast to stained glass the paint of reverse-glass paintings is applied onto the smooth surface without successive firing. It is applied from the backside with the intension to view the painting through the glass. This has the effect of intense and shining colors. Popular during the 15th and 16th century, reverse-glass paintings were replaced in the 19th century by cheaper colored prints.

The low adhesion between oil- or resin-containing colors and the glass is one of the causes for degradation phenomena in reverse-glass paintings. Especially in addition with glass corrosion the objects are in danger to loose their decoration. This mechanisms of

'loss of adhesion' is connected to the formation of a depletion layer between paint and glass.

The investigated object shows serious damage phenomena like the delamination of the paint, resulting in parts in the total loss of the decoration. 3D Micro-XRF was used in this application as a means for the destruction-free investigation of potential corrosion layers between paint and glass. Depth profiles of mobile elements, such as K or Ca, are particularly of interest as a proof of corrosion.

Prior to the investigation with 3D Micro-XRF the glass matrix was characterized with the Micro-XRF spectrometer described in section 2.4.1. Table 5.1 shows the quantification values for the glass matrix, which proved to be potash glass. The concentration values have uncertainties of about 10 %, oxygen, sodium, magnesium and aluminum constitute the dark matrix for Micro-XRF and their concentration values have been obtained through a previous SEM-EDX investigation.

element	concentration / %	element	concentration / %
O	44.5	Si	31.6
Na	0.73	P	0.24
Mg	0.25	Cl	0.33
Al	1.13		

Table 5.1: Concentration values for non-detectable elements with 3D Micro-XRF obtained by Micro-XRF. The values for oxygen, sodium, magnesium and aluminum have been obtained through a previous SEM-EDX investigation.

The 3D Micro-XRF measurements were performed at the mySpot beamline, see section 2.4.2. The calibration with an excitation energy of 19 keV of figure 4.4 was used, thus, with a FWHM of about 23 µm at 10 keV. The object was measured from the painted side. Four depth scans on spots without paint, i.e. where the paint had already lost its adhesion, two scans on blue paint and one scan on brown paint were conducted with live times of 600 s per spectrum and step widths of 4 - 5 µm.

Figure 5.1 shows the net peak depth profiles of a group of selected elements of one glass scan (left) and one scan on blue paint (right). The points are the measured net peak intensities and the solid lines correspond to the intensities computed with the quantitative fit.

For the fit of the scan on the glass, the object was assumed to have two layers, a thin corrosion layer and the bulk. The density of the glass bulk was known to be ≈ 2 g/cm^3, so the Micro-XRF values were multiplied with this density and implemented as dark matrix. The layer boundaries and the local densities of the elements were the fit parameters (option 8 in table 4.5). The resulting overall density of the sample was composed of the density of the dark matrix plus the density of the fitted elements. The fit of the concentrations was implemented as fitting of Oxides, that is, in each iteration the oxygen concentration was modified according to the modified elemental composition.

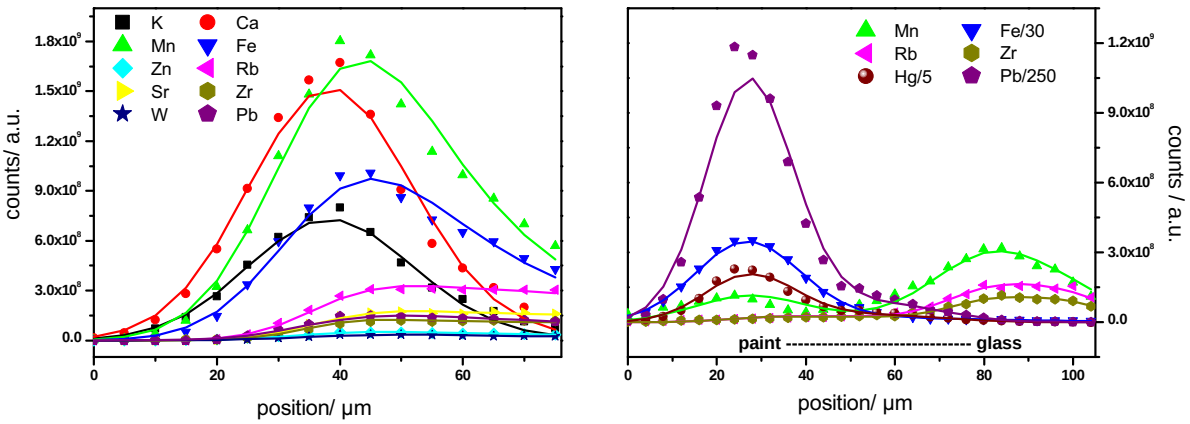

Figure 5.1: Left: Intensity depth profiles of the elements in the glass without any paint layer. Right: Intensity depth profiles of the elements in a blue paint layer and in the glass. The solid lines represent in both graphs the corresponding fits of the reconstruction algorithm. In order to depict the intensity profiles of Pb, Hg and Fe in the same graph they have been divided by the factors 250, 5 and 30, respectively.

The best fit to the data was obtained by assuming a diffusion layer on the surface of the glass of around 5 - 10 µm followed by the bulk glass. In this layer the local densities of all non-matrix elements are significantly smaller than in the bulk glass. The uncertainty of the results for the elemental concentration of the bulk glass due to the absorption from this layer are thus negligible. The concentrations of the glass bulk as well as its density are presented in the right column of table 5.2.

The analysis of the scan on the blue spot (right graph in figure 5.1) indicated a three layer system, composed of paint layer, diffusion layer and glass matrix. The presence of Fe, Pb, Hg and traces of Cd in the paint layer suggested the presence of Berlin Blue, Lead White, Cinnabar and Cadmium Yellow, respectively. As binding media poppy-seed oil was assumed, which consists of stearic acid, oleic acid, linoleic acid and glycerin. With this qualitative information the dark matrix could be assumed as the poppy-seed oil and the well known composition of the four paint colors (see table 5.3) could be included in the fitting procedure of the paint layer. The elements of this layer were fitted as local densities also, so that the density could be derived from the sum of all local densities. For the initial concentration values of the diffusion layer and glass layer the reconstructed values of the glass scans were used.

The best fit to the measured values of all elements was obtained by assuming following layers: a paint layer of around 7 µm, a diffusion layer of around 50 µm, and the 'pure'

	concentration / %		
	scan on blue spot		glass scan
element	blue paint	corrosion layer	glass bulk
K	0.8	0.9	9
Ca	0.9	5	12
Ti	-	-	0.04
Mn	0.06	0.07	0.7
Fe	4	1	0.3
Ni	0.03	0.01	5×10^{-4}
Zn	0.02	0.01	0.006
Rb	0.001	0.008	0.04
Sr	3×10^{-4}	6×10^{-4}	0.03
Zr	0.002	0.006	0.01
Cd	0.5	-	-
Ba	0.3	0.04	0.1
W	-	-	0.009
Hg	0.2	0.07	-
Pb	53	8	0.04
Density/ g/cm^3	5.8	1.8	2.2

Table 5.2: Weight percent values for two layers of a depth scan on a blue paint spot and glass matrix values obtained through four scans on pure glass spots.

color	chemical formula
Lead White	$2\ PbCO_3{\cdot}Pb(OH)_2$
Berlin Blue	$Fe_4[Fe(CN)_6]_3$
Cinnabar	HgS
Cadmium Yellow	CdS
poppy-seed oil	$C_{17}H_{35}COOH + C_{17}H_{33}COOH + 7 \cdot C_{17}H_{31}COOH + C_3H_5(OH)_3$

Table 5.3: Chemical formula of paint colors and binding media in the paint layer

glass bulk. The weight percent distribution of the six elements depicted in the left graph of figure 5.1 is presented in figure 5.2. The presentation as a bar graph gives an impression of the principal weight percent distribution in the three assumed layers, but it does not reflect eventual variations inside these layers. The concentration of all elements measured in layers one and two are given in table 5.2 (blue paint, corrosion layer). Additionally, the overall densities of the layers are displayed.

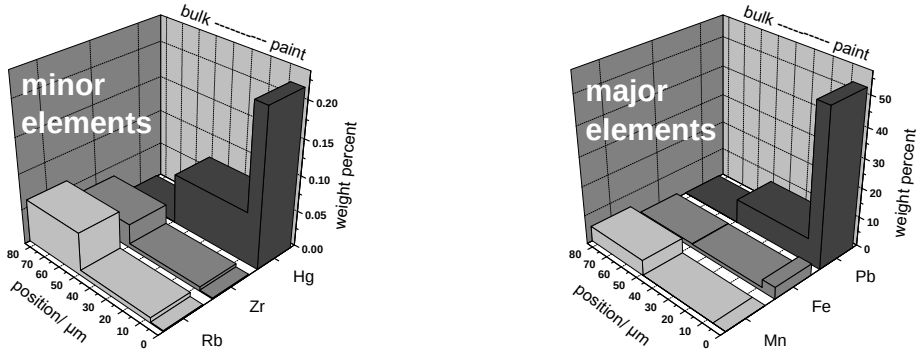

Figure 5.2: Reconstructed weight percent distribution of the elements Mn, Fe, Rb, Zr, Hg and Pb corresponding to the intensity depth profiles depicted in the right graph of figure 5.1.

Uncertainties for the composition in table 5.2 range between 8 % for elements with higher fluorescence energies up to 25 % for elements with lower fluorescence energy like Mn. Elements with fluorescence energies lower than 5 keV show a spread of up to one order of magnitude. A more precise indication of errors is not reasonable as the composition of the glass bulk varies strongly. The indicated error values serve as estimates and are derived from the statistical spread of values of one scan reconstructed with different initial values as well as from the statistical spread between the four scans.

Further on, the obtained results for the glass bulk of the scan on the blue spot are not shown in table 5.2. The reason is the strong absorption due to the high density of this layer which causes high errors for the calculated values. The strong absorption effect is demonstrated in figure 5.3. Here, the calculated intensity ratios of the respective fluorescence radiation from the bulk glass undergoing either the absorption of the blue paint layer or the absorption of the blue paint layer and the corrosion layer is compared to the fluorescence radiation without any absorption. The connecting line between the points is for guiding the eye, only. As can be seen from the graph, even for Zr the intensity ratio is not higher than 0.45 with respect to the absorption of both layers.

This leads to the trend, that uncertainties increase considerably with decreasing fluorescence energy. For example, when comparing the reconstructed glass bulk values for strontium (Sr Kα fluorescence line at 14.014 keV), the values have a deviation of only 23 %, while the deviation for manganese (Mn Kα fluorescence line at 5.894 keV)

is higher than 600 %. Hence, for comparison of the elemental concentration in the blue paint layer, in the corrosion layer, and in the bulk glass the data of the four scans on the 'pure' bulk glass were taken into consideration.

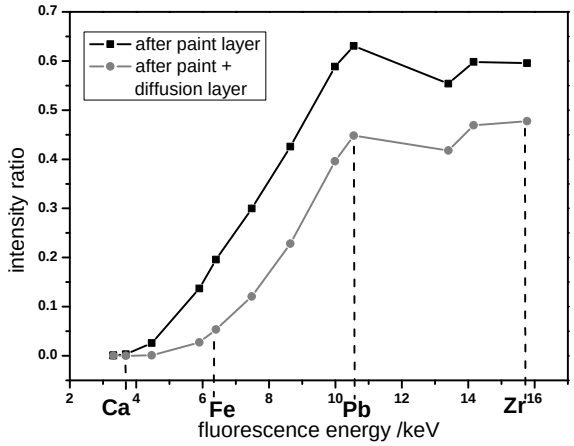

Figure 5.3: Calculated intensity ratios of the respective fluorescence radiation from the bulk glass undergoing either the absorption of the blue paint layer (black squares) or the absorption of the blue paint layer and the corrosion layer (red dots) compared to the fluorescence radiation without any absorption. The connecting line between the points is for guiding the eye, only.

The results concerning the art historical questions can be summarized as follows. The main coloring constituent in the blue color is Berlin Blue and the ratio of Berlin Blue to Lead White is about 1 : 5. Further on, a comparison to the intensity profiles obtained from the 'pure' glass shows that Pb and Hg must have migrated into the glass. The glass bulk contains only a small amount of Pb and no Hg at all. This is supported by the weight percent distribution of the two elements in figure 5.2. Their weight percent in the corrosion layer is significantly different to the one in the glass bulk. On the other hand, the weight percent distribution of Mn, Rb, and Zr clearly shows that depletion in the diffusion layer has taken place. Also for Fe, enrichment in the corrosion seems to have taken place. However, the evaluation for Fe is more complicated as it occurs in both layers, in the paint layer as well as in the bulk glass. Therefore, a reliable conclusion for the corrosion layer can not be drawn in this case.

In general, the quantification for these kinds of objects is a difficult task due to their inhomogeneity. This is even more complicated when strong absorption occurs. In the case of the investigated reverse-glass painting, the lead white in the paint layer is one main reason for the strong absorption effects. Therefore, it is a good test object for the usefulness of 3D Micro-XRF for archaeometric investigations as lead white can be found in almost every painting. In view of these obstacles the results of our reconstruction algorithm should be regarded as semi-quantitative, only. The same holds for the recon-

structed thickness values, because the algorithm was developed for real layered systems without taking concentration gradients into account. Hence, the thickness for the diffusion layers has to be considered as an indication for its order of magnitude. Nevertheless, the results are significant enough to draw conclusions on the corrosion mechanisms.

It is well known, that Rb and Sr are part of the glass matrix, just like K and Ca. Although there are differences in the chemical properties of these elements, they react similar because they belong to the same chemical groups. One may conclude from the diffusion of Rb and Sr, that K and Ca were subject to a diffusion process as well, even if they could not be measured directly. Assuming that an acidic material was used as binding media in this object, we suppose that a corrosion process beginning at the glass/binding media was initiated.[1] The changes in elemental concentrations confirm our assumption.

Lead and mercury ions have migrated into the glass matrix originating from the paint layer (Lead White and Cinnabar dispersed in oil) whereas lighter elements such as manganese decrease in the corrosion zone. The depth profile of lead and mercury within the glass reflects the dissemination of the corrosion process. Here, the dissemination of mercury is more remarkable than the one of lead, because of the insolubility of the Cinnabar pigment.

Summary

In this case study, 3D Micro-XRF spectroscopy was used in order to investigate corrosion processes at the interface paint/glass of a historical reverse painting on glass. Without sectioning or sampling of the object it was possible to reconstruct the elemental composition of the object into the depth of the sample. Although the analysis must be considered semi-quantitative, the art-historian question could clearly be answered. In this particular object, a corrosion layer has formed between glass and paint with altered elemental composition, due to diffusion processes from the paint into the glass. Additionally, for the first time it was shown that 3D Micro-XRF analysis is a well suited tool for archaeometric investigations due to its non-destructiveness and the fact, that no similar reference samples are mandatory.

[1] It is well known, that for non-covered glass surfaces an alkali-depletion within the glass matrix can initiate a corrosion process. The depletion is usually correlated with a formation of 'gel layers', which is due to action of acid hydrolysis.

5.2 Dead Sea Scrolls

In the last section the quantification of 3D Micro-XRF measurements was presented. In combination with Micro-XRF the detectable range of elements was extended in order to gain information about the dark matrix. For the investigation of the next application example, additional information was derived through the analysis of the scattered radiation of the 3D Micro-XRF measurements. This addition to the analysis strategy gives insights into the density variations of inhomogeneous samples as well as an impression for possible dark matrix changes.

An international research campaign on the investigation of the Dead Sea Scrolls was launched a couple of years ago, initiated by Ira Rabin (Jewish National and University Library, Jerusalem, Israel and BAM). Different research facilities are involved using various experimental techniques in order to answer a variety of archaeological questions [HWK+07].

The Dead Sea Scrolls are a collection of hand-written manuscripts found in the North West corner of the Dead Sea, in caves close to the archaeological site Qumran, and are dated to 2nd B.C.E. to 68 C.E. Fragments of more than 800 papyrus and parchment scrolls were found in caves in diverse states of degradation. A few scrolls were found in an excellent preservation state in clay jugs. Most findings were small fragments, though, found on the floor of the caves, some in puddles of water. Today, most fragments are highly degraded and, thus, inhomogeneous laterally as well as into the depth. The degradation has many different causes, e.g. their age, the storage conditions, possibly damaging restoration treatment a.s.o.. The diversity of parchment, papyrus, ink types and scripture suggests, that this collection was not manufactured in the same place and/or time.

The question of provenance and origin is therefore one of the main objectives of scientists involved in the investigation of the Qumran scrolls. In the area around the Dead Sea the water and consequently the air, the surrounding rock a.s.o have a remarkably high content of Bromine, which is characteristic for this specific area. This fact renders the differentiation of parchment which was manufactured with water from that area from parchment from other places possible. Especially the Chlorine to Bromine ratio has already been used for classification [HWK+07].

The archaeological goal of the work conducted with 3D Micro-XRF was to develop an analysis strategy, which enables classification of parchment according to provenance and manufacturing. Additionally, the investigation of the used ink was believed to give insight into these important cultural heritage objects.

5.2.1 Qualitative analysis

Parchment samples have a relatively small density and thickness. The small density implies that absorption effects play a minor role in contrast to f.e. metal samples. Information obtained by Micro-XRF is the integrated fluorescence from the whole information depth. In case of thin samples most elements can be detected throughout the whole sample. These two facts make it feasible to obtain valuable information from

XRF measurements even without quantification. The following section deals with purely qualitative results.

Samples

Two kinds of fragments were provided. On the one hand a collection of about 100 samples were available. This so-called Ronald-Reed collection consists of parchment pieces from caves of the Qumran settlement, from excavation sites close by (Nahal Hever) and reference samples from sites further away from the Dead Sea (Murabba'at). The collection provides an excellent overview over all kinds of parchment found at Qumran. Additionally it allows the comparison of Qumran pieces to similarly old parchment pieces from places close by. None of the fragments was subject to restoration procedures, thus, excluding alteration of the fragment due to recent treatment.

Additionally, the opportunity to investigate some selected fragments from important scrolls with ink was rendered possible. One fragment of the Tempel Scroll, one of the Thanksgiving Scroll and two of the Scroll of Genesis Apocryphon were examined.

All investigated fragments consist of parchment, which is a thin material made from goat skin. Parchment is distinct from leather as it is not tanned, but stretched, scraped, and dried under tension, creating a stiff white, yellowish or translucent animal skin. Chemically it consists mainly of collagen. Collagen is a macromolecule composed of glycine, proline and hydroxyproline. Hence, the chemical formula can be assumed to be $C_2H_5NOC_5H_9NOC_5H_{10}NO_2$. Typical densities of ancient parchment range between 1.4 and 2 g/cm^3 [FMBC00].

Measurements

All Micro-XRF measurements were performed by Timo Wolff with the spectrometer presented in section 2.4.1. Figure 5.4 shows the concentration values of one line scan on fragment 4Q11 (denoting sample 11 of cave 4) and one scan on a piece of the Thanksgiving Scroll. All elements, which can be measured with 3D Micro-XRF are minor or trace elements, the dark matrix constitutes more than 98 % of the sample. The inhomogeneity of the fragments is clearly visible.

Three-dimensional measurements were mostly carried out at the mySpot beamline (4 - 5 beamtimes: Jan07 - April08), see section 2.4.2. Additionally, selected fragments have been examined with the compact laboratory 3D Micro-XRF setup at the TU Berlin, described in the same section.

Altogether 114 scans on 18 samples within 5 beamtimes were examined. Tables 5.4 and 5.5 list all measurements on the investigated samples, with the number of scans, the scan parameters and some qualitative information on the analysis. Main elements are Ca, Fe, Sr and Br. While Br seems to be homogeneous in all samples, other elements are enhanced at the surfaces. Figure 5.5 shows the typical depth profiles of a scan on the fragment 4Q13. Layers with enhanced concentrations of especially Fe and Ca can be distinguished. The profiles are not absorption-corrected, thus, the enhancement may be equally pronounced on both surfaces. In almost all investigated samples this

sample	beamtime	no of scans	live time / s	step width / µm	debris layers?	notes	Br net peak intensity/ $\cdot 10^8$
A43	11.07	3	100	10	no	thin, much Br	25 - 30
A44	11.07	5	100	10	?	much damage, no analysis possible	≈2
AF132	10.07	7	50	10	yes	much damage!, thick	5 - 350
AF151	10.07	4	25	10	yes	thick, Br hom.	15
	11.07	4	100	10	yes	thick, Br hom.	10
M1	01.07	2	500	10	yes		0.2
	03.07	4	250	7 - 8	yes		0.5 - 0.7
	04.08	1	250	10	yes	8 keV	-
M4	11.07	1	150	10	yes		3
M9	11.07	2	150	10	yes		1.5
IQ04	03.07	6	250	17	yes	treated and untreated	5 - 8
IQ10	01.07	4	500	15	yes		1 - 1.2
	03.07	4	250	10	yes	much Fe	7 - 10
4Q2	11.07	4	100	10	yes	thick	3 - 5
4Q11	11.07	2	100	10	yes	damaged	4
	04.08	3	100	10	yes	19 keV	5 - 6
	04.08	3	100	10	yes	8 keV	-
4Q12	01.07	4	475	10	yes		0.6 - 1.2
4Q13	11.07	4	100	10	yes		5 - 6
4Q28	01.07	4	500	15	?	no analysis possible	-
	03.07	4	250	15	yes	much Br, very inhom.	4 - 6
Q5	10.07	4	50	5	yes	much Br, thick	80 - 95

Table 5.4: 3D Micro-XRF measurements at the Berlin synchrotron BESSY II, 79 scans during five beamtimes on different spots of 14 samples of the Ronald-Reed collection were performed.

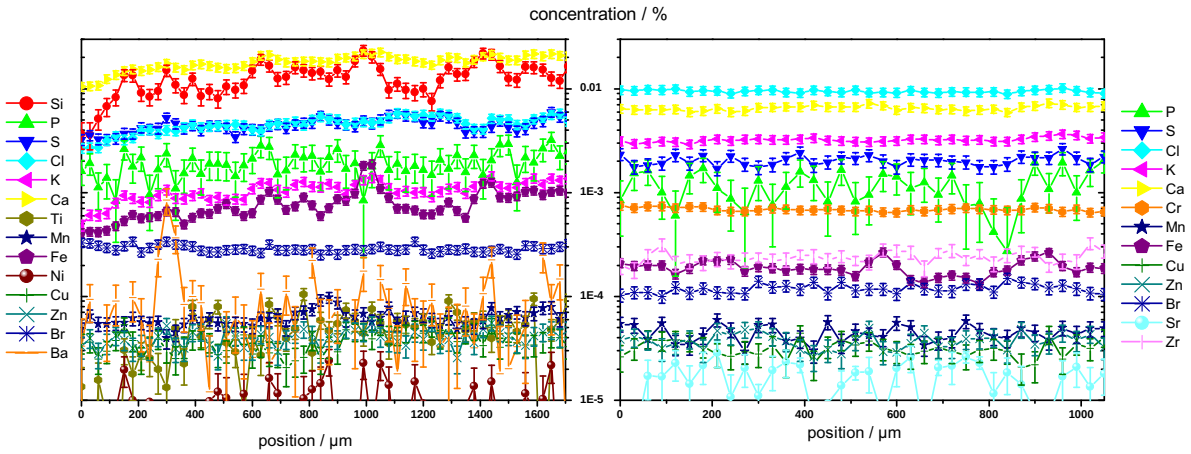

Figure 5.4: Micro-XRF line scans on the fragment 4Q11 (left) and one fragment of the Thanksgiving Scroll(right). The samples are visibly highly inhomogeneous.

enhancement is present. These layers may originate from the manufacturing process or the storage and aging of the fragments. In the following these features will be called debris layers and their presence is indicated in tables 5.4 and 5.5, also. Additionally, the mean net peak intensity of bromine is listed for a fast comparison of scans measured within one beamtime.

With the laboratory 3D Micro-XRF spectrometer scans on samples 4Q2, 4Q13, A43, A44, M4, M9 were conducted with 500 s live time and 20 - 30 µm step width. Debris layers could be distinguished on all samples except A43, which is consistent with the synchrotron measurements. With Micro-XRF numerous line scans were performed with step widths of 70 to 200 µm and 20 to 50 s live time. The samples are highly inhomogeneous laterally as well as into the depth.

Scattering

In order to draw conclusions on the composition of the parchment, marker elements must be found which are homogeneously distributed throughout the sample. These elements can be assumed to be part of the parchment matrix and have not been added during storage or transportation, but during manufacturing.

Figure 5.6 shows a depth scan on a spot without ink on one of the Genesis Apocryphon pieces (Genesis13). The bromine and the Compton depth profile are displayed as well as their ratio.

The Compton profile shows, that the density of the sample into the depth varies considerably. On the other hand it is obvious, that, although the parchment is highly

sample	beamtime	no of scans	live time / s	step width / µm	debris layers?	notes	Br net peak intensity/ $\cdot 10^8$
Genesis13	03.07	2	250	10	no	parchment	5
	03.07	2	250	4 - 15	no	ink	5 - 8
	04.08	1	50	7	yes	parchment	5
	04.08	1	50	5 - 10	yes	ink	4 - 10
Genesis14	11.07	2	100	5 - 10	slightly	parchment, Kupferfraß	5 - 8
	11.07	5	100	5 - 10	slightly	ink, Kupferfraß	5 - 8
	04.08	3	50	5 - 7	?	very much damage!, parchment and ink	5 - 20
Thanksgiving	11.07	2	100	5 - 10	slightly	parchment, very thin	3
	11.07	5	100	5 - 10	slightly	ink, no distinction	3
	04.08	1	50	7	?	ink spot	5
Tempelscroll	11.07	4	100	5 - 10	slightly	parchment, damaged	5
	11.07	5	100	5 - 10	slightly	ink, damaged	5 - 10
	04.08	2	50 - 200	5 - 10	no	8 and 19 keV	2

Table 5.5: 3D Micro-XRF measurements at the Berlin synchrotron BESSY II, 35 scans during three beamtimes on different spots of 4 samples were performed.

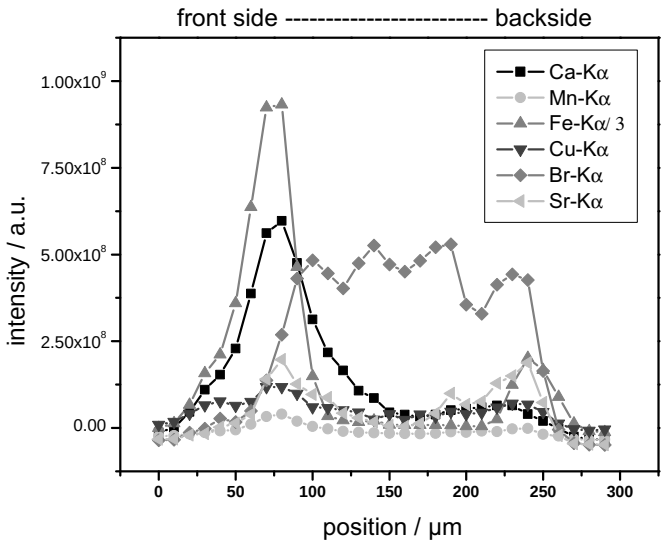

Figure 5.5: Depth scan of the fragment 4Q13 with 19 keV excitation energy, 100 s live time, 10 µm step width. Debris layers are clearly visible on both surfaces.

inhomogeneous, Br is homogeneously distributed. The Br depth profile follows the Compton profile, the ratio is constant throughout the parchment. This makes Br a suitable element for the classification of the parchment.

Positioning

Figure 5.7 shows a measurement of the fragment 4Q11. The scan was conducted with an excitation energy of 19 keV, with a step width of 10 µm and 100 s live time per spectrum. In the left graph the fluorescence profiles are depicted. The sample is very inhomogeneous. In the right graph the bromine depth profile and the scattering profiles can be compared. All profiles are very similar. The agreement between Compton and Rayleigh scattering shows, that the matrix composition of the parchment does not change significantly into the depth, while the agreement with the Br profile supports the statement of the latter section, that Br is a matrix constituent.

In order to find more marker elements, the sample was measured with two excitation energies as well as from the front, the back and the side, see figure 5.8. All spectra from the measurement on the side of the fragment were collected in the same depth in relation to the surface. Fast depth scans were employed to guarantee this aspect. That means, that prior to the collection of a spectrum, a depth scan with a short live time was performed and the probing volume was positioned at a fixed position in relation to the sample surface. The distance between this position and the sample surface was chosen to be only a few micrometers. In this way absorption phenomena could be minimized in order to measure elements with low fluorescence energies throughout the whole depth of

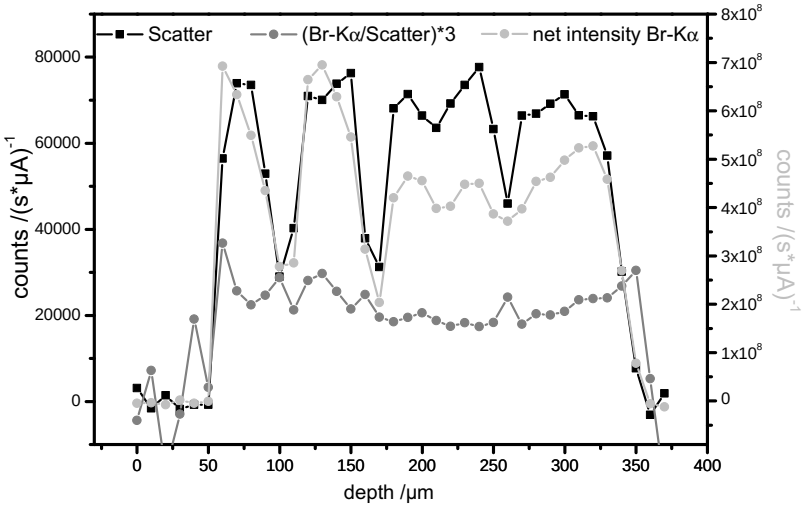

Figure 5.6: Scatter and bromine depth profiles as well as their ratio of a scan on a fragment of Genesis Apocryphon. Bromine is homogeneously distributed in the parchment.

the sample.

The two excitation energies were chosen in order to effectively excite the broadest possible range of elements, 8 keV for light elements and 19 keV for transition metals. Figure 5.9, top panel, shows six Fe Kα-fluorescence depth profiles derived from six different measurements. The agreement of the profiles shows the excellent reproducibility of the positioning of the sample, even after the excitation energy has been changed. The bottom graph of figure 5.9 shows, that chlorine is an additional matrix constituent.

5.2.2 Quantitative analysis

Quantification of 3D Micro-XRF depth profiles is a laborious task. Every depth profile must first be evaluated qualitatively in order to obtain initial values for the number of layers, the sample boundaries, the concentrations of the fluorescence elements in each layer etc.. The fitting must then be judged after each iteration, as explained in section 4.3. Additionally, it is not possible to transport thousands of fragments to a synchrotron source. Thus, for routine analysis it is desirable to use a portable routine analysis method. Through the analysis of selected 3D Micro-XRF investigations, adequate marker elements can be found. Micro-XRF can then be used for the quantification of these elements as will be explained in the next section. Other specific archaeological questions can only be answered with depth resolved measurements. In such cases 3D Micro-XRF proves to be a suitable tool, as will be discussed at the end of this section.

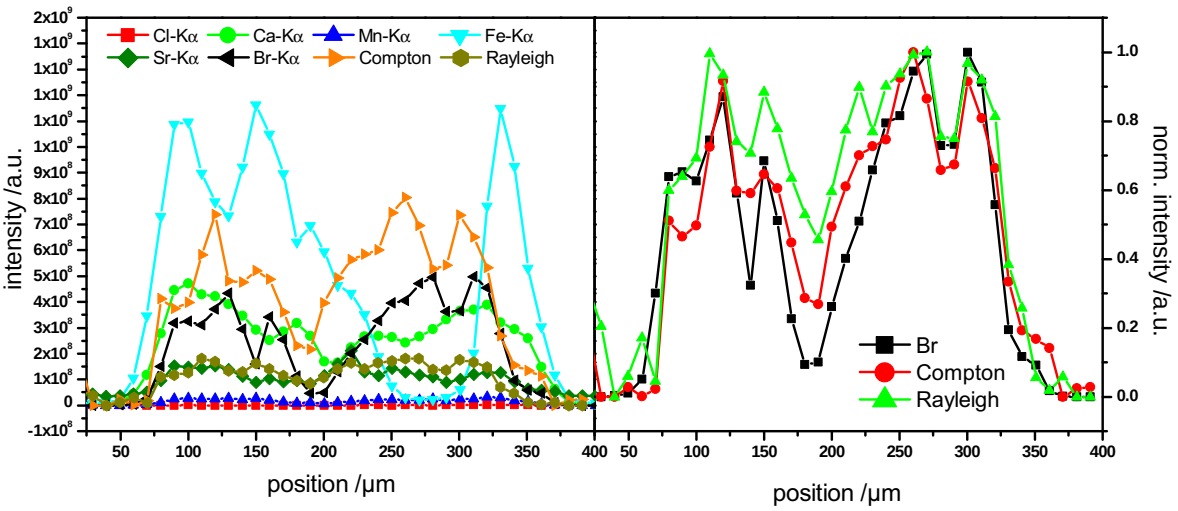

Figure 5.7: Left: Depth profiles of a scan on 4Q11 with 19 keV excitation energy. Right: Scattering depth profiles and Br depth profile. Br is homogeneously distributed in the parchment.

Routine classification

As already mentioned, it is not feasible to investigate all fragments with 3D Micro-XRF, especially as quantitative analysis is until now only possible for measurements at the synchrotron. Not only are many fragments not allowed to be transported, but the investigation of more than 800 samples cannot be done with this specialized method. Already the qualitative analysis of the 3D Micro-XRF scans confirms the assumption, that Cl and Br are matrix constituents. Matrix elements can be analyzed quantitatively with Micro-XRF, if the absorption is not too high. The information depth for Cl-Kα radiation in parchment with normal detection is about 50 µm, while for Br-Kα radiation it is about 5 mm. That means, that absorption of fluorescence radiation is a serious problem for the Cl quantification, while the bromine fluorescence is not affected considerably by a few hundreds of micrometers of parchment. Thus, if Br values from Micro-XRF and 3D Micro-XRF quantification agree, classification of fragments can be done routinely with portable Micro-XRF spectrometers - even on site.

Validation

For the validation of the agreement of the two methods the quantitative example of one scan of the Thanksgiving Scroll fragment will be shown in the following. The fragment

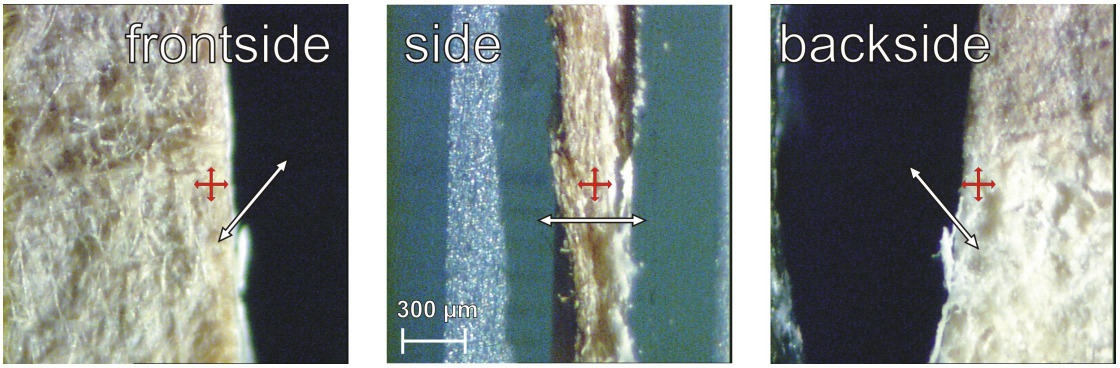

Figure 5.8: Sample 4Q11 was measured on the same spot with two excitation energies from the front, the back and the side.

was weighed, measured in order to obtain the area, a line scan with the Micro-XRF spectrometer was conducted and a 3D Micro-XRF depth scan was performed at the mySpot beamline. The spot for the 3D Micro-XRF scan was chosen in order to have the best agreement with the Micro-XRF line scan.

For the evaluation of the Micro-XRF line scans the dark matrix was assumed to be collagen. Analysis of the spectra yields area density and concentration values for all visible elements. The quantification was done assuming a homogeneous sample of intermediate thickness. This holds only for elements, which are homogeneously distributed into the depth of the parchment, i.e. the analysis values of Fe or Ca are inaccurate. For matrix constituents like phosphor with low fluorescence energy, the quantitative value is incorrect because the absorption of the debris layers is not taken into account, while for elements like bromine, where the absorption is negligible, the result must be accurate.

Nevertheless, for elements which constitute the dark matrix for the 3D measurements, the Micro-XRF values were used. The quantification of the scattered radiation yield then the density of the investigated sample (fitting option no 2 of table 4.5). With this additional information the local densities of the elements can be derived (fitting option no 27 and 8). Thickness values are obtained for possible layers and the whole sample.

Thus, for the validation of the agreement of the methods following values can be used: the area density and the Br concentration for Micro-XRF and in case of 3D Micro-XRF the thickness, the local density of bromine and the density of the sample.

example: Thanksgiving Scroll	area density / g/cm^2	thickness / µm	density / g/cm^3	Br concentration / ppm	Br local density / g/cm^3
3D Micro-XRF		150	1.12	(100)	0.000112
Micro-XRF	0.022			120	

Table 5.6: Validation values for the bromine concentration in a piece of the Thanksgiving Scroll obtained with Micro-XRF and 3D Micro-XRF

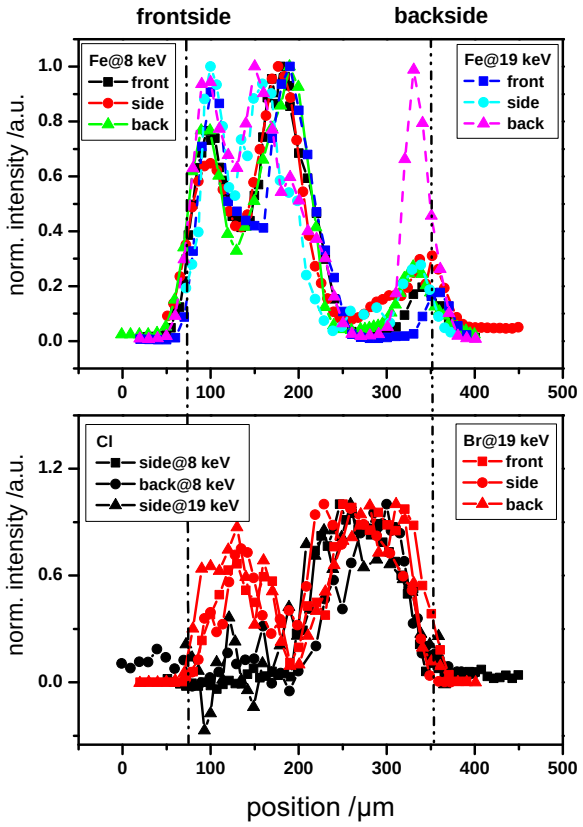

Figure 5.9: Top: Fe depth profiles of six depth scans: 8 and 19 keV excitation energy, measurement from the front side, the back side and along the side of the fragment. Bottom: Cl and Br depth profiles agree, thus, Cl is also homogeneously distributed in the parchment.

In table 5.6 values obtained through the quantification of both methods are presented. The local density of bromine of the 3D Micro-XRF depth scan divided by the density of the sample leads to a concentration of 100 ppm, which is in good agreement with the Micro-XRF value (120 ppm). The weighing measurement yields a density of 1.59 g/cm^3, which is consistent with the value of 1.47 g/cm^3 calculated with the area density derived by Micro-XRF and the thickness derived by 3D Micro-XRF. The deviation to the density value obtained by fitting the 3D Micro-XRF scattering profiles (1.12 g/cm^3) can be explained with slightly incorrect calibration values for the scattered radiation due to micro-inhomogeneities in the glass reference samples used.

Considering the inhomogeneity of the investigated samples, the good agreement of the Br concentration values obtained through the two methods makes it possible to use Micro-XRF as a routine method for the analysis of the Br content in the parchment. On the other hand, the information depth for chlorine is very small. In some investigated

cases already the thickness of the debris layers on the surfaces is bigger than this information depth. XRF methods are therefore not the right tool for the classification of the Qumran fragments on the basis of the Cl to Br ratio.

Figure 5.10 shows Br concentrations for all samples investigated with 3D Micro-XRF. Displayed are Micro-XRF quantification results (blue), 3D Micro-XRF reconstruction values (green) and values obtained by the qualitative analysis of the 3D Micro-XRF depth profiles (red). This qualitative examination was conducted by dividing the mean net peak area intensity by the integral sensitivity value corresponding to the beamtime and then normalizing all values in order to have an agreement with the quantitative values. The displayed uncertainties are statistical values.

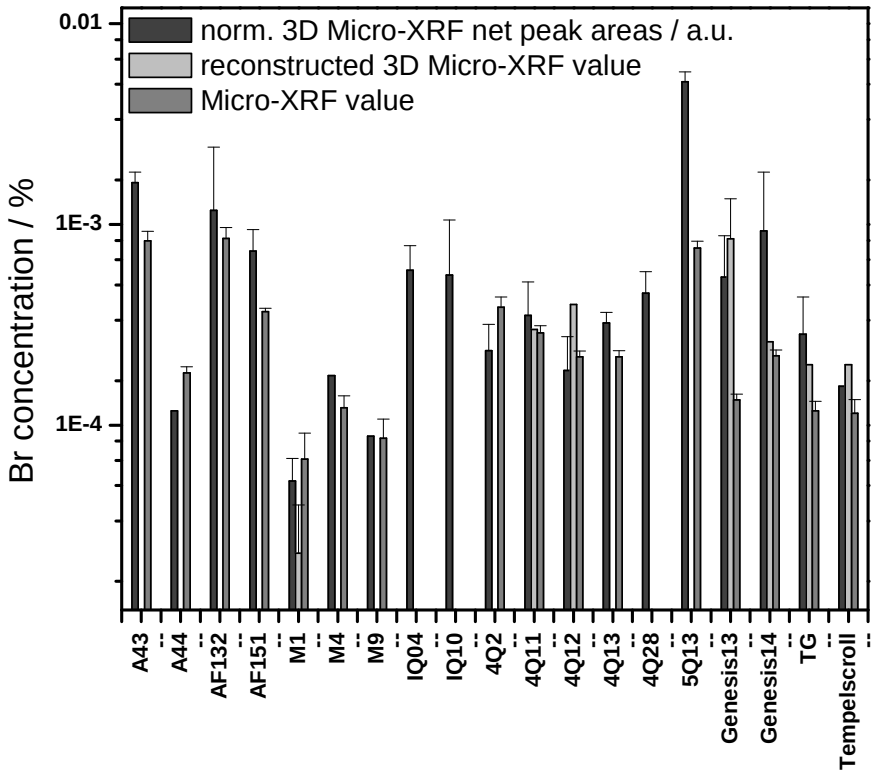

Figure 5.10: Quantification results of all 3D measurements

The basic trends in the concentration values are reflected by all three methods. For example the M-series fragments, which originate from Murabba'at - far away from Qumran or the Dead Sea - have a considerably smaller Br content than the 4Q series. The

differences of the Br concentration values of figure 5.10 can be explained with the inhomogeneity of the samples. The 3D Micro-XRF depth scans were performed on spots of the Micro-XRF line scans. As mentioned earlier, the composition of the parchment varies considerably in one Micro-XRF line scan, see figure 5.4, therefore differences in the quantification values must be expected. Nevertheless, figure 5.10 can be understood as a starting point for a database for Br content in the Dead Sea Scrolls.

Specific archaeometric questions

Fragments of the important scrolls were investigated in order to find references about provenance and manufacturing site. The three investigated scrolls differ in texture and preservation state. While the Tempel Scroll is a very thin, bright parchment, the Thanksgiving Scroll has darkened so much, that scripture can hardly be distinguished to the naked eye. The peculiarity of the Genesis Apocryphon Scroll is, that the carbon-based ink must contain copper, as Kupferfrass has begun to degrade the parchment.

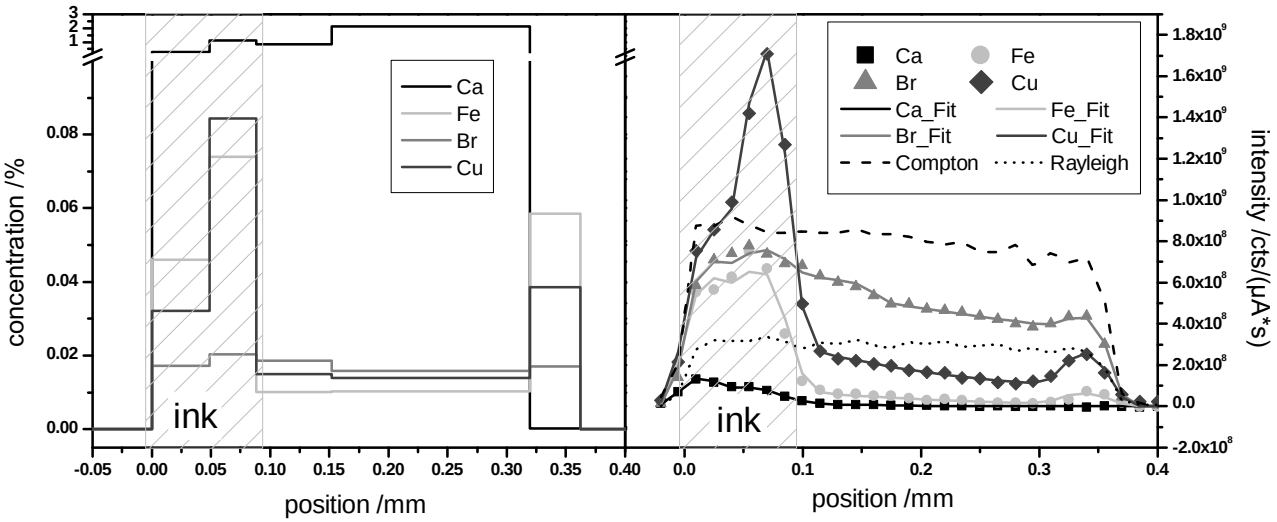

Figure 5.11: Left: Reconstruction of the scan on Genesis Apocryphon on ink shown in the right graph.

The possibility to distinguish between parchment and ink, in order to gain more information about writing and working habits, was one of the main goals of the investigation. Figure 5.11 shows an example of a scan on Genesis Apocryphon where ink and parchment can clearly be separated. In the right graph the depth profiles and the quantitative fit are displayed. The left graph displays the reconstructed concentration values. Br is

relatively homogeneously distributed into the depth of the sample, while the Fe, Cu and Sr fluorescence intensities are higher at the surfaces. On the front side, the Cu content is enhanced noticeably, where the Cu containing ink was applied. The ink has penetrated into the parchment, forming an ink/parchment layer of about 100 µm.

In the case of the other two scrolls, the differentiation between ink and parchment cannot be done. All trace elements are present in the ink as well as in the parchment and density differences cannot be distinguished. As a result the parchment and the ink must have been made with water with a comparable fingerprint concerning trace elements. The conclusion can therefore be drawn implicitly, that they were manufactured under similar conditions and maybe even in the same area.

The classification of fragments concerning their absolute Br concentration and the additional information about similarities between the composition of the ink and the parchment can be interpreted as a starting point for further investigations. In the context of the international cooperation, 3D Micro-XRF has proved to offer new analytical possibilities because it renders non-destructive depth resolution feasible.

Summary

In this presented case study, fragments of the Dead Sea Scrolls were investigated in order to gain insight about manufacturing technique and provenance. Dealing with these priceless cultural heritage objects, the non-destructiveness of the method was mandatory. The fragments are very complex analytical samples, as they are heterogeneous laterally as well as into the depth, and because no adequate reference samples exist. Through the analysis of fluorescence and scattered radiation of 3D Micro-XRF measurements, the elemental composition as well as density variations throughout the whole depth of the samples are accessible. Debris layers can clearly be distinguished from the parchment, in some cases a differentiation of ink to parchment can be performed. 3D Micro-XRF allows a quantitative view into the inside of the fragments and can, thus, help to understand the nature of these fragments. And this understanding is a first step for classification and the development of conservation strategies.

5.3 Black enamel

As an example for the usefulness of qualitative analysis with a laboratory 3D Micro-XRF spectrometer, measurements on another reverse painting on glass will be discussed in this section. In the presented historical glass object 'Lüneburger Meditationstafel' of the 14^{th} century, see figure 5.12, black enamel was used as a contour color. Black enamel ('Schwarzlot') consists of pulverized lead glass that is colored with iron oxide and/or copper oxide in an organic binder (e.g. gum Arabic). The art historical question in this particular case concerned the production technique, more specific the differentiation between cold painting and stained glass techniques.

Figure 5.12: Investigated glass object 'Lüneburger Meditationstafel' of the 14^{th} century (National Museum, Schwerin)

The technique used for reverse painted glass is similar to stained glass. Glass is the substrate material in both cases; in reverse paintings the glass is decorated with pigments in organic binding media (so-called cold-painting), while stained glass is decorated with enamels that are fired onto the glass. While black enamel is typically used for the contouring in stained glass, its use in reverse-paintings on glass would be technologically a combination of stained glass materials with cold-painting application. This would make reverse painting on glass a mixture of both techniques that develops into a genre of its own.

Micro-XRF and laboratory as well as synchrotron 3D Micro-XRF measurements were utilized for this particular archaeological question. All laboratory 3D measurements were conducted by Kathrin Lange in the course of her diploma thesis [Lan08], where the experimental details are given. Micro-XRF measurements were performed by Timo Wolff [Wol09].

5.3.1 Reference measurements

In order to be able to differentiate between cold painting and stained glass, two reference glass objects were manufactured by Hans-Jörg Ranz of revertro [http://www.revertro.eu/]. On two glass slides commercially available black enamel (Heraeus type 04889) was applied. While on sample VP1 the enamel was left to dry, sample VP2 was fired for 30 minutes at 700° C, see figure 5.13.

Figure 5.13: Reference glass objects. VP2 was fired after application of the paint.

The visible differences were investigated with the compact 3D Micro-XRF spectrometer described in section 2.4.2. Depth scans were conducted on the backside of the object, on the front side and on spots with black enamel. While quantitative analysis is not yet feasible, see section 3.4, qualitative information could be derived.

Figure 5.14 shows four depth scans on spots on the front and backside of the two reference samples. The depth scans on the front and backside of VP1 (not fired sample) and the backside scan on VP2 (fired sample) are similar, while the depth scan on the front side of VP2 shows significant changes due to the burning process.

Lead glass has a low melting temperature ($\approx 900°$ C, transition temperature $\approx 470°$ C) compared to other glasses. During the burning process the lead glass in the black enamel melts and glass and black enamel fuse together. In this example, additionally copper and zinc have diffused due to the melting of the lead glass from the black enamel laterally into the surrounding glass. The information depth for Pb-Lα fluorescence radiation with a detection angle of 45° in a SiO_2 matrix and a density of 2.2 g/cm^3 is $\approx$ 200 µm, for Zn Kα and Cu Kα only $\approx$ 100 µm. Due to the relatively low depth resolution of the setup, it is not possible to determine whether the element from the black enamel have diffused into the depth also, though the concept of directed diffusion might be unlikely. The diffusion has not penetrated to the backside of the object.

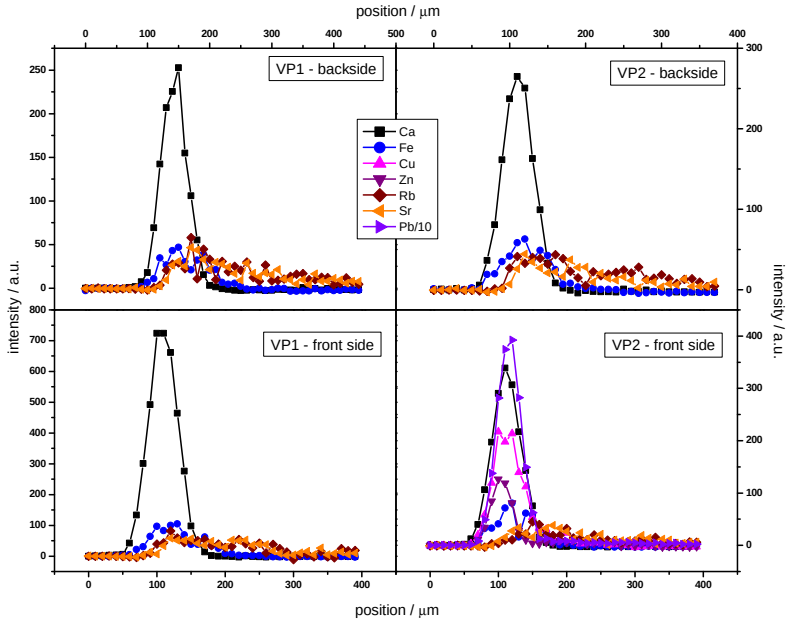

Figure 5.14: Depth scans on the reference samples of figure 5.13 performed with the compact 3D Micro-XRF spectrometer. The depth scans on the front and backside of VP1 (not fired) and the backside scan on VP2 (fired) are similar, while the depth scan on the front side of VP2 shows significant changes due to the burning process.

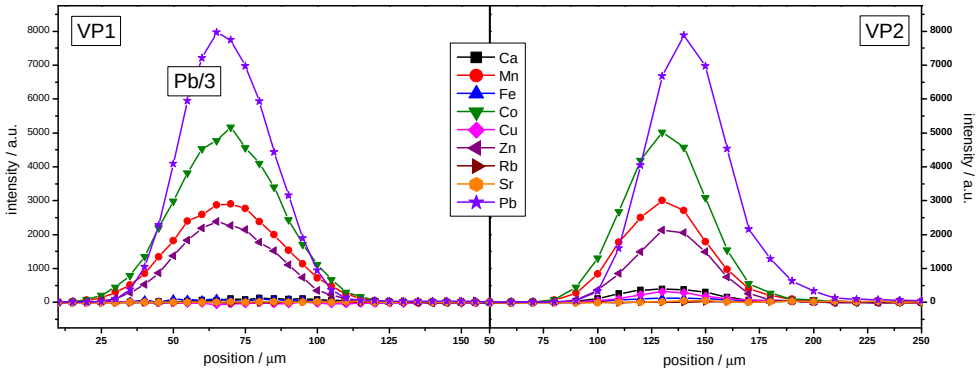

Figure 5.15: left: Depth scan on VP1, note the downscaling of lead. right: depth scan on VP2. Main elements of the black enamel are Pb, Co, Mn, Zn. Firing of the object changes the ratio of Pb to the other elements.

Fluorescence elements in the glass are Ca, Fe, Rb and Sr, while the black enamel additionally contains Cu, Zn and Pb. Measurements on spots with black enamel show, that Mn and Co are enamel constituents, see figure 5.15.[2]

The measurements of the front side of VP2 have shown, that Pb, Cu and Zn have migrated from the black enamel into the surrounding glass, see figure 5.14. The other two black enamel components Co and Mn must not be considered as mobile elements. The change of ratio between Pb and Co in the scan of figure 5.15 confirms this assumption. While the ratio of Pb:Co before the burning process is 5:1 (VP1) it changes to 3:2 for VP2.

The differentiation of layers in this case is rather difficult due to the high absorption of the black enamel layer. Especially in the case of VP1, where the lead content is three-times higher than in the case of VP2 the fluorescence intensity of the glass elements is very low. In principle the differentiation should be possible as demonstrated in figure 5.16. Based on the values of figure 3.13 on page 53 the succession of fluorescence intensity occurrence is plotted as a function of the difference of FWHM for the respective fluorescence energies. That means, that the difference of the FWHM of the probing volume between the Ca Kα fluorescence line and Mn Kα fluorescence line ($\approx$ 2.6 µm) is plotted as the distance between the rise of their intensity. The thickness of the lines corresponds to the respective uncertainties of the FWHM measurements. The left graph demonstrates a system of 10 µm black enamel on glass and the right graph a homogeneous system, where black enamel has completely melted into the glass.

In section 3.2.1 the simulation example showed, that the ratio of difference in FWHM is reflected in the succession of fluorescence intensity occurrence. That means, that the ratio of the distance between the occurrence of the fluorescence intensity of f.e. Ca to Fe to Sr is analog to the difference of the width of the probing volume for Ca to Fe to Sr. For a molten black enamel layer the succession of fluorescence intensity must be according to the fluorescence energy of the elements. In case of a black enamel layer, the succession is changed. The succession of occurrence or the difference between the occurrence of the elements are, thus, evidence for a layered system.

In this case conclusions have to be drawn very carefully, because all glass elements have a very low fluorescence intensity and high statistic errors are responsible, that Rb and Sr fluorescence cannot be used in case of VP1. This leaves only Ca as a marker for the glass, which has a comparably low fluorescence energy and is thus also considerably effected by absorption.

Figure 5.17 shows the normalized depth scans of figure 5.15. The succession of fluorescence occurrence of the scan on VP2 (right panel) is similar to the model of a molten black enamel layer (right graph of figure 5.16). The depth scan on VP1 (left panel) shows a changed succession. The intensity of the Ca Kα line rises after all other fluorescence intensities, although the probing volume is biggest for the energy of this line. Additionally, the distances between the rises of intensity of the other elements do not

[2] Cu, Fe and Pb are expected to be present in historical black enamel. In this case, though, Mn, Co and Zn show remarkably high fluorescence intensities. As the fluorescence energies of these elements are similar, i.e. the sensitivity of the setup for these elements is comparable, they must be major components of the commercially purchased black enamel.

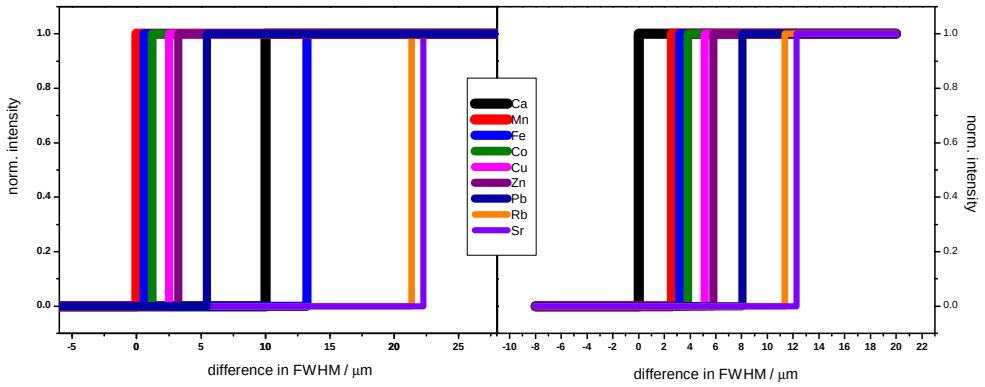

Figure 5.16: Succession of elements for a system of 10 µm black enamel on glass (left) and a one-layered system, where black enamel has completely melted into the glass. The thickness of the lines corresponds to the uncertainties of the FWHM measurements.

show the expected relation as if one layer would be assumed. Thus, for the not fired reference sample (VP1) a layered system can be assumed.

Measurements show, that the black enamel (Heraeus type 04889) which was purchased as a historical glass color contains the main elements Pb, Co, Mn and Zn and smaller amounts of Fe and Cu and is, thus, not authentic. When burning the glass object, the lead glass powder melts into the glass matrix. Cu and Zn seem to be very mobile elements, which migrate laterally into the surrounding glass when heated, while Mn and Co could not be detected on spots without visible black enamel. A differentiation of cold painting (VP1) and stained glass (VP2) could be conducted. Following facts are evidence for the firing of the glass object in this case:

1. Pb and other enamel components (Cu and Zn) can be detected on spots without visible black enamel.

2. The ratio of Pb fluorescence to fluorescence of other enamel components (Mn, Co) changes due to different mobility.

3. The succession of occurrence of fluorescence intensity of elements is comparable to a one-layered system.

Important to note is, based on section 5.1, that diffusion processes can also be responsible for similar changes in historical glass objects. In case of an object, where glass and black enamel compositions are not known in advance, the first two factors cannot be

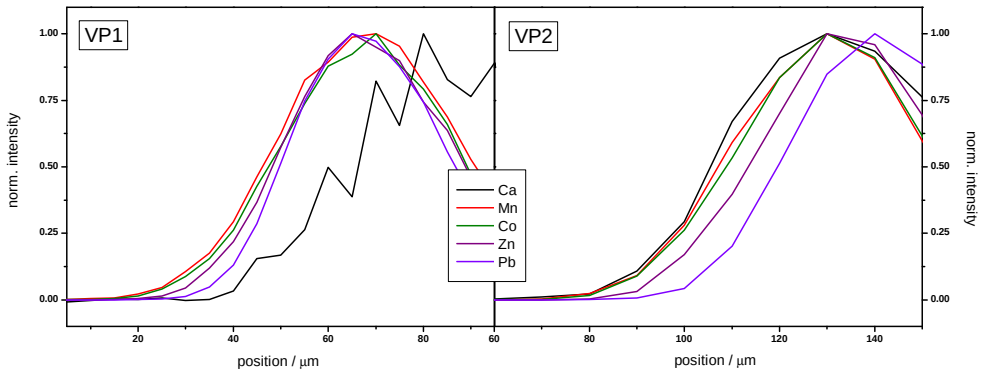

Figure 5.17: Normalized depth scans of figure 5.15. The succession of fluorescence occurrence of the scan on VP2 (right panel) is similar to the model of a molten black enamel layer (right graph of figure 5.16). The depth scan on VP1 (left panel) shows a changed succession, thus, a layered system is probable.

applied for a differentiation. The third factor, though, is a criterion for the distinction between cold painting and stained glass.

5.3.2 Measurements of the 'Lüneburger Meditationstafel'

This principle distinction criterion should help to evaluate historical objects, in this study the 'Lüneburger Mediationstafel'. In the following, measurements with the compact laboratory system and with the synchrotron setup are presented.

Laboratory measurements

Measurements on a fragment of the 'Lüneburger Meditationstafel' were conducted with step widths of 10 µm, live times of 50 to 100s and 50 kV / 600 µA as X-ray tube settings. It was impossible to measure spots on the not painted side of the object, but depth scans were performed, see figure 5.18, on black enamel spots (right panels) and glass spots (left graphs). The bottom graphs are normalized to 1 in order to depict the succession of elements.

The normalized glass scan (bottom left) shows a one-layered succession of elements. By comparison with the bottom right graph, where the normalized profile of a black enamel spot is depicted, the black enamel constituents can be derived. The enamel contains Pb, Fe, Cu and Zn. Each of these elements is detected also in the scans on glass spots. This is not evidence for migration processes, as the glass matrix might contain these elements. The ratio of fluorescence for the black enamel components cannot be compared in this case. The only factor that can differentiate between cold painting and stained glass is

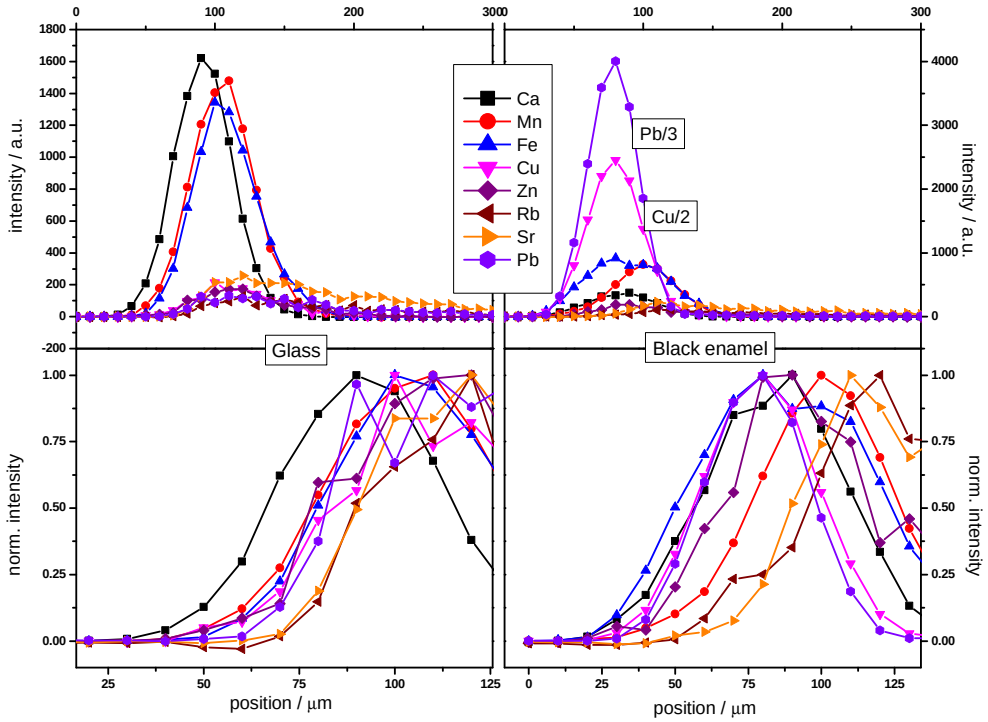

Figure 5.18: Depth scans of a glass spot (left) and a black enamel spot (right) obtained with the compact 3D Micro-XRF spectrometer. The bottom graphs are normalized to 1 in order to depict the succession of elements.

the succession of the occurrence of the intensity of the fluorescence elements in the depth profiles. The succession of occurrence of elements in the bottom right panel of figure 5.18 is not according to the fluorescence energies of the elements. While the succession of Ca, Mn, Rb and Sr is comparable to the glass scan, the position of the black enamel constituents is shifted to the front. This fact is an indication for a layered system, thus, a confirmation for the assumption that the object has not been fired after application of paint.

Synchrotron measurements

In order to validate this assumption, the piece was additionally measured at the mySpot beamline of BESSY II. Depth scans on glass spots and black enamel spots were conducted with 50 s live time and step widths of 5 µm. The quantification of one scan on a black enamel spot will be discussed in the following.

In order to obtain the dark matrix of the glass and the black enamel, Micro-XRF

Oxide	black enamel	glass matrix
	concentration / %	
SiO_2	-	37.5
P_2O_5	-	4.4
K_2O	5.6	10.8
CaO	3.0	15.8
MnO	0.2	0.6
Fe_2O_3	0.6	0.3
CuO	1.6	0.03
ZnO	0.06	0.02
Rb_2O	-	0.02
SrO	-	0.05
BaO	0.02	0.1
PbO	9.8	0.04

Table 5.7: Concentration values of Oxides of the black enamel and the glass matrix of the 'Lüneburger Meditationstafel' derived by Micro-XRF [Wol09]

measurements with the Micro-XRF spectrometer described in [Wol09] were conducted on the object. The glass was assumed to be a soda-lime glass (Micro-XRF dark matrix: NaO). From the qualitative analysis of the 3D Micro-XRF measurements, the black enamel layer was assumed to be around 10 µm thick. With this information and the assumption, that the black enamel was dispersed in a gum Arabic matrix, the Micro-XRF spectra on the black enamel were quantified with a two-layered model. Quantification values are presented in table refJesusTimo. Pb, Cu, Fe and Zn have been identified as black enamel constituents, which is in agreement with the 3D laboratory measurements.[3]

Figure 5.19 shows one of eight depth scans. The measured data (scatter) and the reconstructed fit (lines) are displayed and show good agreement. Two layers are clearly visible and better separated than in the measurements with the laboratory system due to the higher depth resolution of the setup at the mySpot beamline. The best fit was achieved with three layers, a black enamel of about 3 µm, a corrosion zone of about 13 µm and a glass bulk layer. As 3 µm is beneath the depth resolution of the setup, this thickness cannot be taken as an absolute value, but as an indication for a very thin layer.

The reconstructed concentration values for the fluorescence elements are displayed in tables 5.8 and 5.9 for the black enamel and the glass, respectively. Due to the fact, that the Micro-XRF quantification uses a two-layer model, differences are expected in the concentration values. The black enamel values are not affected by the corrosion layer

[3]Traces of Ag have been identified additionally with Micro-XRF, see table 5.7, due to a partial silver decoration. Ag cannot be measured with 3D Micro-XRF, because its fluorescence energy for K as well as L lines lies outside the sensitivity range.

element	concentration / %		rel. deviation
	Micro-XRF	3D Micro-XRF	
K	4.7	12.2	-161
Ca	2.2	6.8	-215
Mn	0.14	<det. limit	(100)
Fe	0.40	0.49	-24
Cu	1.24	1.99	-61
Zn	0.04	0.05	-14
Pb	9.1	9.4	-3

Table 5.8: Quantification values for elemental concentrations in the black enamel derived with Micro-XRF and 3D Micro-XRF and their relative deviations. The concentration value for Mn was reconstructed to be $5 \cdot 10^{-9}$ which means that it is below detection limit of the used spectrometer.

element	concentration / %			rel. deviation	
	Micro-XRF	3D Micro-XRF			
		corrosion layer	bulk	corrosion layer	bulk
K	8.9	7.3	7.2	19	20
Ca	11.3	12.1	12.5	-8	-11
Mn	0.44	0.53	0.55	-19	-24
Fe	0.23	0.12	0.47	49	-107
Cu	0.03	0.19	0.03	-590	-4
Zn	0.02	0.03	0.02	-38	-18
Rb	0.02	0.01	0.01	13	19
Sr	0.04	0.04	0.05	-1	-10
Pb	0.04	0.67	0.02	-670	57

Table 5.9: Quantification values for elemental concentrations in the corrosion layer and the glass bulk derived with Micro-XRF and 3D Micro-XRF and their relative deviations.

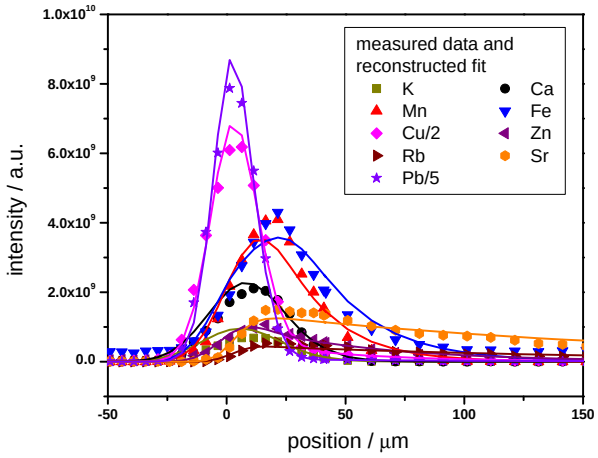

Figure 5.19: Depth scan of a black enamel spot with the mySpot beamline setup. Measured data (scatter) and reconstructed fit (lines) are displayed.

and, thus, the deviation values lie for most elements in the expected range of 20 to 50 % as discussed in section 5.1. Higher deviations for low-Z elements can be explained by the high absorption of the lead glass. Considering the heterogeneity of the investigated object due to bad state of preservation, the high absorption of the black enamel layer and the formation of the corrosion layer, the values for the glass bulk agree between both techniques.

From the 3D Micro-XRF reconstruction it is clearly visible, that lead and copper have migrated into the glass. The assumption of a 10 µm thick black enamel layer from the qualitative analysis of the 3D Micro-XRF spectra is a good guess, considering the formation of the corrosion layer. Other depth scans on spots with black enamel also show diffusion zones between black enamel and glass in accordance to the results obtained with the reverse painting on glass investigated in section 5.1. A melting process based on the results discussed before is highly unlikely.

This example illustrates the merits and the limitations when using two complimentary techniques. Micro-XRF as an integrating method cannot be applied to stratified samples without further knowledge of the sample, i.e. the number of layers. 3D Micro-XRF on the other hand needs information about the dark matrix, which can be provided by Micro-XRF. This example shows once more, that quantitative analysis is only feasible when using different experimental techniques. Nevertheless, the main result of both techniques is the same: the sample was not fired after the application of the black enamel.

Summary

In this presented case study, 3D Micro-XRF investigations were used to answer one specific art historian question. 3D Micro-XRF measurements with X-ray tube excitation and synchrotron excitation as well as Micro-XRF experiments have been performed on a historical reverse painting on glass. Although the investigated piece is as a historical glass object heterogeneous and the confocal measurements with synchrotron and with X-ray tube excitation have not been conducted on exactly the same position, the result is unambiguous. In the example of the 'Lüneburger Meditationstafel' black enamel as a stained glass color was used in a cold painting. And this mixing of two techniques might just be interpreted as a new art historian genre [HBH$^+$09].

The suitability of qualitative 3D Micro-XRF with X-ray tube excitation was shown for the differentiation of homogeneous samples as opposed to layered structures. This possibility is an inherent characteristic of the technique and can therefore be routinely used without the need for a full quantification. With new compact 3D Micro-XRF spectrometers available, this fact may lead to an increasing user community and new fields of application as synchrotron radiation is no longer mandatory.

6 Discussion, conclusion and outlook

In this work the new method of 3D Micro-XRF was presented. Due to the use of two polycapillary lenses in a confocal arrangement, fluorescence and scattered information can be derived three-dimensionally from a sample. The analysis of the experimental data yields the elemental composition into the depth of the investigated object. The goal of this work was to develop and validate the quantification for 3D Micro-XRF in order to render this technique into a true analytical tool.

An analytical expression for the fluorescence intensities of elements in a thick homogeneous sample when measured by 3D Micro-XRF was first published in [MK05]. Therein, a model for a three-dimensional sensitivity was presented and first ideas for a calibration and a quantification for monochromatic excitation were formulated. In this work, these ideas were implemented in an analysis software and validated with the help of reference samples. The model was extended to the analysis of stratified samples. Additionally, the possibility to use the scattered radiation was included in the quantification procedure.

One of the main assumptions for the quantification model is that the acceptance area of a polycapillary halflens can be described by a Gaussian intensity distribution. Characterization measurements of the used polycapillary lenses confirmed this assumption and demonstrated the need for a calibration, as the transmission or spot size functions are extremely dependent on the usage of the optic.

Numerous 3D Micro-XRF experiments were performed with two laboratory setups and at two different beamlines of the Berlin synchrotron BESSY II. Experience was gained concerning alignment procedures, experimental strategies as well as calibration requirements. With this knowledge, 3D Micro-XRF could be developed into a true analytical tool for the analysis of unknown samples without the need for similar reference samples.

The quantification of reference material was used for the evaluation of uncertainties inherent of this new technique. 3D Micro-XRF is well suited for the investigation of samples with low density values due to the low absorption and the accompanying high information depth. In the example of especially manufactured polymer reference samples (five layers - one element) the reconstruction of thickness and composition of layers could be shown to be in excellent agreement with the manufacturers values. The reconstruction of the composition of a thick homogeneous glass reference sample (one layer - thirteen elements) demonstrated first analytical difficulties concerning detection limits and absorption of low fluorescence energies. Uncertainties for the reconstructed concentrations range from 5 % for the polymere samples and about 20 % for the analysis of the glass reference sample with higher discrepancies for trace and low-Z elements. Thickness reconstruction proved to be less ambiguous with uncertainties smaller than 10 %.

The analysis of more complex samples results in a more semi-quantitative reconstruction. As a first demonstration the investigation of car paint samples was discussed. The high absorption from a pure Zn layer hinders the quantitative analysis. Nevertheless valuable information can be derived into the depth of a sample as f.e. the layer thicknesses and the attribution of elements to certain layers. Scattered radiation is used in this example for the reconstruction of a clearcoat layer with no fluorescence elements.

Application examples from the field of archaeometry were presented. 3D Micro-XRF spectroscopy as a destruction-free method has the advantage, that sampling or sectioning of the object is not necessary. This new method has proved to be applicable to many questions concerning cultural heritage objects. In the presented examples it was shown, that 3D Micro-XRF has the ability to deal as a semiquantitative method with the difficulties encountered when investigation extremely inhomogeneous samples. The use of scattered radiation as an addition to the fluorescence information can give valuable information about density variations within a sample. Additionally, through the reconstruction of the scattered depth profiles the question of dark matrix and density can be solved to some extend.

Laboratory 3D Micro-XRF measurements were performed with X-ray tube excitation. While quantitative analysis is not yet possible, first studies on the qualitative capabilities of the systems were performed. For many relevant questions qualitative or semi-quantitative analysis of 3D measurements yields sufficient information. A new compact 3D Micro-XRF spectrometer shows very stable performance giving the possibility of routine laboratory measurements. First quantification ideas for polychromatic excitation have been established and a follow-up DFG project (Entwicklung eines 3D Mikro-Röntgenfluoreszenz Laboranalysengerätes) has already been applied for. In this project, the compact spectrometer is supposed to be developed into a commercially available tool with implemented analysis software.

In general, it must be stated, that the quantification of 3D Micro-XRF measurements in most cases demands a priori knowledge of the investigated sample. The number of layers, the density of the layers and the elemental composition of the dark matrix must be given in advance. The accuracy of these initial values and the complexity of the sample influences the fitting procedure. The reconstruction procedure has to be adapted to each sample and judged by the user interactively. Different fitting strategies can be applied according to the nature of the sample.

In comparison to classical Micro-XRF, the quantification is, thus, more laborious and the results are less accurate. Nevertheless, 3D Micro-XRF as a tool for the investigation of stratified materials is an alternative, if sectioning of the sample has serious disadvantages or nondestructive characterization is the only option. For many scientific issues especially concerning cultural heritage objects, as shown in this work, relative concentration profiles or quantitative analysis with lower precision provides valuable and important information.

In the future, this new technique will be extended to new fields of application. The 3D Micro-XRF setup at the mySpot beamline at BESSY II already includes a nitrogen

cold gas stream for the cryogenic fixation of specimen [KMP+07]. This feature enables the destruction-free investigation of biological specimen. The compact 3D Micro-XRF spectrometer will be equipped in the near future with a similar construction in order to render biological investigations in the laboratory feasible.

Another extension of the method is the measurements of absorption characteristics in the confocal geometry (3D Micro-XANES), thus, giving the possibility to investigate chemical speciation three-dimensionally. First measurements with the synchrotron setup have been conducted and the development of an analytical model has already been initiated in our group.

The idea of confocal measurements has triggered another new experimental technique - 3D micro proton induced X-ray emission (3D Micro-PIXE). In collaboration with scientist of the Institute of Nuclear Physics, NCSR Demokritos, Athens, Greece, first measurements were performed at the Jožef Stefan Institute in Ljubljana, Slovenia [KSZ+07], and the centre de recherche et de restauration des musées de France (C2RMF), Paris, France [KKS+07]. Based on the quantification model presented in this work, 3D Micro-PIXE measurements have already been analyzed [SKM+09].

With the possibility to do routine experiments in the laboratory, full 3D maps become feasible. The accompanying increase in data size will need new ways of handling. The visualization of three-dimensional net peak intensities will be a part of the follow-up DFG project. Clustering of data based on principal component analysis will be developed in order to recognize structures in the depth of a sample.

7 Danksagung

Ich möchte mich bei Prof. Eberhardt bedanken, für die Möglichkeit zu promovieren und für die Zeit, die er sich für mich und meine Arbeit genommen hat.

Gefreut hat mich, dass aus meiner anfangs Zweitbetreuerin Birgit Kanngießer, dann glücklicherweise meine Erstbetreuerin wurde. Ihr möchte ich vor allem dafür danken, dass sie immer an mich geglaubt hat. Sie ist ein Vorbild nicht nur in akademischer Hinsicht.

Vielen Dank gebührt Wolfgang Malzer für die Einführung in (sein) analytisches Denken. Zwar denken wir immer noch aus und in entgegengesetzte Richtungen, doch weiß ich das inzwischen zu schätzen. Ich freue mich sehr, dass er nun wieder zu uns stößt.

Dem Arbeitskreis Analytische Chemie der Uni Hannover unter der Leitung von Prof. Vogt möchte ich danken für die fruchtbare Kooperation. Insbesondere Ina Schaumann war unerläßlich für die Validierungsmessungen und ihre sympatische Art hat die experimentelle Arbeit bei Bessy und die darauf folgenden endlosen Auswertungsversuche sehr bereichert.

Der Arbeitsgruppe Kunst- und Kulturgutanalyse der BAM möchte ich für die Möglichkeit danken, Anwendungsbeispiele aus der Archäometrie untersuchen zu können. Durch Gespräche mit Oliver Hahn hat sich in nicht nur einem Gebiet mein Horizont erweitert. Ohne die unzähligen Mikro-RFA Messungen, Auswertungen und die gemeinsamen Linsencharakterisierungsmessungen von und mit Timo Wolff wäre diese Arbeit nicht möglich gewesen.

Allen aktuellen und nicht mehr aktuellen Mitgliedern der Arbeitsgruppe 'Analytische Röntgenspektroskopie/Röntgenphysik' der TU Berlin möchte ich danken für eine äußerst angenehme Arbeitsathmosphäre. Ich habe viel gelernt und gleichzeitig viele spannende Menschen kennen lernen dürfen. Danke euch allen.

Zum Schluss danke ich allen nicht namentlich Erwähnten, die mir Kraft, Rückhalt und Freude gegeben haben.

Bibliography

[BDF+01] V. M. Borovikov, V. K. Djurba, M. G. Fedurin, V. V. Repkov, G. V. Karpov, G. N. Kulipanov, M. V. Kuzin, N. A. Mezentsev, V. A. Shkaruba, D. Kraemer, and D. Richter. Superconducting 7T Wave Length Shifter for BESSY-II. *Nucl. Instrum. Methods Phys. Res. Section A*, 467-468(Part 1):181 – 184, 2001.

[BEB+08] A. Bjeoumikhov, M. Erko, S. Bjeoumikhova, A. Erko, I. Snigireva, A. Snigirev, T. Wolff, I. Mantouvalou, W. Malzer, and B. Kanngießer. Capillary [mu]Focus X-ray lenses with parabolic and elliptic profile. *Nucl. Instrum. Methods Phys. Res. Section A*, 587(2-3):458 – 463, 2008.

[BKL+06] B. Beckhoff, B. Kanngießer, N. Langhoff, R. Wedell, and H. Wolff, editors. *Practical X-ray Fluorescence Analysis*. Springer, 2006.

[BRB+01] H. Bronk, S. Röhrs, A. Bjeoumikhov, N. Langhoff, J. Schmalz, R. Wedell, H.-E. Gorny, A. Herold, and U. Waldschläger. ArtTAX : a new mobile spectrometer for energy-dispersive micro X-ray fluorescence spectrometry on art and archaeological objects. *Fresenius J. Anal. Chem.*, 371:307 – 316, 2001. papier.

[CCB+04] R. Cesareo, A. Castellano, G. Buccolieri, S. Quarta, and M. Marabelli. Giotto in the Chapel of the Scrovegni: EDXRF analysis of the golden haloes with portable equipment. *X-Ray Spectrom.*, 33(4):289 – 293, 2004.

[CCV+94] G.-J. Chen, F. Cerrina, K. F. Voss, K. H. Kim, and F. C. Brown. Raytracing of X-ray focusing capillaries. *Nucl. Instrum. Methods Phys. Res. Section A*, 347(1-3):407 – 411, 1994.

[DJS+08] J. Dik, K. Janssens, G. Van Der Snickt, L. van der Loeff, K. Rickers, and M. Cotte. Visualization of a Lost Painting by Vincent van Gogh Using Synchrotron Radiation Based X-ray Fluorescence Elemental Mapping. *Anal. Chem.*, 80(16):6436–6442, 2008.

[Dum33] J. W. M. Dumond. The Linear Momenta of Electrons in Atoms and in Solid Bodies as Revealed by X-Ray Scattering. *Rev. Mod. Phys.*, 5(1):1–33, Jan 1933.

[Ebe99] H. Ebel. X-ray tube spectra. *X-Ray Spectrom.*, 28:255–266, 1999.

[Egg04] T. Eggert. *Die spektrale Antwort von Silizium-Röntgendetektoren*. PhD thesis, Technische Universität München, 2004.

[ERS02] W. T. Elam, B. D. Ravel, and J. R. Sieber. A new atomic database for X-ray spectroscopic calculations. *Rad. Phys. and Chem.*, 63(2):121 – 128, 2002.

[ESF+04] A. Erko, F. Schäfers, A. Firsov, W.B. Peatman, W. Eberhardt, and R. Signorato. The BESSY X-ray microfocus beamline project. *Spectrochim. Acta, Part B*, 59(10-11):1543 – 1548, 2004. 17th International Congress on X-Ray Optics and Microanalysis.

[FMBC00] A. Facchini, C. Malara, G. Bazzani, and P. L. Cavallotti. Ancient Parchment Examination by Surface Investigation Methods. *J. Colloid Interface Sci.*, 231(2):213 – 220, 2000.

[FRJ+02] J. L. Ferrero, C. Roldán, D. Juanes, E. Rollano, and C. Morera. Analysis of pigments from Spanish works of art using a portable EDXRF spectrometer. *X-Ray Spectrom.*, 31(6):441 – 447, 2002.

[GC98] G. E. Gigante and R. Cesareo. Non-destructive analysis of ancient metal alloys by in situ EDXRF transportable equipment. *Rad. Phys. and Chem.*, 51(4-6):689 – 700, 1998.

[GJSX99] J. Gormley, T. Jach, E. Steel, and Q.-F. Xiao. Polycapillary x-ray optic spectral gain and transmission. *X-Ray Spectrom.*, 28(2):115 – 120, 1999.

[GLE03] M. Van Gysel, P. Lemberge, and P. Van Espen. Description of Compton peaks in energy-dispersive x-ray fluorescence spectra. *X-Ray Spectrom.*, 32(2):139 – 147, 2003.

[GM01] R. Van Grieken and A. Markowicz, editors. *Handbook of X-Ray Spectrometry Revised and Expanded (Practical Spectroscopy, V. 29)*. CRC, 2nd edition, 11 2001.

[GP03] N. Gao and I. Y. Ponomarev. Polycapillary x-ray optics: manufacturing status, characterization and the future of the technology. *X-Ray Spectrom.*, 32(3):186 – 194, 2003.

[Gui94] A. Guinier. *X-Ray Diffraction: In Crystals, Imperfect Crystals, and Amorphous Bodies*. Dover Publications, 1994.

[HBH+09] O. Hahn, S. Bretz, C. Hagnau, H.-J. Ranz, and T. Wolff. Black enamel in reverse paintings on glass. *Archeometry*, submitted, 2009.

[HDCC07] D. Hampai, S. B. Dabagov, G. Cappuccio, and G. Cibin. X-ray propagation through polycapillary optics studied through a ray tracing approach. *Spectrochim. Acta, Part B*, 62(6-7):608 – 614, 2007. A Collection of Papers Presented at the 18th International Congress on X-Ray Optics and Microanalysis (ICXOM 2005).

[HMKB04] O. Hahn, W. Malzer, B. Kanngiesser, and B. Beckhoff. Characterization of iron-gall inks in historical manuscripts and music compositions using x-ray fluorescence spectrometry. *X-Ray Spectrom.*, 33(4):234 – 239, 2004.

[HO79] J. H. Hubbell and I. Overbo. Relativistic atomic form factors and photon coherent scattering cross sections. *J. Phys. Chem. Ref. Data*, 8(1):69–106, 1979.

[HVB+75] J. H. Hubbell, W.. J. Veigele, E. A. Briggs, R. T. Brown, D. T. Cromer, and R. J. Howerton. Atomic form factors, incoherent scattering functions, and photon scattering cross sections. *J. Phys. Chem. Ref. Data*, 4(3):471–538, 1975.

[HWK+07] O. Hahn, T. Wolff, B. Kanngießer, W. Malzer, and I. Mantouvalou. Non-destructive Investigation of the Scroll Material: "4Qcomposition Concerning Divine Providence" (4Q413). *Dead Sea Discoveries*, 14(3):359 – 364, 2007.

[Jac67] J. D. Jackson. *Classical Electrodynamics*, volume 1d ed.; New York. Wiley, 1967.

[JPF04] K. Janssens, K. Proost, and G. Falkenberg. Confocal microscopic X-ray fluorescence at the HASYLAB microfocus beamline: characteristics and possibilities. *Spectrochim. Acta, Part B*, 59(10-11):1637 – 1645, 2004. 17th International Congress on X-Ray Optics and Microanalysis.

[KKS+07] B. Kanngießer, A.-G. Karydas, R. Schütz, D. Sokaras, I. Reiche, S. Röhrs, L. Pichon, and J. Salomon. 3D Micro-PIXE at atmospheric pressure: A new tool for the investigation of art and archaeological objects. *Nucl. Instrum. Methods Phys. Res. Section B*, 264(2):383 – 388, 2007.

[KMM+08] B. Kanngießer, I. Mantouvalou, W. Malzer, T. Wolff, and O. Hahn. Non-destructive, depth resolved investigation of corrosion layers of historical glass objects by 3D Micro X-ray fluorescence analysis. *J. Anal. At. Spectrom.*, 23:814 – 819, 2008.

[KMP+07] B. Kanngießer, W. Malzer, M. Pagels, L. Lühl, and G. Weseloh. Three-dimensional micro-XRF under cryogenic conditions: a pilot experiment for spatially resolved trace analysis in biological specimens. *Anal. Bioanal.Chem.*, 389(4):1171 – 1176, 2007.

[KMR03] B. Kanngießer, W. Malzer, and I. Reiche. A new 3D micro X-ray fluorescence analysis set-up - First archaeometric applications. *Nucl. Instrum. Methods Phys. Res. Section B*, 211(2):259 – 264, 2003.

[KSZ+07] A.-G. Karydas, D. Sokaras, C.s Zarkadas, N. Grlj, P. Pelicon, M. Zitnik, R.n Schütz, W. Malzer, and B. Kanngießer. 3D Micro PIXE—a new technique

for depth-resolved elemental analysis. *J. Anal. At. Spectrom.*, 22(10):1260 – 1265, 2007.

[KvBM00] R. Klockenkämper, A. von Bohlen, and L. Moens. Analysis of pigments and inks on oil paintings and historical manuscripts using total reflection x-ray fluorescence spectrometry. *X-Ray Spectrom.*, 29(1):119 – 129, 2000.

[KVJ00] L. Kempenaers, L. Vincze, and K. Janssens. The use of synchrotron micro-XRF for characterization of the micro-heterogeneity of heavy metals in low-Z reference materials. *Spectrochim. Acta, Part B*, 55(6):651 – 669, 2000.

[Lan08] K. Lange. Korrosionsuntersuchungen an Kunstobjekten mit einem 3D Mikro-Röntgenfluoreszenz Laborspektrometer. Diploma thesis, Technische Universität Berlin, 2008.

[LWC+07] X. Lin, Z. Wang, X. Chu, T. Sun, and X. Ding. Investigation of a tabletop confocal micro X-ray fluorescence setup. *Chin. Phys. Lett.*, 24(12):3368 – 3370, 2007.

[LWS+08] X. Lin, Z. Wang, T. Sun, Q. Pan, and X. Ding. Characterization and applications of a new tabletop confocal micro X-ray fluorescence setup. *Nucl. Instrum. Methods Phys. Res. Section B*, 266(11):2638 – 2642, 2008.

[Mal04] W. Malzer. *3D Mikro-Röntgenfluoreszenzanalyse*. PhD thesis, Universität Bremen, 2004.

[Man05] I. Mantouvalou. Phase and amplitude manipulation using an acousto-optical modulator for optimised fs-laser induced breakdown spectroscopy. Diploma thesis, Technische Universität Berlin, 2005.

[MK03] W. Malzer and B. Kanngießer. Calculation of attenuation and x-ray fluorescence intensities for non-parallel x-ray beams. *X-Ray Spectrom.*, 32(2):106 – 112, 2003.

[MK05] W. Malzer and B. Kanngießer. A model for the confocal volume of 3D micro X-ray fluorescence spectrometer. *Spectrochim. Acta, Part B*, 60(9-10):1334 – 1341, 2005.

[MMS+08] I. Mantouvalou, W. Malzer, I. Schaumann, L. Lühl, R. Dargel, C. Vogt, and B. Kanngießer. Reconstruction of Thickness and Composition of Stratified Materials by Means of 3D Micro X-ray Fluorescence Spectroscopy. *Anal. Chem.*, 80(3):819–826, 2008.

[PH06] B. M. Patterson and G. J. Havrilla. Three-dimensional elemental imaging using a confocal x-ray fluorescence microscope. *Am. Lab.*, 38(8):15 – 20, 2006.

[PSPR09] R. Daniel Pérez, H. J. Sánchez, C. A. Pérez, and M. Rubio. Quantification of Multilayer Samples by Confocal μ XRF. *SYNCHROTRON RADIATION IN MATERIALS SCIENCE: Proceedings of the 6th International Conference on Synchrotron Radiation in Materials Science*, 1092(1):107–111, 2009.

[Sei08] C. Seim. Untersuchung von keltischen Keramikscherben mittels eines 3D Mikro-Röntgenfluoreszenz Laborspektrometers. Diploma thesis, Technische Universität Berlin, 2008.

[SF66] T. Shiraiwa and N. Fujino. Theoretical Calculation of Fluorescent X-Ray Intensities in Fluorescent X-Ray Spectrochemical Analysis. *Jpn. J. Appl. Phys*, 5:886 – 899, 1966.

[She55] J. Sherman. The theoretical derivation of fluorescent X-ray intensities from mixtures. *Spectrochim. Acta*, 7:283–306, 1955.

[SHHB06] C. M. Sparks, E. P. Hastings, G. J. Havrilla, and M. Beckstead. Characterizing process semiconductor thin films with a confocal micro X-ray fluorescence microscope. *Powder Diffr.*, 21(2):145–147, 2006.

[SJPL04] Z. Smit, K. Janssens, K. Proost, and I. Langus. Confocal μ-XRF depth analysis of paint layers. *Nucl. Instrum. Methods Phys. Res. Section B*, 219-220:35 – 40, 2004. Proceedings of the Sixteenth International Conference on Ion Beam Analysis.

[SKM+09] D. Sokaras, A.-G. Karydas, W. Malzer, R. Schutz, B. Kanngießer, N. Grlj, P. Pelicon, and M. Zitnik. Quantitative analysis in confocal micro-pixe-general concept and layered materials. *J Anal Atom Spectrom*, 24(5):611–621, 2009.

[SMM+09] I. Schaumann, W. Malzer, I. Mantouvalou, L. Lühl, B. Kanngießer, R. Dargel, U. Giese, and C. Vogt. Preparation and characterization of polymer layer systems for validation of 3D Micro X-ray fluorescence spectroscopy. *Spectrochim. Acta, Part B*, 64:334 – 340, 2009.

[TC82] R. Tertian and F. Claisse. *Principles of Quantitative X-Ray Fluorescence Analysis*. Heyden (London), 1982.

[TN07] K. Tsuji and K. Nakano. Development of confocal 3D micro-XRF spectrometer with dual Cr-Mo excitation. *X-Ray Spectrom.*, 36:145 – 149, 2007.

[TND07] K. Tsuji, K. Nakano, and X. Ding. Development of confocal micro X-ray fluorescence instrument using two X-ray beams. *Spectrochim. Acta, Part B*, 62(6):549 – 553, 2007.

[VJA+95] L. Vincze, K. Janssens, F. Adams, M. L. Rivers, and K. W. Jones. A general Monte Carlo simulation of ED-XRF spectrometers. II: Polarized monochromatic radiation, homogeneous samples. *Spectrochim. Acta, Part B*, 50:127 – 147, 1995.

[VVBA04] B. Vekemans, L. Vincze, F. E. Brenker, and F. Adams. Processing of three-dimensional microscopic X-ray fluorescence data. *J. Anal. At. Spectrom.*, 19:1302 – 1308, 2004.

[Wie02] H. Wiedemann. *Synchrotron Radiation*. Springer, 2002.

[WLS+08] X. Wei, Y. Lei, T. Sun, X. Lin, Q. Xu, D. Chen, Y. Zou, Z. Jiang, Y. Huang, X. Yu, X. Ding, and H. Xu. Elemental depth profile of faux bamboo paint in Forbidden City studied by synchrotron radiation confocal μ-XRF. *X-Ray Spectrom.*, 37(6):595 – 598, 2008.

[WMB+06] A. R. Woll, J. Mass, C. Bisulca, R. Huang, D.H. Bilderback, S. Gruner, and N. Gao. Development of confocal X-ray fluorescence (XRF) microscopy at the Cornell high energy synchrotron source. *Appl. Phys. A*, 83(2):235 – 238, may 2006.

[WMM+09] T. Wolff, I. Mantouvalou, W. Malzer, J. Nissen, D. Berger, I. Zizak, D. Sokaras, A. Karydas, N. Grlj, P. Pelicon, R. Schutz, M. Zitnik, and B. Kanngießer. Performance of a polycapillary halflens as focusing and collecting optic - a comparison. *J. Anal. Atom. Spectrom*, 24:669 – 675, 2009.

[Wol09] T. Wolff. *Referenzprobenfreie quantitative mikro Röntgenfluoreszenzanalyse*. PhD thesis, Technische Universität Berlin, 2009.